2014

Electronic Properties And Atomic Scale Microscopy Of Two Dimensional Materials: Graphene And Molybdenum Disulfide

Jyoti Katoch
University of Central Florida

ELECTRONIC PROPERTIES AND ATOMIC SCALE MICROSCOPY OF TWO-DIMENSIONAL NANOSCALE MATERIALS: GRAPHENE AND MOLYBDENUM DISULFIDE

by

JYOTI KATOCH
Masters in Physics, University of Central Florida, 2010

A dissertation submitted in partial fulfilment of the requirements
for the degree of Doctor of Philosophy
in the Department of Physics
in the College of Sciences
at the University of Central Florida
Orlando, Florida

Spring Term
2014

Major Professor: Masahiro Ishigami

ABSTRACT

Novel two dimensional nanoscale materials like graphene and metal dichalcogenides (MX_2) have attracted the attention of the scientific community, due to their rich physics and wide range of potential applications.

It has been shown that novel graphene based transparent conductors and radiofrequency transistors are competitive with the existing technologies. Graphene's properties are influenced sensitively by adsorbates and substrates. As such not surprisingly, physical properties of graphene are found to have a large variability, which cannot be controlled at the synthesis level, reducing the utility of graphene. As a part of my doctorate dissertation, I have developed atomic hydrogen as a novel technique to count the scatterers responsible for limiting the carrier mobility of graphene field effect transistors on silicon oxide (SiO_2) and identified that charged impurities to be the most dominant scatterer. This result enables systematic reduction of the detrimental variability in device performance of graphene. Such sensitivity to substrates also gives an opportunity for engineering device properties of graphene using substrate interaction and atomic scale vacancies. Stacking graphene on hexagonal boron-nitride (h-BN) gives rise to nanoscale periodic potential, which influences its electronic graphene. Using state-of-the-art atomic-resolution scanning probe microscope, I correlated the observed transport properties to the substrate induced extrinsic potentials. Finally in efforts to exploit graphene's sensitivity to discover new sensor technologies, I have explored non-covalent functionalization of graphene using peptides.

Molybdenum disulfide (MoS_2) exhibits thickness dependent bandgap. Transistors fabricated from single layer MoS_2 have shown a high on/off ratio. It is expected that ad-atom engineering can be used to induce on demand a metal-semiconductor transition in MoS_2. In this direction, I have

explored controlled/reversible fluorination and hydrogenation of monolayer MoS_2 to potentially derive a full range of integrated circuit technology. The in-depth characterization of the samples is carried out by Raman/photoluminescence spectroscopy and scanning tunneling microscopy.

This thesis is dedicated to my Parents

For their Unconditional Love, Motivation, and Support.

ACKNOWLEDGMENTS

Firstly, I would like to thank my PhD advisor, Masa Ishigami. As his first graduate student, I got an opportunity to work very closely with him in the lab. He taught me everything from tightening the flanges of UHV chamber to fixing the complicated STM. He guided me to become an independent thinker by providing me with an environment where I could come up with ideas, collaborate with other researchers and execute them. His knowledge, insight and experience helped me to move forward and accomplish my projects. He made sure that I got all the resources in lab to accomplish my goals. Whenever the instruments in the lab broke down or experiments did not work, his encouraging words kept my spirits high. His energy and enthusiasm made it even more enjoyable to work in lab.

I am always impressed by his presentation skills. He taught me to communicate my research efficiently and effectively through talk practice and paper writing. His advice and full support encouraged me to form Physics Women society (PWS) in the department. He is an advisor who makes an effort for the well-being of his students. I could talk freely to him about any concerns or problems that I faced. He was an involved and concerned advisor who made my graduate school a success and at the same time enjoyable.

I would like to thank Dr. Enrique del Barco for providing me an open access to the instruments in his lab. I am really impressed by his teaching skills after sitting in his ”condensed matter physics” class and enjoyed listening to his discussions during journal club meetings. I would also like to thank his group members for helping me over the years.

I would like to thank Dr. Eduardo Mucciolo for his support and guidance. He always found time from his busy schedule to discuss and advise me about my research. His passion for teaching and eagerness in helping graduate students became evident to me when he agreed to form a formal coursework relevant to my research. I was amazed by his in-depth knowledge in physics and how

he could explain difficult concepts in simple words. The fruitful discussions with him further enhanced the understanding of my research.

I would also like to thank Dr. Kevin Coffey for agreeing to be a part of my dissertation committee and being supportive. I would like to thank Dr. Bhattacharya and Dr. Rahman for their valuable guidance and help over the years. I would like to especially thank Dr. Nina Orlovskaya and her students, for providing me access and helping me to use Raman system for the experiments. Also thanks to Dr. Tetard for collaborating and allowing me to use her confocal Raman spectrometer for characterizing MoS_2 samples.

I would like to especially thank Guy Zummo for helping in my research efforts. He helped me to hook up the helium recovery system with the STM and UHV transport chamber. It was great to have an expert technician available for advice whenever needed and taking care of instruments in the clean room.

I would like to thank my supportive labmates. Ryuichi, Christian and Mike have been amazing co-workers to work with. The best part is that Ryuichi relentlessly tried to scare me off by sneaking upon me but never succeeded! Christian, who is our lab's "fume-hood police officer" was always nice to me (thank you Kelsey!) and let me use the fume hood even if my part of the workspace was a little mess (not sure if anyone else escaped his eagle eyes). Mike was the toughest to deal with until Ryuichi spilled the beans about 'Gets' (don't know what it means though). Jokes apart, Ryuichi has always been there to help me in lab and discuss scientific/non-scientific topics. He and Christian has been great help in maintaining SEM, which allowed me make devices for transport measurement without any worries. Mike taught me CVD graphene growth which helped my STM experiments.I would like to thank undergraduates Qing, Danny, John, Joel, Derek, and Ben. They are bright young members of the group who are always eager to help and try new things. I would also like to thank Dr. Ben Dawson, who was a postdoc in our lab and other past members of our group.

I would like to thank the staff in Physics department specially: Monika, Jesscia, Elizabeth, Pat,

Mike and Felix. Because of them I had to never worry about any administrative work. They were nice enough to accommodate my forgetfulness and last minute urgencies. I would like to especially thank Monika for sharing her famous and delicious cheesecake.

I would like to thank my husband Simran for being very supportive and helping. He is my strength, mentor, and best critic. Above all he is my best friend who kept me going through the stress and difficult times in graduate school. He is the man behind my success. I would also like to thank my husband's family (especially my mother-in law and sister in-law, who are simply amazing !!!). My brother in-law Gurinder's unique sense of humor was my medicine during stressful days of graduate school. They all have been very supportive, encouraging and understanding.

I would like to thank my parents for giving me the freedom to chase my dreams, providing me with resources, encouragement and love. My sisters were my earliest mentors who always looked out for me and helped tremendously in shaping my career. I have a fantastic brother in-law who supported, guided and helped in many ways. I would also like to thank all the kids in the family Manya, Karmanya and Amitoj. I always drew my strength from their love, innocence, selflessness and belief in my abilities.

I would like to thank all my friends who made Orlando a happy place to live:

Pankaj Kadwani (& his beautiful family); Dev & Karthika (for taking care of things for me when I first landed in US & Dev making sure that I ate awesome home cooked food!), Gowri & Anusha (for always being around whenever I needed any help), Shruba (really thankful for all her help and guidance. What a nice roommate to have!), Apurva, Bala Bhai, Prabhu, Meghal, Gautam and Suchi. Special thanks to Karthika's parents for their love and blessings (and obviously auntie's delicious food!!!!)

TABLE OF CONTENTS

LIST OF FIGURES

LIST OF TABLES

LIST OF ACRONYMS

AFM	Atomic force microscopy
CVD	Chemical vapor deposition
FETs	Field- effect transistors
FTIR	Fourier transform infrared
GBP	Graphene/graphite binding peptide
hBN	Hexagonal boron nitride
HOPG	Highly-oriented pyrolytic graphite
H_2O_2	Hydrogen peroxide
MD	Molecular dynamics
MoS_2	Molybdenum disulfide
SEM	Scanning electron microscopy
STM	Scanning tunneling microscopy
STS	Scanning tunneling spectroscopy
SiO_2	Silicon dioxide
UHV	Ultra high vacuum
XPS	X-ray photoelectron spectroscopy

CHAPTER 1: PROPERTIES OF GRAPHENE AND MOLYBDENUM DISULFIDE

1.1. Synthesis of graphene and molybdenum disulfide (MoS_2)

For the work presented in this thesis, I used mesoscopic sheets of graphene and monolayer molybdenum disulfide prepared by mechanically exfoliation of bulk material or macroscopic sheets grown using a chemical vapor deposition (CVD) processes as discussed in detail below.

1.1.1 Mechanical Exfoliation:

In 3-dimensional layered materials like graphite and metal dichalcogenides, the layers are held together by weak Van der waal forces of interaction. This, in principle, makes it possible to separate monolayers of these materials by breaking the weakly held bonds, using mechanical or chemical energy. Novoselov et al. [1] used this technique to isolate graphene from highly-oriented pyrolytic graphite (HOPG). Ever since then, this method has been widely used to isolate mostly defect free, high quality graphene. Typically the size of the exfoliated flakes can vary from $1\mu m - 50\mu m$ (* I once exfoliated a graphene flake of size $200\mu m$ by $50\mu m$).

In mechanical exfoliation, graphite is repeatedly cleaved using a residue-free silicone-free adhesive tape to obtain thinner graphite flakes and then the tape is put down on the target substrate. Then, the surface of the tape is rubbed gently before the tape is removed to obtain several exfoliated flakes of thin graphite and monolayers on the substrate. Similarly, bulk molybdenum disulfide (2H-MoS_2) is a layered structure which can be exfoliated by tape to isolate 1H- MoS_2 monolayers.

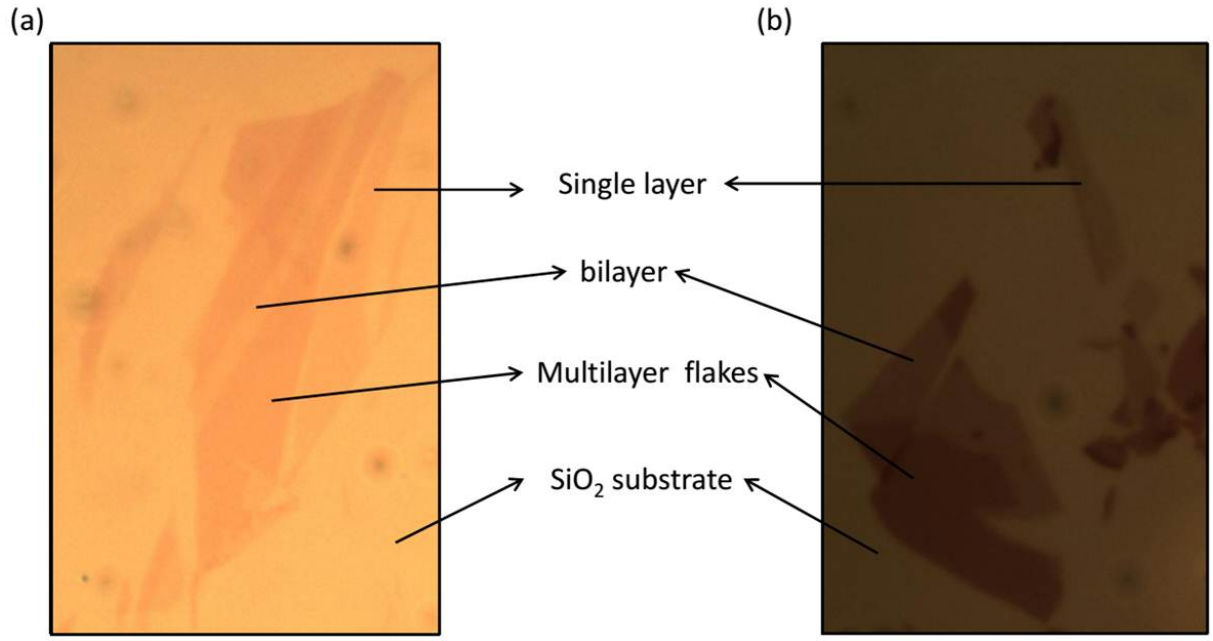

Figure 1.1: Optical images of exfoliated graphite and molybdenum disulfide on 300nm $\mathrm{SiO_2}$ substrate. Arrows label single layer, two- layer, and multilayer flakes of both graphite and $\mathrm{MoS_2}$. (a) Exfoliated flakes of graphite (b) Exfoliated flakes of $\mathrm{MoS_2}$.

Figure 1.1 (a) and (b) show optical images of exfoliated layers of graphite and molybdenum disulfide, respectively.

1.1.2 Chemical Vapor Deposition (CVD) growth:

1.1.2.1 Graphene:

Large-area synthesis of graphene and other 2D materials is particularly desired for various practical applications. Li, X., et al., [2] demonstrated that large area graphene can be grown directly on copper foil by chemical vapor deposition. This growth involves initially annealing $25\mu m$ thick copper foil in a furnace at $1000\,^{\circ}\mathrm{C}$ in a low pressure hydrogen atmosphere for 30 mins and then the graphene growth is initiated by flowing a mixture of methane and hydrogen gas. The foil is

heated in this gas mixture for about fifteen minutes to obtain continuous monolayer graphene (90% coverage) and then it is cooled down. The cooling rate plays an important role for the quality of the grown graphene. Next, this graphene is transferred to a desired substrate by wet etching the copper foil.

1.1.2.2 Molybdenum disulfide:

Monolayer $\mathrm{MoS_2}$ of size up to 120 μm can be obtained by CVD on a desired substrate. After the substrate is cleaned in piranha solution ($\mathrm{H_2SO_4} : \mathrm{H_2O_2} = 3 : 1$) for about two hours, it is loaded faced down above the crucible containing $\mathrm{MoO_3}$. Another crucible containing sulfur is kept upstream from the $\mathrm{MoO_3}$ crucible. The furnace is heated to $650\,^{\circ}\mathrm{C}$ in a $\mathrm{N_2}$ environment for fifteen minutes to obtain monolayer $\mathrm{MoS_2}$ growth on the substrate [3]. CVD $\mathrm{MoS_2}$ samples on $\mathrm{SiO_2}$ used for this thesis were synthesized by James Hone's group at Columbia University.

1.2 Band structure

1.2.1 Graphene:

The graphene lattice is composed of carbon atoms arranged in honeycomb array, with two sublattices A and B as shown in Figure 1.2(a). Each carbon atom has six electrons with electronic configuration $1\mathrm{s}^2, 2\mathrm{s}^2, 2\mathrm{p}^2$. The three valence electrons in $2\mathrm{s}, 2\mathrm{p_x}, 2\mathrm{p_y}$ orbitals hybridize to form three coplanar sp^2 orbital which gives three σ bonds. The remaining valence electron in each perpendicular $2\mathrm{p_z}$ orbital hybridize with neighboring $2\mathrm{p_z}$ orbital to form π bonds.

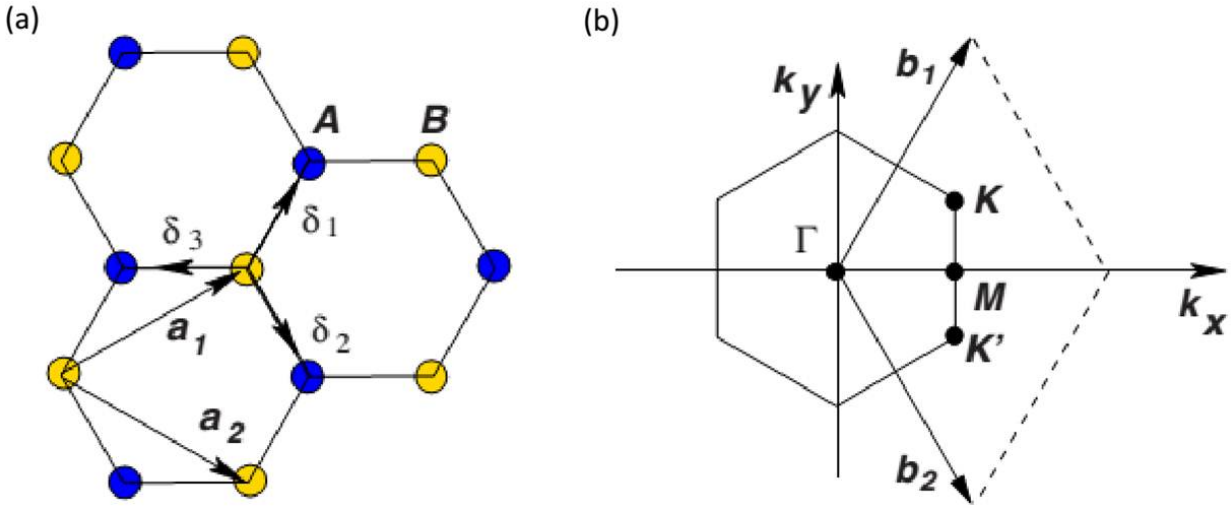

Figure 1.2: Hexagonal lattice structure of graphene. [4] (a) Lattice of graphene, which can be considered as two intertwining triangular lattices, with lattice unit vectors a_1 and a_2. (b) Graphene Brillouin zone. The valence and conduction touch each other at K and K′ points, known as Dirac points.

The mechanical properties of graphene are determined by the strength of the σ bonds whereas the electrons in the π bonds are responsible for its electronic properties.

The single-band tight binding model considering electron hopping between nearest neighbors [5], gives the energy band as

$$E_{\pm}(k) = \pm t\sqrt{1 + 4f(k)}, \tag{1.1}$$

where f(k)= $\cos^2(\mathrm{k_x a}/2) + \cos(\sqrt{3}\mathrm{k_x a}/2)\cos(\mathrm{k_y a}/2)$, and a = 2.46 Å is the lattice constant.

Figure 1.2(b) depicts the Brillouin zone of the graphene lattice. Neutral graphene ($\mathrm{E_F} = 0$) has two sets of nonequivalent sites K and K′ (known as the Dirac points) of the Brillouin zone, where the conical shaped valence and conduction bands touch as shown in Figure 1.3. Thus, graphene is a zero gap semiconductor, or semimetal. Near the Dirac points it has a linear dispersion relation given as E = $\hbar \mathrm{v_F k}$, where $\mathrm{v_F} = \sqrt{3}\mathrm{at}/2\hbar \approx 10^6 \mathrm{ms}^{-1}$ is the Fermi velocity.

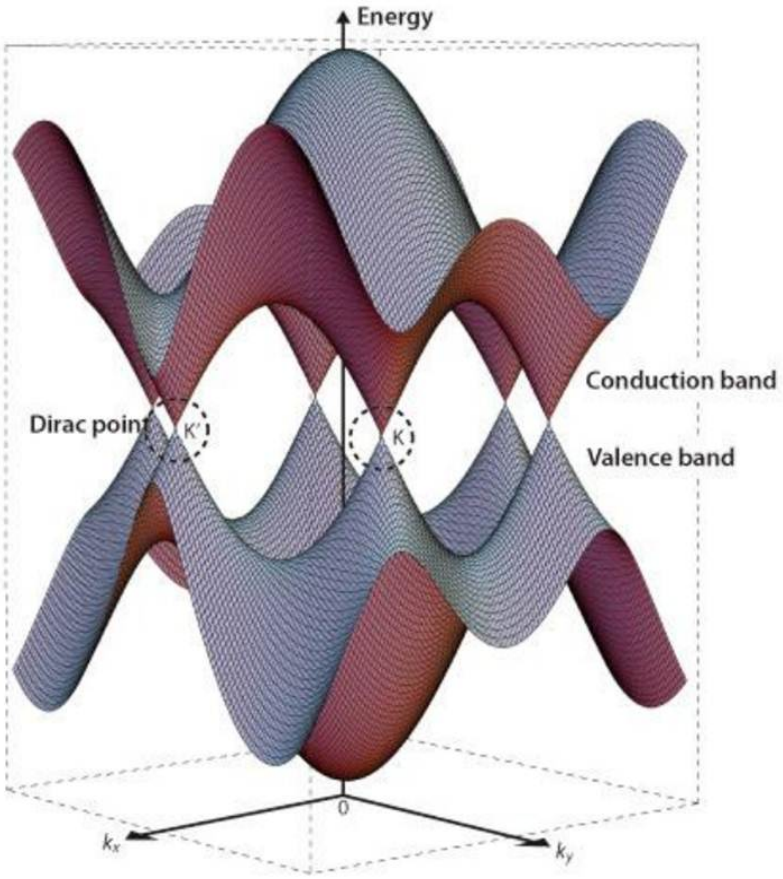

Figure 1.3: Band structure of graphene [6], where energy bands of graphene near fermi energy meet at Dirac points K and K'.

The Hamiltonian close to the Dirac point is given as

$$\mathsf{H} = \hbar v_F \begin{pmatrix} 0 & k_x - ik_y & 0 & 0 \\ k_x + ik_y & 0 & 0 & 0 \\ 0 & 0 & 0 & -k_x + ik_y \\ 0 & 0 & -k_x - ik_y & 0 \end{pmatrix} \tag{1.2}$$

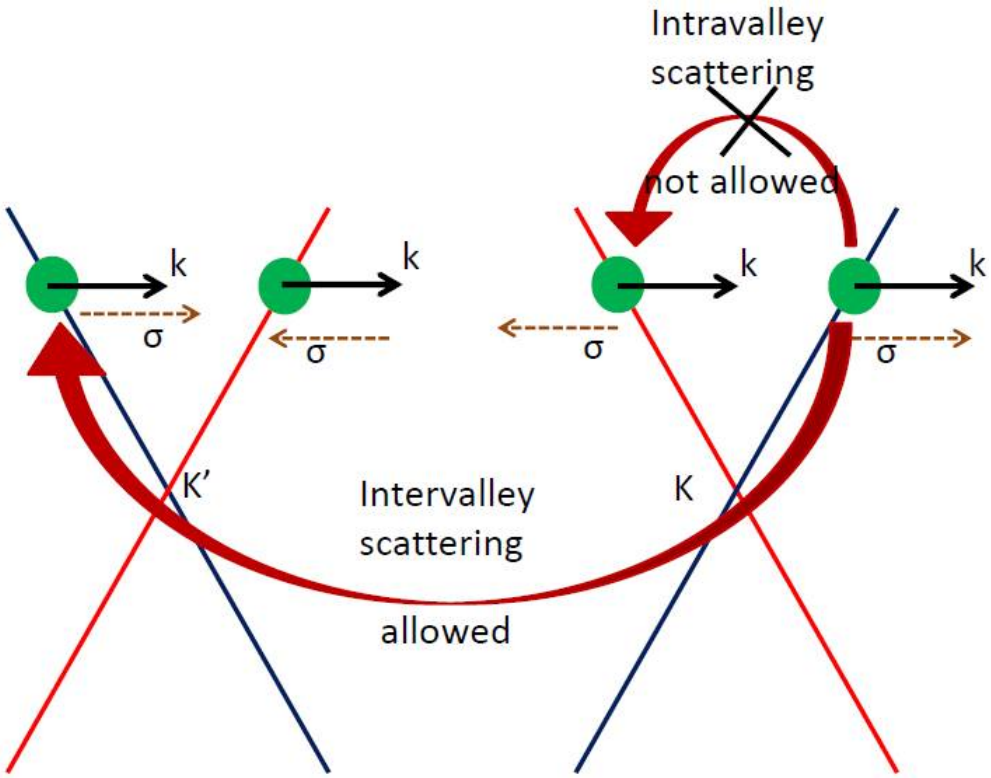

Figure 1.4: Pseudospin conservation in graphene allows intervalley transitions but forbids intravalley scattering.

The eigenstates of the above equation are

$$\begin{pmatrix} \Psi_A^K \\ \Psi_B^K \end{pmatrix} = \frac{1}{\sqrt{2}} e^{ik.r} \begin{pmatrix} e^{\frac{-i\theta_k}{2}} \\ \pm e^{\frac{i\theta_k}{2}} \end{pmatrix} \tag{1.3}$$

and

$$\begin{pmatrix} \Psi_B^{K'} \\ \Psi_A^{K'} \end{pmatrix} = \frac{1}{\sqrt{2}} e^{ik.r} \begin{pmatrix} \pm e^{\frac{-i\theta_k}{2}} \\ e^{\frac{i\theta_k}{2}} \end{pmatrix} \tag{1.4}$$

where $\pm$ signs correspond to conduction/valence bands and $\tan\theta_{\mathrm{k}} = \mathrm{k_y}/\mathrm{k_x}$.

The charge carriers in graphene behave like massless Dirac fermions and possess an extra degree of freedom called "pseudospin", which is coupled to the direction of the momentum of charge

carriers [4]. The pseduospin allows us to distinguish the contribution from each sub-lattice.

The consequence of the peculiar symmetry at the Fermi level is that the intervalley scattering (scattering of charge carriers between K and K' cones), requiring pseudospin flipping, is not allowed as depicted in Figure 1.4. This suppresses the backscattering in graphene, and theoretically predicts a long mean free path of charge carriers.

1.2.2 Molybdenum disulfide:

Bulk $\mathrm{MoS_2}$ is a 3D material, which exists in two stable forms: layered $2\mathrm{H}-\mathrm{MoS_2}$ and polytype $3\mathrm{R}-\mathrm{MoS_2}$. The layered 3D $2\mathrm{H}-\mathrm{MoS_2}$ can be exfoliated to obtain 2D $1\mathrm{H}-\mathrm{MoS_2}$. As shown in Figure 1.5, the structure of monolayer $\mathrm{MoS_2}$ is composed of hexagonally arranged Mo atoms sandwiched between two hexagonal S monatomic layers, such that Mo and $\mathrm{S_2}$ occupy alternate positions in the hexagonal corners to give a honeycomb structure. Each Mo atom has six neighboring S atoms in trigonal prismatic arrangement and each S atom forms a pyramidal center as it has three neighboring Mo atoms. The unit cell of bulk $\mathrm{MoS_2}$ consists of two $\mathrm{MoS_2}$ layers which are displaced such that each Mo atom in one layer is on top of the S atom from the two adjacent layers.

The electronic configuration of Mo and S atoms is $[\mathrm{Kr}]4\mathrm{d}^5, 5\mathrm{s}^1 \mathrm{and} [\mathrm{Ne}]3\mathrm{s}^2, 3\mathrm{p}^4$ respectively. The d states are responsible for the unique electronic properties of $\mathrm{MoS_2}$. Density functional theory (DFT) calculations show that the band structure changes with a decrease in the number of $\mathrm{MoS_2}$ layers [8], as depicted in Figure 1.6. This is due to changes in the hydriziation between p states of S and d states of Mo, as well as quantum confinement. The decrease in the number of $\mathrm{MoS_2}$ layers does not change the excitonic transitions at the Γ-point, but the indirect band transition at the Γ-point changes due to interlayer coupling.

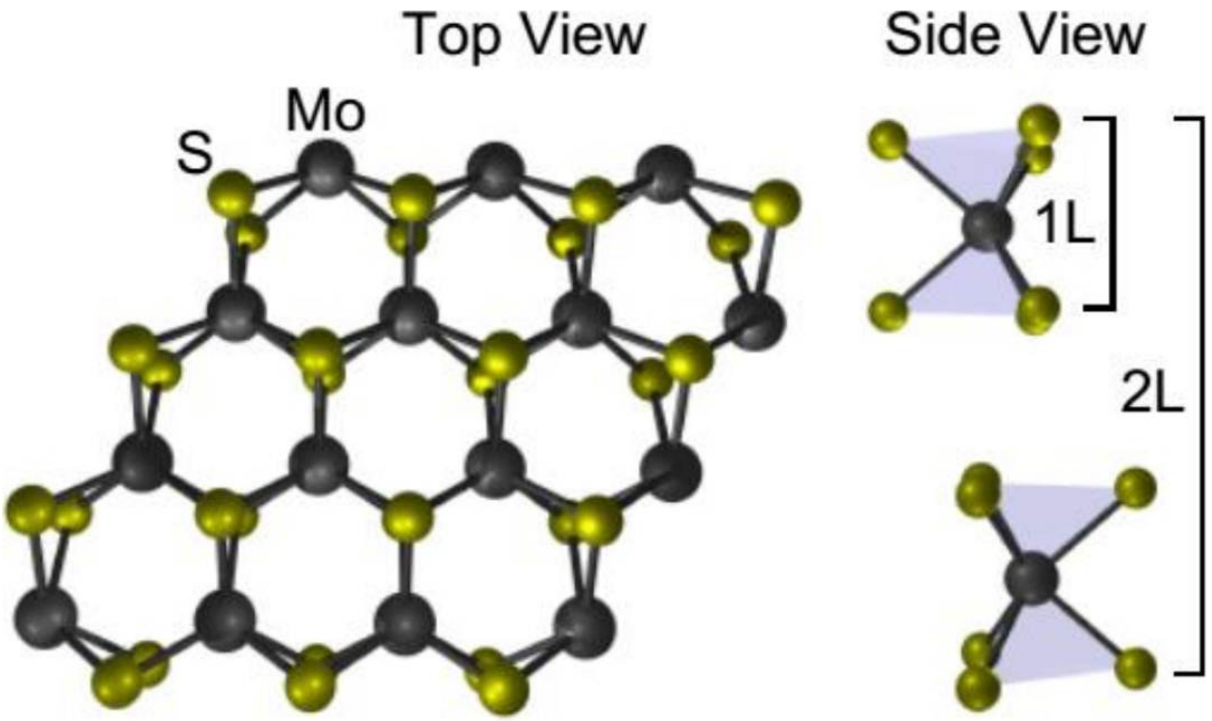

Figure 1.5: Top view and side view of monolayer MoS_2 [7], where sulfur atoms are represented by yellow and molybdenum atoms by black.

Bulk MoS_2 has a fundamental indirect band gap of 1.2 eV at the Γ-point which, for monolayer MoS_2, becomes so large that it changes to a direct band gap material with a band gap of 1.9 eV.

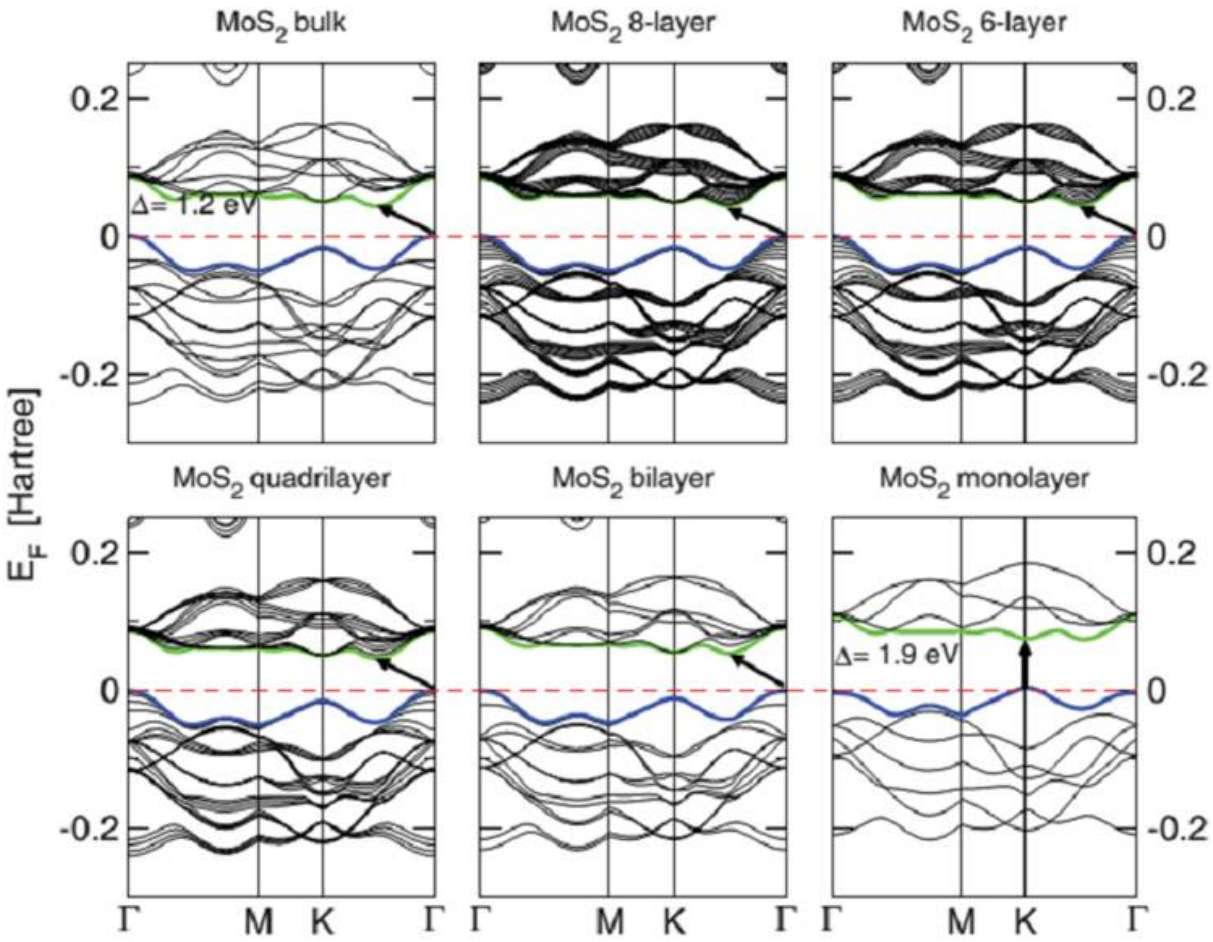

Figure 1.6: The band structure [8] for different thicknesses of MoS_2 layers, using DFT calculations. The red line denotes the Fermi level and the arrow represent the direct or indirect transition for any of these systems. It shows the transition from indirect gap in bulk MoS_2 to direct gap in single layer of MoS_2.

1.3 Electronic transport properties

1.3.1 Graphene

The charge carriers in graphene exfoliated on a SiO_2/Si substrate can be continuously tuned between holes and electrons by back gate voltage, using Si as the gate electrode.

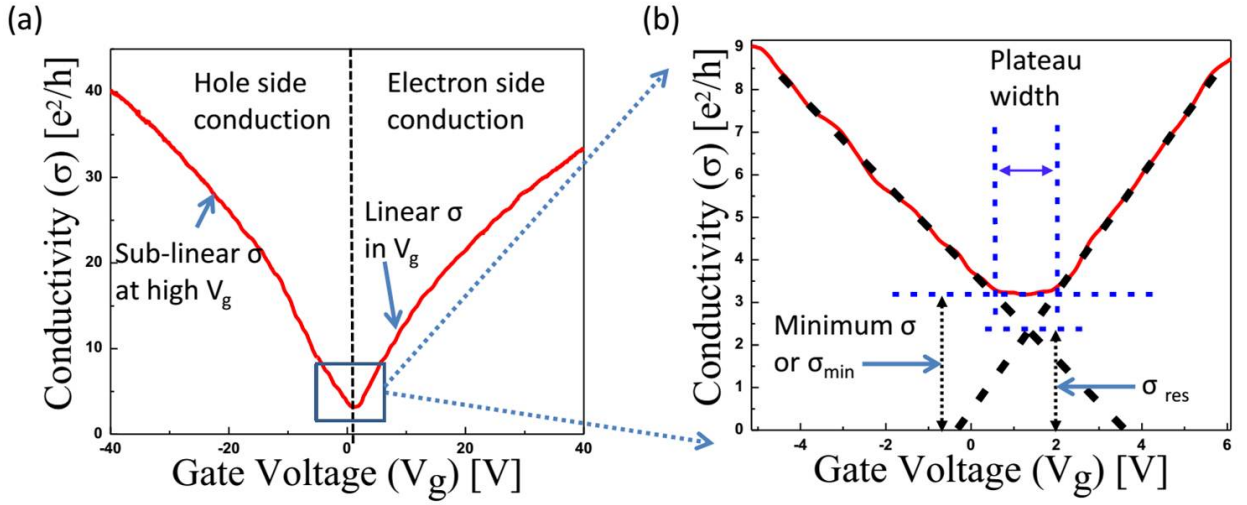

Figure 1.7: Ambipolar transport characteristic of the graphene device on SiO_2. (a) Conductivity at large carrier density shows sub-linear behavior with voltage. (b) Shows the definition for minimum conductivity, plateau width and residual conductivity.

Graphene on SiO_2 has been experimentally demonstrated to attain high field effect mobility as high as $20,000 cm^2$/Vs at room temperature and has a weak temperature dependence [9]. The conductivity of graphene, in general, can be characterized by Figure 1.7(a). At high charge carrier concentrations, the conductivity is linear with respect to the carrier density n, whereas at highest carrier concentrations the conductivity becomes sublinear with gate voltage (carrier concentration n).At low charge density (near transition between charge carriers from hole to electrons) the conductivity does not vanish but has some minimum value (known as the universal minimum conductivity, V_{min}) with a conductivity plateau. Generally, for clean high quality graphene samples (i.e. absent of any external doping) the minimum conductivity is experimentally observed near zero gate voltage is $4e^2/h$ with a smaller plateau. Figure 1.7(b) clearly depicts the minimum conductivity or σ_{min}, and plateau width near the charge neutrality point. In this figure the black dotted lines intersect above zero conductivity at residual conductivity, σ_{res}.

Owing to gate tunable high carrier mobilities, graphene has been demonstrated to have potential

application as radio frequency transistors, reaching cutoff high frequency of 155GHz with a gate length of 40 nm [10]. However due to zero bandgap and lack of a reliable technique to open its electronic bandgap without degrading its electronic transport properties, the application of graphene for integrated circuit technologies is presently hampered . This has led to search for alternate thin 2D materials with a bandgap which has larger on/off ratio.

1.3.2 Molybdenum disulfide

Single layer of $\mathrm{MoS_2}$ is a semiconductor with a bandgap of 1.9 eV. It is 0.7 nm thick and has no dangling bonds. This makes $\mathrm{MoS_2}$ an attractive material for application in next-generation electronics and opto-electronics [11]. $\mathrm{MoS_2}$ sheets on $\mathrm{SiO_2}$, have previously been demonstrated to have room temperature mobility $< 50\mathrm{cm^2V^{-1}s^{-1}}$, with sub-threshold swing $> 1\mathrm{V/decade}$ [12][13][14]. Radisavljevic et al. [15] reported n-type conduction with mobility of $200\mathrm{cm^2V^{-1}s^{-1}}$, subthreshold swing 74 mV/decade and on/off ratio of 1×10^8 at room temperature, for a top gated $\mathrm{MoS_2}$ device with a high dielectric $\mathrm{HfO_2}$. Figure 1.8 shows the typical electrical characteristics of a top gated $\mathrm{MoS_2}$ device.

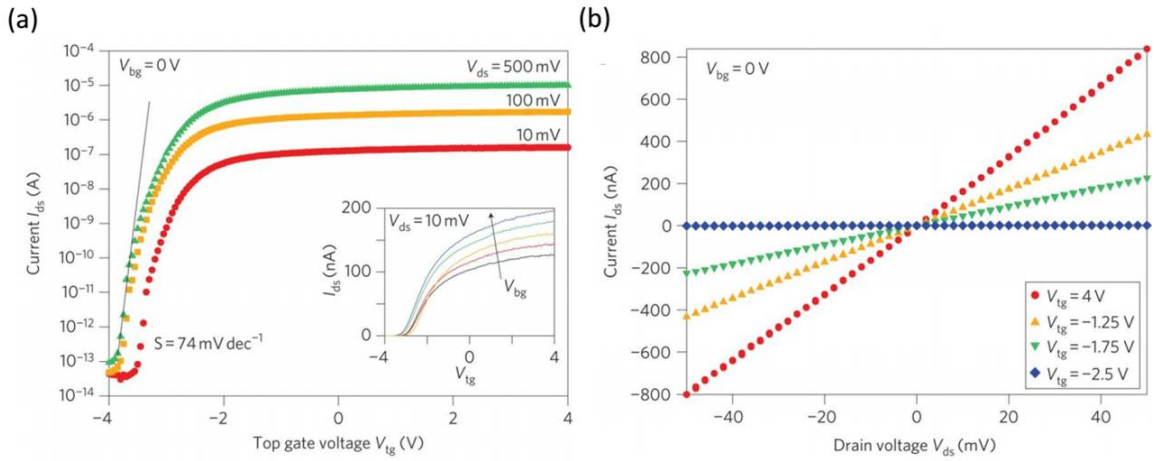

Figure 1.8: Top gated electrical characteristics [15] of MoS_2 transistor at room temperature [15]. (a) current (Ids) Vs top gate voltage (V_{tg}) curve for various voltage bias (V_{ds}). Inset shows I_{ds} Vs V_{tg} for -10V,-5V, 0V, 5V and 10V of back gate voltages(V_{bg}). (b) I_{ds} Vs V_{ds} for different V_{tg} .

1.4 Optical properties

1.4.1 Graphene:

Graphene is one atom thick but still has a high optical absorbance of 2.3%, which makes it visible to naked eye. The light absorption in graphene arises from:

1. Intraband optical absorption: In the far-infrared region, the free carrier optical response is given by the Drude model for conductivity [16] as

$$\sigma(\omega) = \frac{\sigma_0}{1 + i\omega\tau}, \tag{1.5}$$

Where σ_0 is the dc conductivity, ω is the angular frequency of light, and τ is the electron scattering time. The plasmonic excitations in graphene by light absorption are prohibited due to momentum mismatch between plasmons and photons. However such plasmonic excitations are experimentally observable by using periodic grating structures or patterned graphene arrays [17].

2. Interband optical absorption- From mid-infrared to ultraviolet region, interband (between valence and conduction band) optical transitions occurs and can be modified through electrostatic gating[16].

Raman spectroscopy is widely used as a non-destructive way to study phonon dispersion in graphene. It gives information about both its electronic properties and atomic structure [18]. Ordinarily, relaxed carriers in zero-gap graphene do not exhibit a photoluminescence (PL) signal. A PL signal has been observed for pristine graphene under excitation from a femtosecond laser [19] using an ion gel gated graphene device under near infrared laser excitation [20].

1.4.2 Molybdenum disulfide:

The optical properties of $\mathrm{MoS_2}$ vary with the number of layers due to the changes in its electronic band structure. Mak et al. [21], characterized the optical properties of monolayer and few layer $\mathrm{MoS_2}$ samples using photoluminescence, optical absorption, and photoconductivity spectroscopy at room temperature. Figure 1.9 shows the normalized PL intensity as a function of energy (eV) for various thicknesses of $\mathrm{MoS_2}$ from six layers to monolayer. This study shows that bulk $\mathrm{MoS_2}$ is an indirect band gap material whereas monolayer $\mathrm{MoS_2}$ emits light strongly as it changes to a direct band gap material. Suspended monolayer $\mathrm{MoS_2}$ shows an increase in the PL quantum yield by a factor of 10^4 as compared to bulk $\mathrm{MoS_2}$.

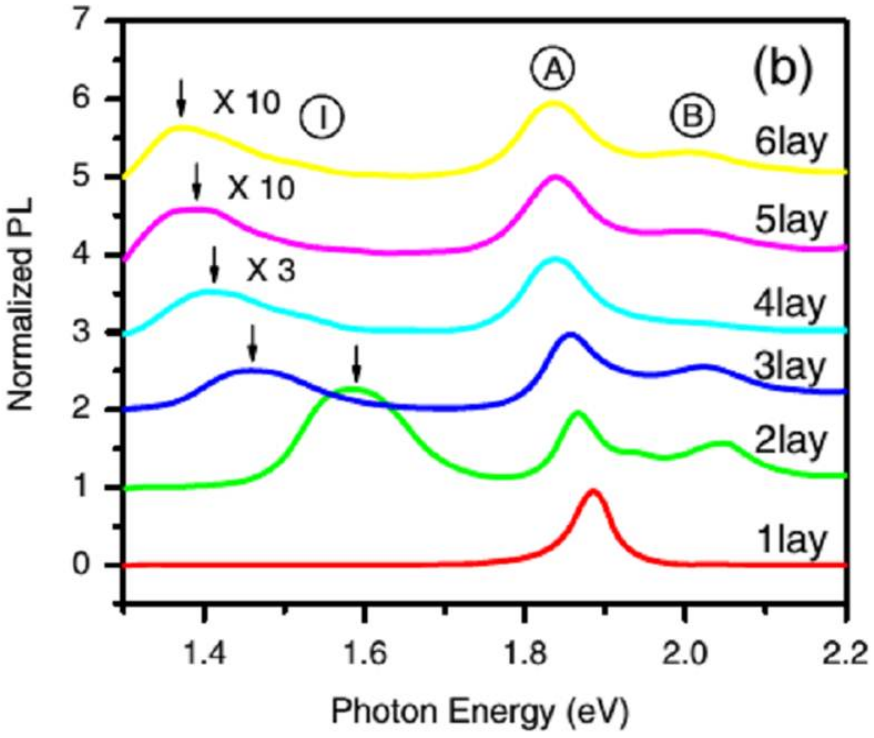

Figure 1.9: The normalized PL intensity [21] as a function of photon energy in (eV) for 1 to 6 layers of MoS_2 layers.

1.5. Impact of extrinsic impurities, adsorbates, and substrates

1.5.1. Graphene:

1.5.1.1 Phonon scattering:

Hwang et al. [22] theoretically investigated the intrinsic room-temperature mobility of graphene in the absence of other scattering mechanisms such as defects, charge impurities, etc . The resistivity due to electron scattering by longitudinal acoustic (LA) phonons is given as

$$\rho_{LA} = (\frac{h}{e^2})\frac{\pi^2 D_A^2 K_B T}{2h^2 \rho_S \nu_S^2 \nu_F^2}, \tag{1.6}$$

where D_A is acoustic deformation potential, ν_S is 2.1 $\times$ 10^4 m/s is the sound velocity for LA phonons, ν_F is the fermi velocity, K_B is the Boltzmann constant, and ρ_S = 7.6 $\times$ 10_{-7} Kg/m^2 is 2D mass density of graphene.

Experimentally the resistivity scattering due to LA phonon was demonstrated to be independent of carrier density (n) [23]. However phonon modes of the underlying substrate also play an important role in scattering elections in graphene. For example in the case of graphed on SiO_2, the polar optical phonon of the substrate scatter the electrons by exerting long range potential through remote interfacial phonon (RIP) scattering [24],[25],[26].

1.5.1.2 Charge impurities:

Charge impurities exert long-range potential which scatter the charge carriers (electrons or holes) in graphene. These random charged impurities are generally either embedded near the surface of SiO_2 substrate (intrinsically trapped ions in SiO_2 which are screened by electrons in graphene) or are at the interface of graphene and the substrate (residual extrinsic charges formed during the graphene synthesis process etc). These charged impurities create a spatially inhomogeneous potential distribution in the graphene plane resulting in the formation of electron-hole puddles. Carrier transport described using the self-consistent random phase approximation (RPA)-Boltzmann formalism [27] predicts a strong dependence of the minimum conductivity on the impurity density, as given below

$$\sigma(n) = Ce\frac{n}{n_{imp}} + \sigma_{res}, \tag{1.7}$$

where e is the electronic charge, C is a constant which is calculated to be C = $5 \times 10^{15}\mathrm{V}^{-1}\mathrm{s}^{-1}$ for SiO_2 , n is charge carrier density, n_{imp} is the defect density, and σ_{res} is the residual conductivity at n=0. Furthermore, this charged impurity theory is capable of predicting field effect mobility

($\mu = \sigma/ne$) as a function of impurity density [27] as:

$$\mu = \frac{\mathrm{C}}{\mathrm{n_{imp}}} \approx \frac{5 \times 10^{15} \mathrm{V^{-1}s^{-1}}}{\mathrm{n_{imp}}} \tag{1.8}$$

The above formalism predicts that minimum conductivity can vary from $20e^2/h$ to $4e^2/h$ depending on the charged impurity density, which contradicts the earlier experimental study indicating a universal minimum conductivity [28]. Chen et al. [29] experimentally investigated the impact of charge impurities on the transport properties of graphene on $\mathrm{SiO_2}$. In their study a controlled amount of charge scatterers are successively introduced to otherwise atomically clean graphene devices. They demonstrated the effect of charged impurities on the high-carrier density conductivity of the graphene, showing consistency with the theoretical calculations discussed above [27],[30]. Authors implied that the success of the theory in explaining the potassium doping experiments shows that the theory describes the native scatterers. Yet, experiments performed on graphene on different substrates and dielectric environments show that Coulomb impurities are not limiting the mobility in graphene [31].

1.5.1.3 Ripples:

Ripples can result from the intrinsic instability of the graphene crystal or originate during mechanical fabrication of graphene, which relies on the van der Waals interaction between the $\mathrm{SiO_2}$ substrate and the graphene. Scanning Tunneling Microscope (STM) topography of the graphene sheet shows that it is not atomically flat on the $\mathrm{SiO_2}$ surface but has nanometer-sized ripples [32]. These ripples are caused by the roughness of the thermally grown $\mathrm{SiO_2}$ substrate. Theoretical studies [33] show that ripples induce weak, yet finite scattering. The conductivity is given by

$$\sigma_{corr}(n) = C_{corr} e n^{2H-1}, \tag{1.9}$$

where exponent H gives the fractal dimension of the ripples, and$C_{corr} \propto (\frac{r}{z})^2$, where r is the radius and z is the height of the ripples. Ishigami et al. [32], experimentally observed that the height of the ripples is due to the roughness of SiO_2 and $2H \approx 1$, this will give $\sigma(n)$ constant (contrary to experimentally observed linear conductivity $\sigma(n)$). However, Meyer et al. [34] performed TEM studies of suspended graphene membranes, obtaining $2H \approx 2$ and a linear relationship between z and r. Here the ripples exert long-range scattering and result in a linear conductivity with carrier density. These two contradictory experimental results make the contribution of ripples to scattering of charge carriers in graphene unclear. Also graphene exfoliated on atomically flat substrates like mica has fewer ripples [35] but still its mobility is similar to that of graphene on SiO_2. There is sufficient experimental evidence, to suggest that ripples are not a dominant charge scattering source in graphene on SiO_2.

1.5.1.4 Resonant Impurities:

Charge carrier transport in graphene can also be limited by resonant scatterers [36],[37],[38]. These scatterers can be adsorbed chemical species or atomic vacancies in the graphene crystal [39] which give rise to resonance states called "midgap states" near Dirac point. These strong adsorbates exert short-range scattering potentials, inducing intervalley scattering. Theoretical calculations performed considering resonant scatterers in graphene give conductivity dependence on the concentration of these resonant impurities as

$$\sigma \propto n(ln^2(k_F R)), \tag{1.10}$$

where R is the radius of the adsorbate [36],[37],[38]. Chen et al. [40] created vacancies in graphene using high energy He and Ne ion bombardment and obtained results consistent with scattering by

midgap states.

1.5.2. Molybdenum disulfide

1.5.2.1 Coulomb scattering at charge impurities:

Like graphene, the mobility of charge carriers in $\mathrm{MoS_2}$ at low temperature can be highly influenced by charge impurities from the host substrate or device environment. The coulomb scattering can be reduced by placing $\mathrm{MoS_2}$ in a high dielectric environment. It has been recently shown that $\mathrm{MoS_2}$ devices capped with high dielectric insulator indeed exhibit larger mobilities as compared to samples placed on $\mathrm{SiO_2}$ [15].

1.5.2.2 Roughness scattering:

In the case of freely standing $\mathrm{MoS_2}$, ripples of $\sim$1nm height are seen which can also potentially reduce its mobility [41]. So far the role of these ripples on the scattering of charge carriers in $\mathrm{MoS_2}$ has not been experimentally investigated.

1.5.2.3 Phonon scattering:

The mobility of charge carriers generally decreases with increasing temperature due to fact that phonon scattering scales with temperature. Using first principle Kaasbjerg et al. [41] calculated the temperature dependence of the mobility in single layer $\mathrm{MoS_2}$ as $\mu \propto \mathrm{T}^{-\Upsilon}$, where $\Upsilon = 1.69$ at room temperature. At temperatures below 100 K the acoustic phonons dominate, but at higher temperature the optical phonons dominate. These calculations show that at room temperature the optical phonon scatterers limit mobility of $\mathrm{MoS_2}$ to $410\mathrm{cm^2V^{-1}s^{-1}}$. In the case of top gated $\mathrm{MoS_2}$

devices, the out-of-plane homopolar modes are quenched, which changes Υ to 1.52 and, hence, increases mobility at room temperature by $\sim 70\mathrm{cm}^2\mathrm{V}^{-1}\mathrm{s}^{-1}$.

CHAPTER 2: EXPERIMENTAL TECHNIQUES

2.1. Transport measurement

2.1.1. Device fabrication

2.1.1.1. Development of the technique for graphene-based devices

2.1.1.1.1. Wafer preparation

The first step involves patterning alignment markers on a clean 3 inch SiO_2 (280 nm)/Si wafer by standard photolithography and then depositing Au (60 nm)/ Cr (5 nm) using thermal evaporator. As shown in Figure 2.1, these alignment markers have a coordination system which helps to efficiently map and locate the one atom thick, few micron-sized graphene flakes under the optical microscope later on. Next, this 3 inch wafer is cut into smaller wafers about 10 mm $\times$ 10 mm in size. Before use, the wafers are cleaned by dipping in piranha solution ($H_2SO_4 : H_2O_2$ = 3:1) for about 30 minutes and finally rinsed in DI water.

2.1.1.1.2. Graphene devices

The graphene is mechanically exfoliated from kish graphite, using a residue-free adhesive tape onto clean wafers. Exfoliated layers of graphite are identified under an optical microscope and single layers of graphene are confirmed using Raman spectroscopy, which is discussed in detail in section 2.2. Next, a graphene flake is etched into a 4-point probe geometry. The etch pattern is defined using electron beam lithography (e-beam) and then etched with O_2 plasma.

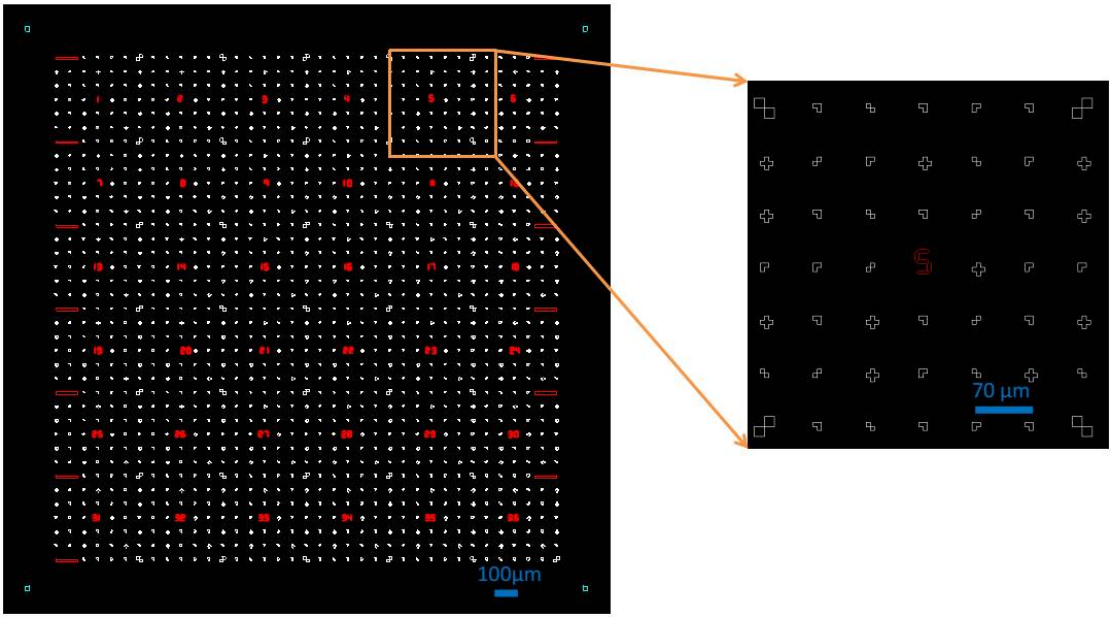

Figure 2.1: Pattern of alignment markers repeated on the 3" wafer using photolithography.

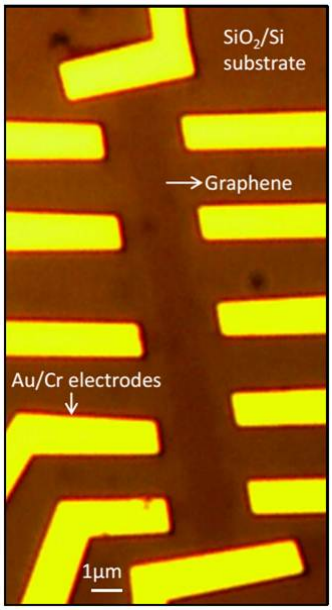

Figure 2.2: An optical micrograph of a graphene device on SiO_2 substrate. The Au (80 nm)/ Cr (5 nm) electrodes were defined using e-beam lithography.

Finally, the contacts are patterned using e-beam lithography and Au (80 nm)/ Cr (5 nm) metal contacts are thermally evaporated. The device channel length and width are typically 2-3 μm and 5-6 μm respectively. Figure 2.2 shows a typical completed graphene device.

2.1.1.2. Failure modes for graphene device fabrication

2.1.1.2.1. Electrode thickness

My experimental studies required an atomically clean graphene device (which will be discussed in detail in the next chapter). However, after device fabrication, the graphene surface can be covered by residual e-beam resist leftover from processing. So, before the transport measurements, the graphene devices are cleaned down to the atomic scale by annealing in continuously flowing $\mathrm{H_2/Ar}$ at $350\,^{\circ}\mathrm{C}$ for 3 hours [32]. In order to survive this annealing step, it is critically important that the electrode metal (Au in this case) is thicker than 50nm.

2.1.1.2.2. Electrode failure

The wafer should be cleaned thoroughly otherwise the Cr sticking layer does not make good contact with the wafer and comes off after hydrogen annealing. The smallest electrodes are generally more prone to be damaged due to poor adhesion, as shown in Figure 2.3. Great care should be taken during device fabrication to use clean tools, fresh chemicals, and an evaporator chamber with a known metal evaporation history, otherwise device contamination can occur.

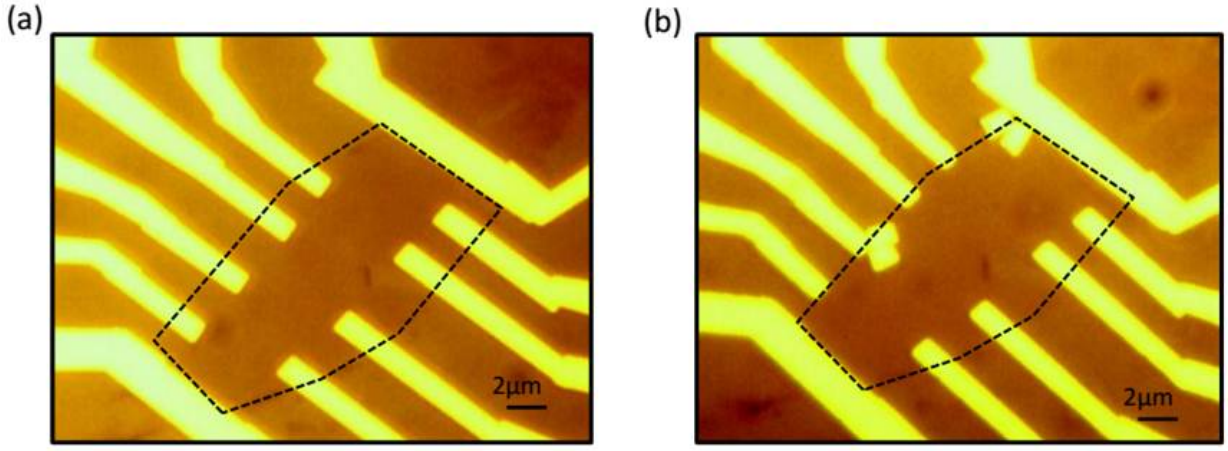

Figure 2.3: (a) Shows the optical image of the graphene device before hydrogen annealing. (b) shows the same graphene device after hydrogen annealing with electrical contacts on one-side ripped.

2.1.1.2.3. Wire bonding

During wire bonding great precaution should be taken to electrically ground the wire bonder, and sample holder to avoid accidental static discharging of the device by physical contact. Also force and power used for bonding should be minimized (just enough to make a bond). The wire bonder can also pass a huge current and blow up the graphene device. This was observed in a scanning electron microscopy (SEM) image of a graphene device on SiO_2 before and after wire bonding as shown in Figure 2.4. So, it is absolutely important to service regularly an old wire bonder in order to avoid such destructive current spikes. This problem has been alleviated upon purchase of a new wire bonder. The wire bonding parameter for graphene device are given in the table below.

Table 2.1: Graphene device wire bonding parameters

Bond	Power	Time	Force
Post	300	30 ms	High
Graphene	240	30 ms	Low

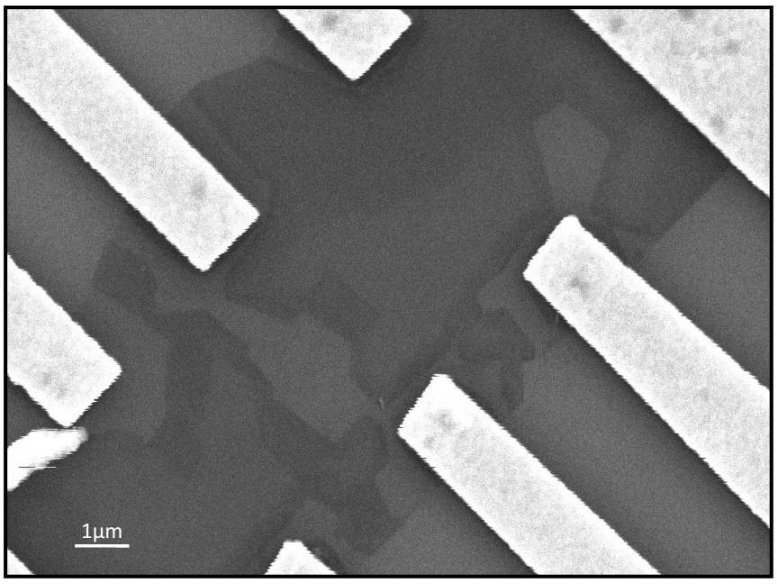

Figure 2.4: Scanning electron microscopy image (SEM) of a blown graphene device, where high current passed by wire bonding tip has torn the graphene.

2.1.2. Ultra high vacuum (UHV) chamber

2.1.2.1. Design

2.1.2.1.1. Helitran LT-3B open cycle cryostat:

The ultra-high-vacuum chamber compatible open-cycle Heli-tran Liquid Transfer Refrigeration System (LT-3B) was manufactured by Advanced Research Systems Inc, shown in Figure 2.5(a) and (b). It is capable of operating in the temperature range of 2 to 300 K. Also, the sample block is fitted with a heater so that the sample can also be heated in UHV up to 500 K.

The liquid helium is transferred into the cryostat through a transfer line by pressurizing the helium dewar. This transfer line has a filter which blocks any dirt from clogging the needle valve and is designed to minimize heat losses.

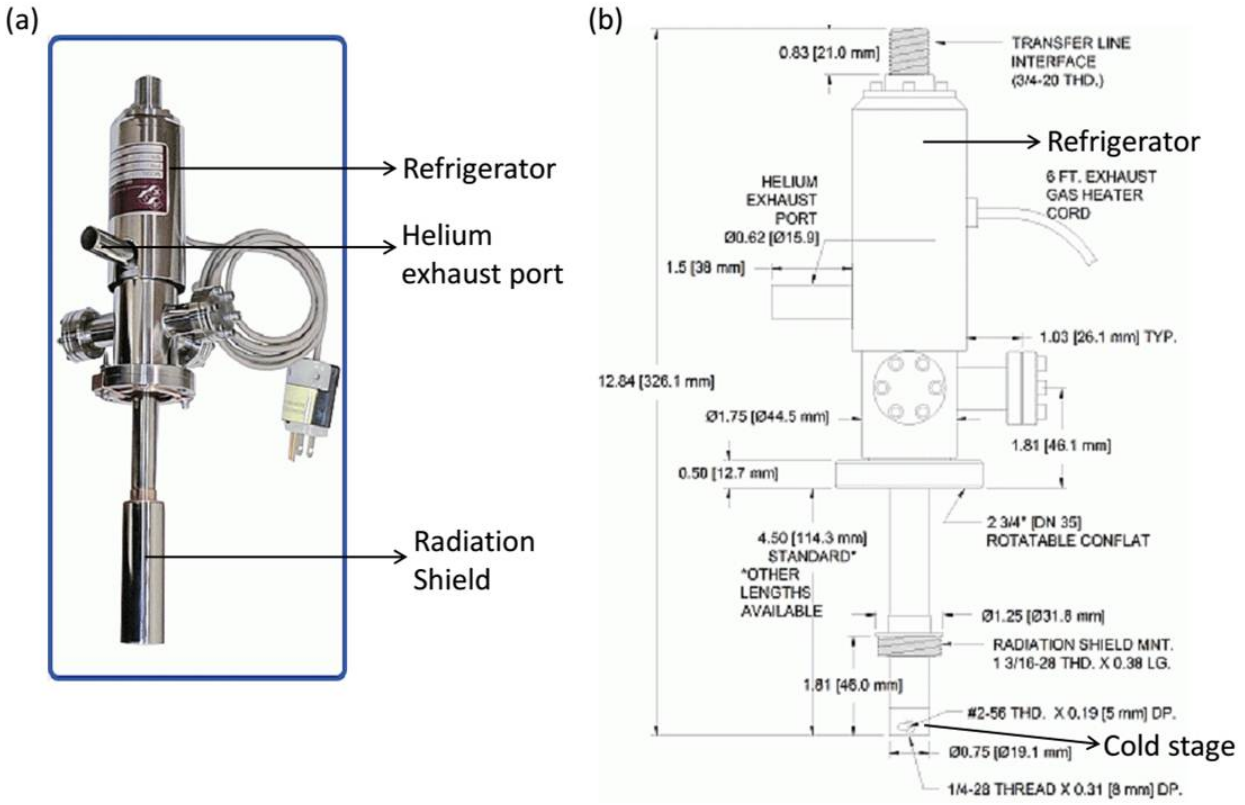

Figure 2.5: (a) Heli-tran LT-3B cryostat. (b) The drawing of the Heli-tran with dimensions from Advanced Research Systems Inc.

A needle valve is at the end of the transfer tube that goes in the cryostat and it directs the liquid flow into the heat exchanger. The heat exchanger can be regulated by adjusting the threaded interface. The heat exchanger, as name suggests acts as an interface for the sample holder. Figure 2.6 shows a simplified design of the cryostat. The sample holder is cooled down by a continuous liquid helium flow through cryostat and the helium gas exhaust comes out of the exhaust port.

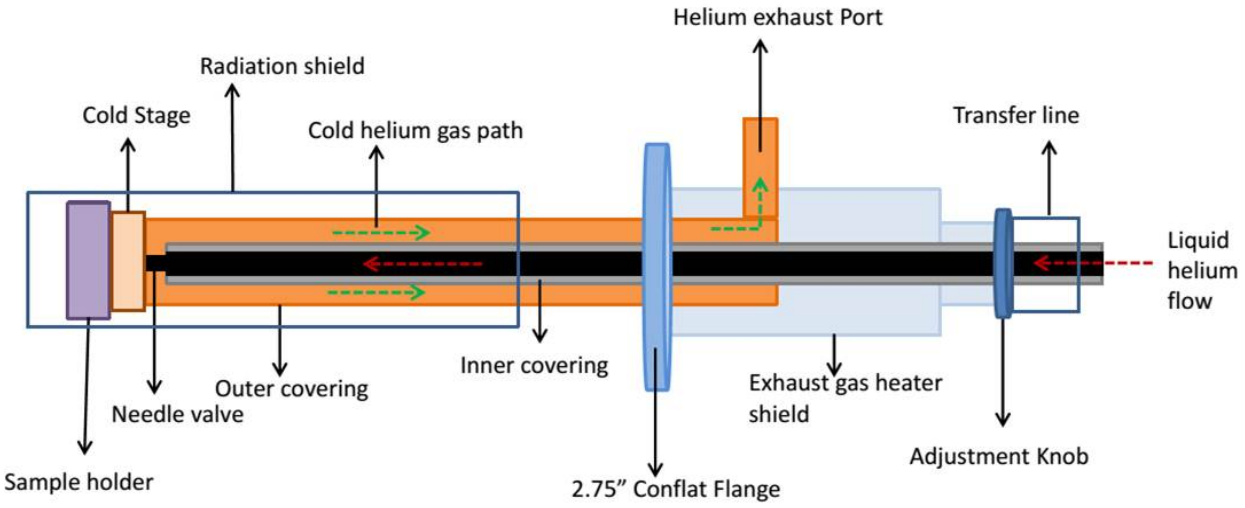

Figure 2.6: Schematic of the internal structure of the cryostat design in Heli-tran LT-3B.

A radiation shield which is cooled down using exhausted helium from the heat exchanger, minimizes the heat loss. Typically, cool down from 300 K to 10 K takes about 40 mins and at low temperature the helium consumption is about 1.5 liters/hr. UHV and low temperature compatible manganin wire of 0.005 mm diameter, 290 Ωcm specific resistance is used for electrical wiring of the helitran. The electrical wires are wrapped around the cryostat such that there is enough thermal anchoring to further minimize the heat losses as shown in Figure 2.7.

2.1.2.1.2. Hydrogen cracker:

Figure 2.8 a) shows the commercially available atomic hydrogen source EFM H from Omicron Nanotechnology/Focus GmbH. It consists of mainly three parts: the gas inlet, the cooling unit, and the tungsten capillary as shown in the schematic of the EMF H in Figure 2.8(b). It is based on the principle of dissociating hydrogen gas by heating to high temperature. Through a leak valve, a controlled amount of molecular hydrogen is passed into the tungsten filament, which is heated to 2600 K by electron bombardment, ensuring that almost all of the hydrogen dissociates.

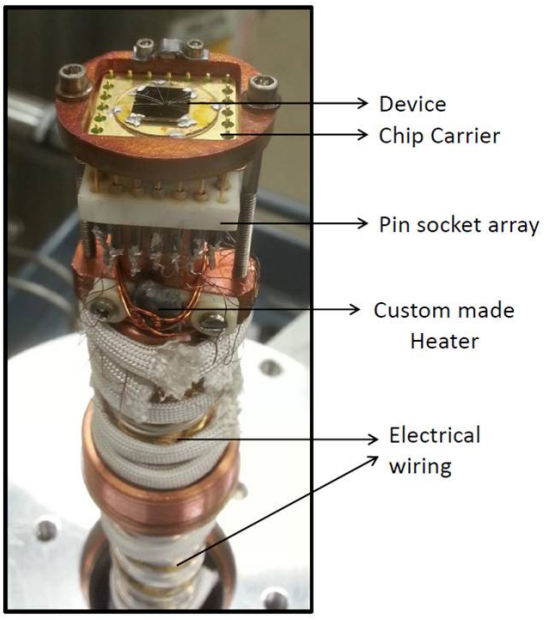

Figure 2.7: Picture showing LT-3B cryostat with the wiring and a device.

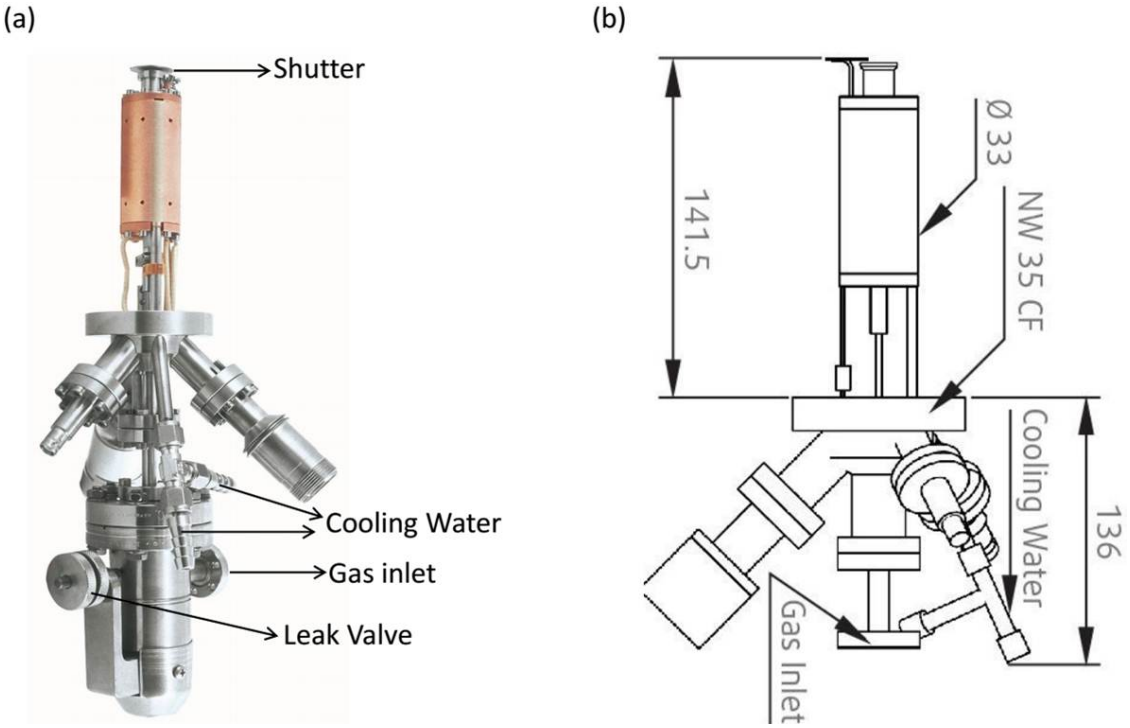

Figure 2.8: (a) Atomic hydrogen source EFM H from Omicron Nanotechnology/Focus GmbH. (b) The schematic of the atomic hydrogen cracker showing physical dimensions, showing clearly the cooling water lines, gas inlet, and tungsten capillary [Source: Omicron Nanotechnology].

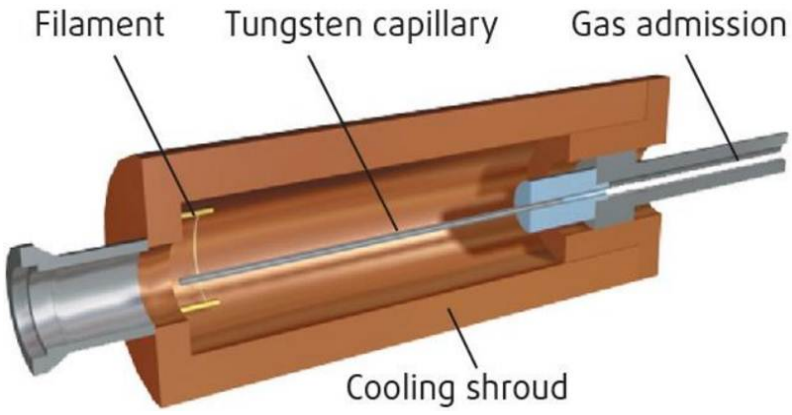

Figure 2.9: Schematic of the cooling shroud in the atomic hydrogen cracker. This shroud enables the system to maintain the low base pressure of 10^{-10} mbar at the heater filament, which helps to get a reproducible angular distribution of atomic hydrogen [Source: Omicron Nanotechnology].

Figure 2.9 shows the schematic of the cooling shroud, which enable the hydrogen cracker to maintain low base pressure of 10^{-10} mbar in the capillary heater. The tungsten capillary is carefully pre-adjusted at a fixed position in the center to get a reproducible angular distribution of atomic hydrogen, which is dependent on the pressure and temperature of the tungsten capillary. Higher pressure results in a broad distribution, while low pressure gives a sharper distribution profile. Figure 2.10 shows the spot profile of the hydrogen cracker as a function of different heating powers. Higher power corresponds to higher temperature, hence it gives a sharper angular distribution. Moreover, the hydrogen cracker is equipped with a shutter in direct sight of the hydrogen beam that allows precise hydrogen dosage as well as protects sample during degassing of the filament.

Faraday cup measurements: During the cracking of hydrogen gas at high temperature, a small amount of hydrogen ions may also be generated. For my experimental study it is essential to expose the sample to pure atomic hydrogen (explained in next chapter). I mounted a Faraday cup in place of the sample holder in order to measure ion current. With the filament heated at 60 Watts, upon opening the shutter a negatively charged ion current of about 2.3μA was measured.

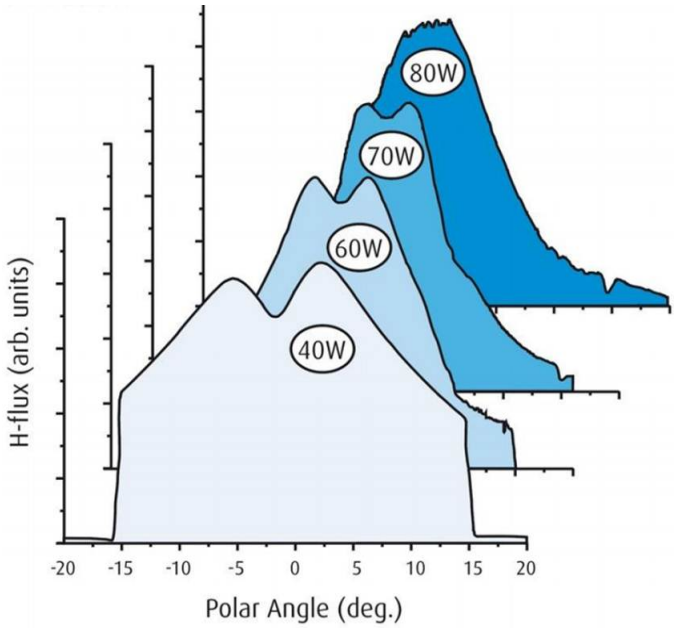

Figure 2.10: : The spot profile of the hydrogen cracker as a function of different heating powers. Higher power gives a sharper angular distribution [Source: Omicron Nanotechnology].

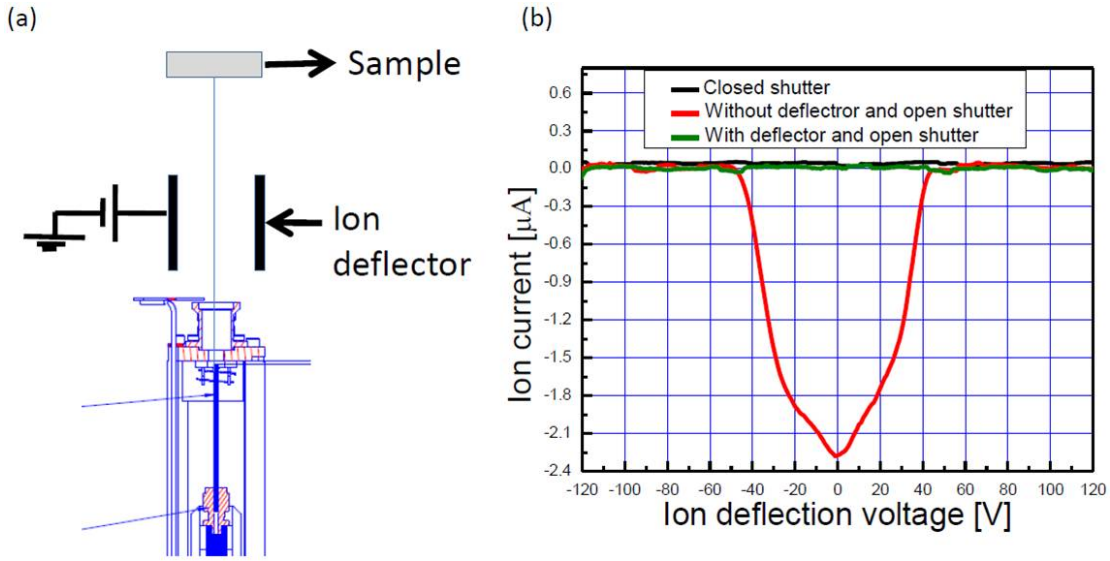

Figure 2.11: : (a) Hydrogen cracker with a ion deflector system and (b) Ion current measurements using Faraday cup with hydrogen cracker shutter closed, open shutter with no deflector, and open shutter with deflector. These measurements clearly indicate that there is a small ion current which can be quenched to almost negligible values by using a deflector.

The path of these ions can be easily deviated by employing an electric deflector between the hydrogen cracker and the sample as shown in the Figure 2.11(a). The ions are deflected by applying +210V across the parallel stainless steel plates. Figure 2.11(b) shows the comparison of the ion current with shutter closed, open, and open with the ion deflector in place, as a function of deflecting voltage. It is clearly seen that, using the deflector, the ion current becomes negligible as all the negatively charged ions are deflected away from the Faraday cup.

2.1.2.1.3 Experimental setup:

The chip carrier with a graphene device is mounted in the pin socket array on the Heli-tran. Figure 2.12 shows the schematic of the experimental setup. The Heli-tran goes upside down into the top of the chamber that device has direct line of sight to the hydrogen cracker, which is fitted at the bottom of the chamber. The sample is at a distance of about $11.28^{"}$ from the hydrogen cracker. A movable shutter is inserted from the side $1/4^{"}$ port to cover the radiation shield during outgassing of the hydrogen cracker. During the measurements, the radiation shield and hydrogen cracker shutters help to precisely control the hydrogen dosage to the device. A mass spectrometer, Residual Gas Analyser (RGA) 200 from Stanford Research Systems, is employed to detect any leaks in the UHV chamber and to check the residual gas content after baking out the chamber. A Valcon Plus 300 combination pump (Star Cell ion pump and Titanium Sublimation Pump combination) from Varian Vacuum technologies is used for efficient pumping of hydrogen and noble gases.

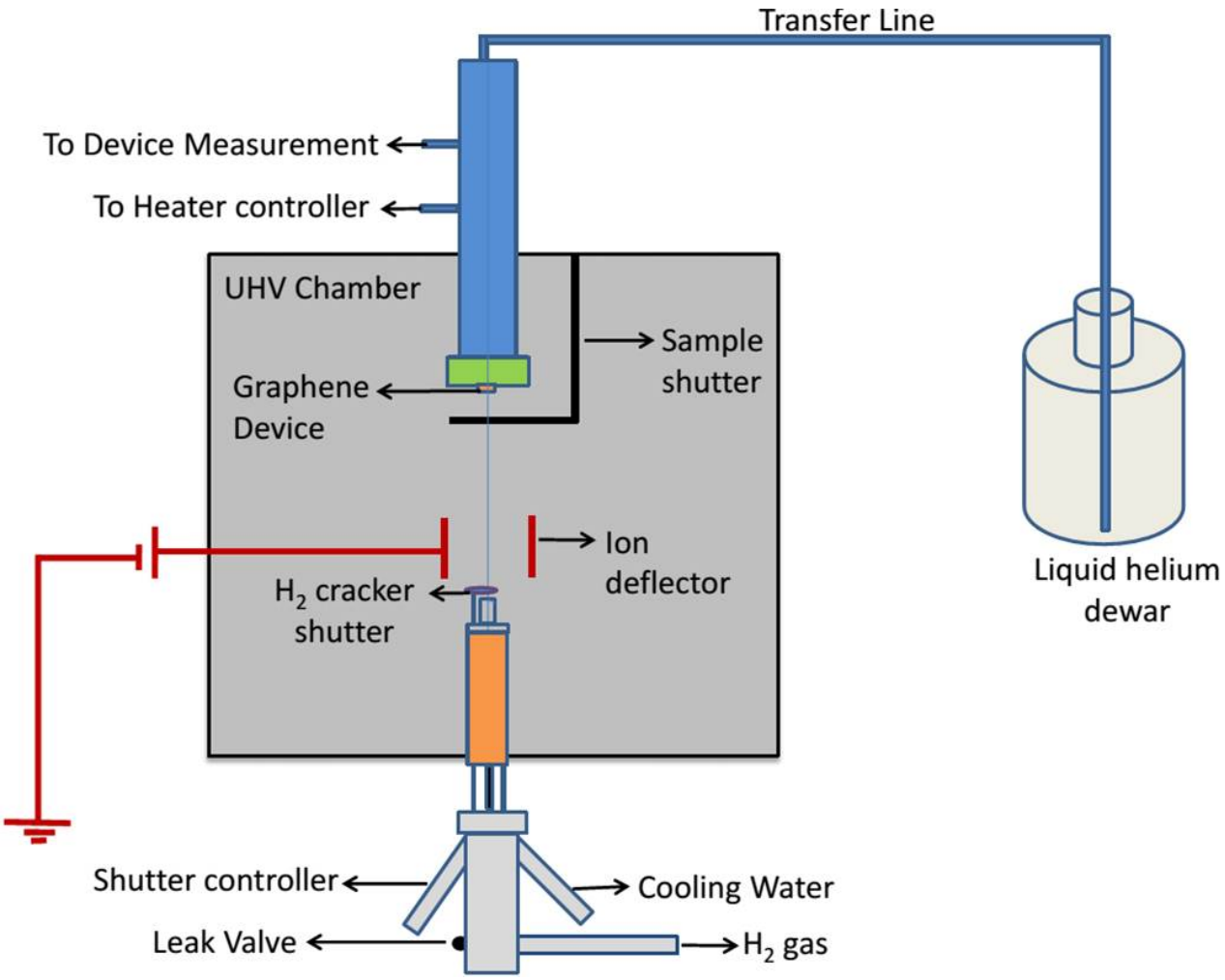

Figure 2.12: : Schematic of the UHV experimental setup at liquid helium temperature.

2.1.2.1.4 Electrical measurements:

The transport measurements of the graphene devices were carried out in our ultra-high vacuum chamber using quasi-DC measurements. Figure 2.13 shows a schematic of the 4-probe device measurement setup. A Keithley 2400 is used to apply back gate voltage to the Si wafer through R_g (100 MΩ resistor), which acts a current limiting resistor that protects the graphene in case of a short-circuit between the graphene and the gate. The back Si gate voltage varies the charge carrier density in graphene.

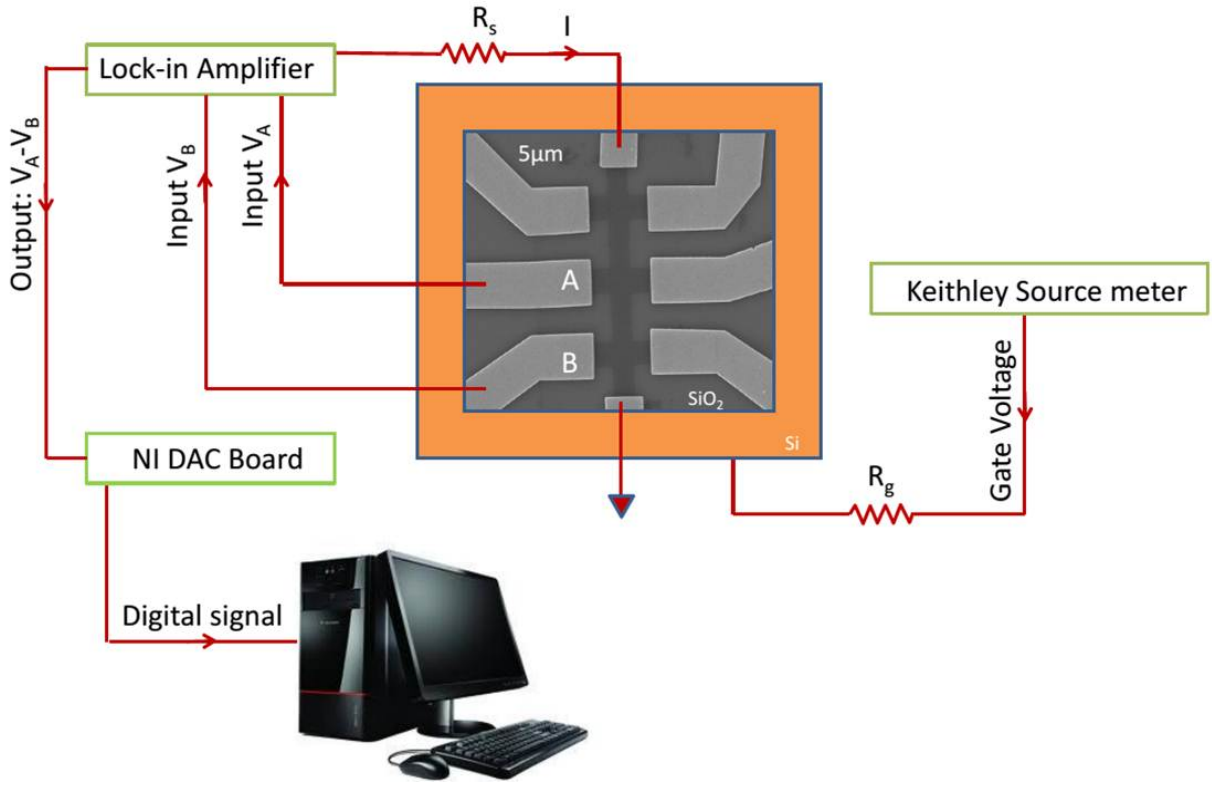

Figure 2.13: : Four probe graphene device measurement setup, using a lock-in amplifier.

A lock-in amplifier is used to generate a reference voltage $(\sim 1\mathrm{V})$ at a reference frequency (sine wave signal $\sim$167.16 Hz), which is sent to excite the experiment. The response of the graphene to this signal is measured by the lock-in amplifier by phase-sensitive detection, which gets rid of all electrical noise and gives a response only at the reference frequency [42]. The reference voltage signal is converted to current by the R_s resistor $(10\ \mathrm{M}\Omega)$ which is connected to the source electrode of the device. The drain electrode is grounded during measurement. The voltage difference is measured across two other electrodes, i.e., $\mathrm{V_A} - \mathrm{V_B}$, by using the lock-in amplifier. The output of lock-in amplifier is connected to a DAC (Digital to analog converter) board. All these physical instruments are interfaced to the computer and controlled by a Labview program. Another Keithley sourcemeter (2010) is used to apply +210V to the hydrogen ion deflection system during usage of the hydrogen cracker.

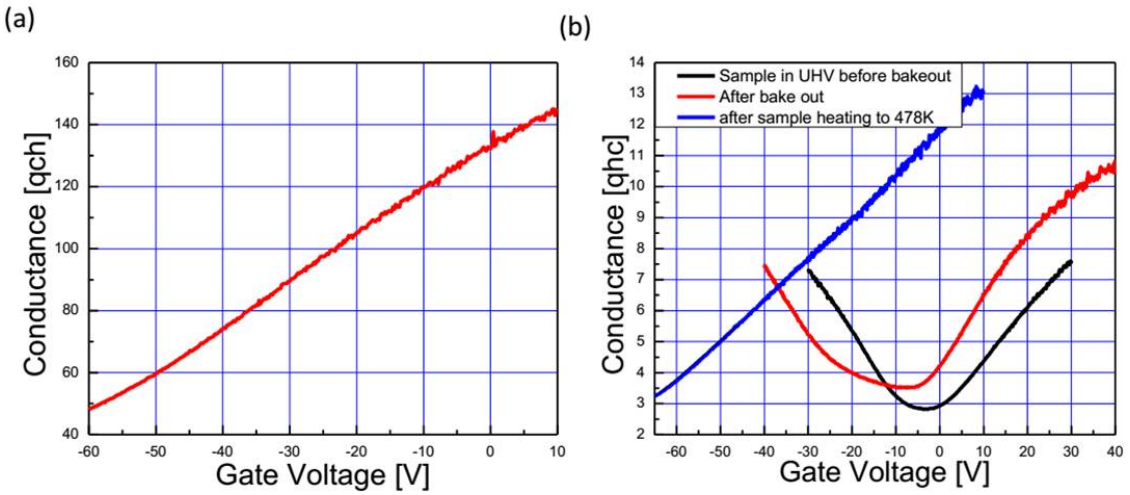

Figure 2.14: : Conductance as a function of gate voltage for two different graphene devices on SiO_2. (a) Device labeled J3 shows conductance minimum point shifted beyond -60 V after 24hr device annealing at 480 K in UHV, indicating the sample to be heavily negatively doped. (b) Another device labeled J35 similarly shows shift in the conductance minimum point after UHV annealing.

2.1.2.2 Contamination issues:

Typically the electrical transport measurement of an undoped mesoscopic graphene device has minimum conductivity ($\sigma_{\min}$) at or near zero gate voltage. The gate voltage at which conductivity is minimized is called $V_{\min}$. This shift in minimum conductivity point to negative (positive) gate voltage indicates electron (hole) doping of the sample. Figure 2.14(a) shows the measured conductance of a graphene device labeled J3 after overnight device annealing in UHV at 480 K. It has the conductance minimum point unusually shifted beyond -60 V gate voltage, which means that this sample is heavily doped. As shown in Figure 2.14(b), for another device labeled J35, the transport measurements were done in successive steps: in vacuum, after bake out and after device annealing at 478 K, again has $V_{\min}$ negatively shifted after annealing. This unusual large shift of $V_{\min}$ beyond -50V clearly points to possible contamination (extrinsic doping) of the graphene device.

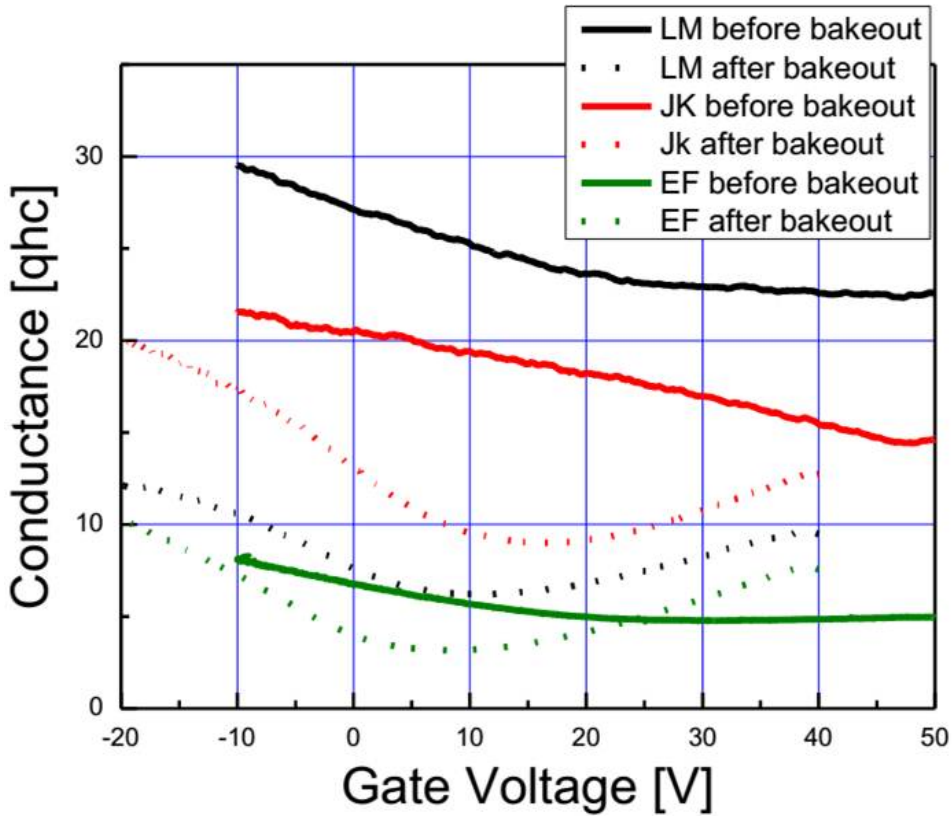

Figure 2.15: : Transport measurements of three two-probe devices labeled LM, LI and EF before and after chamber bake out. Before and after bake out, each of these devices exhibit positive doping, indicating no contamination during bake out and outgassing of the filaments.

The possible contamination source are: device fabrication, hydrogen annealing process, wire bonding, UHV chamber, helitran contamination, and device heater. I measured three two-probe graphene devices labeled LM, EF and JK to systematically rule out other possibilities and identify the source of contamination. Figure 2.15 shows the transport characteristics of these devices measured in the Heli-tran before and after bakeout of the UHV chamber. Each of these devices exhibits positive doping of the graphene before and after chamber bake out, indicating no contamination due to hydrogen annealing, device fabrication, chamber bake out, or outgassing of filaments in UHV. Next, these devices were measured after annealing in UHV using a button heater (without the Heli-tran).

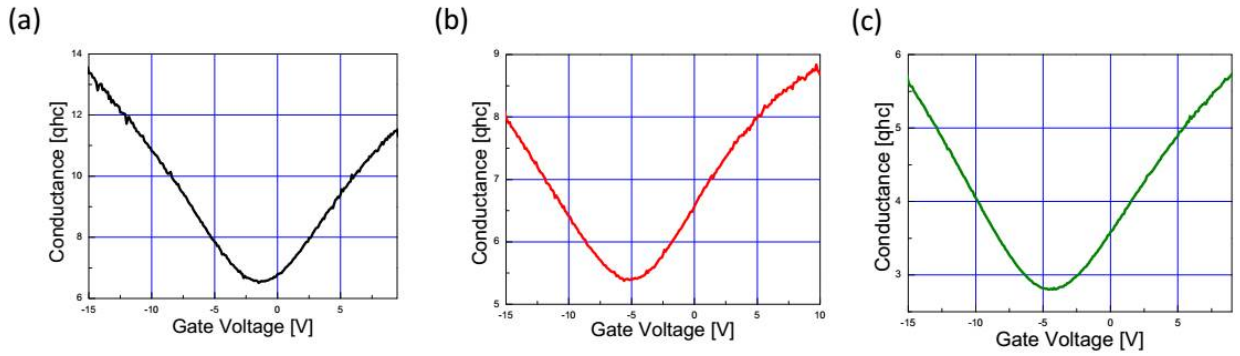

Figure 2.16: : Transport measurement of graphene devices, using button heater (without Heli-tran) (a) Device EF, (b), Device LM and (c) Device KJ show slight shift in V_{min} to negative gate voltage after device annealing, ruling out hydrogen annealing, and UHV chamber contamination

The transport measurements shown in Figure 2.16(a),(b) and (c), rule out device annealing, and UHV chamber as a source of contamination, as we observe only slight shift of V_{min} to negative voltage.

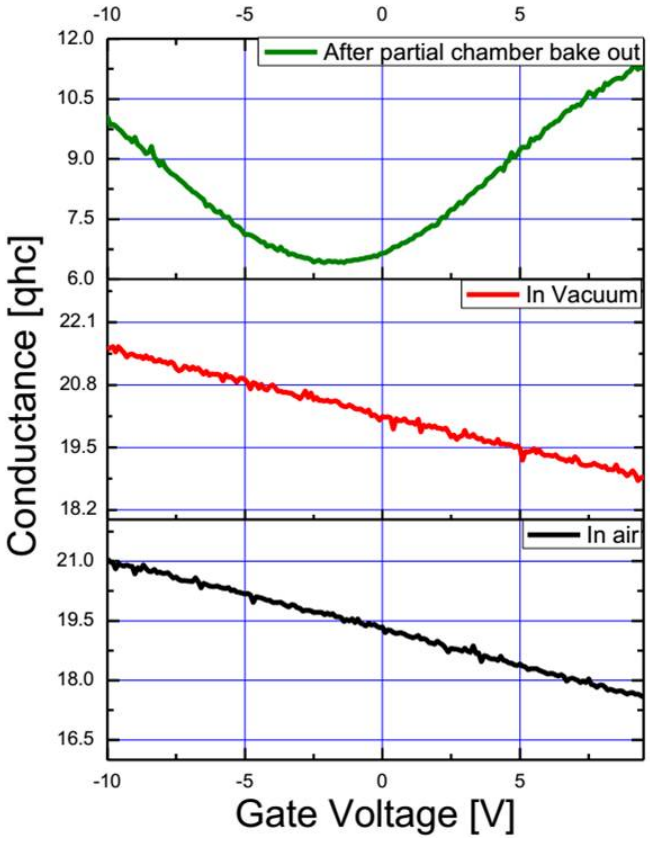

Figure 2.17: : Transport measurements of device labeled EF plugged into the Heli-tran without heating showed slightly negative doping after chamber bake out, indicating no contamination from Heli-tran and UHV chamber.

Next, we tested the Heli-tran without heater. For this we plugged these devices in Heli-tran and carried out transport measurements. Figure 2.17 shows the data obtained, which confirms that Heli-tran and UHV chamber are not contaminated. Furthermore, when these devices were heated using the heater V_{min} shifted to negative gate voltage as shown in Figure 2.18 (a), (b), and (c), indicating the heater to be the source of contamination.

On inspecting the heater, the black color contamination was visible as shown in Figure 2.19. It turned out that Advanced Research Systems (ARS) Inc. used stycast to glue down the heater on the cryostat.

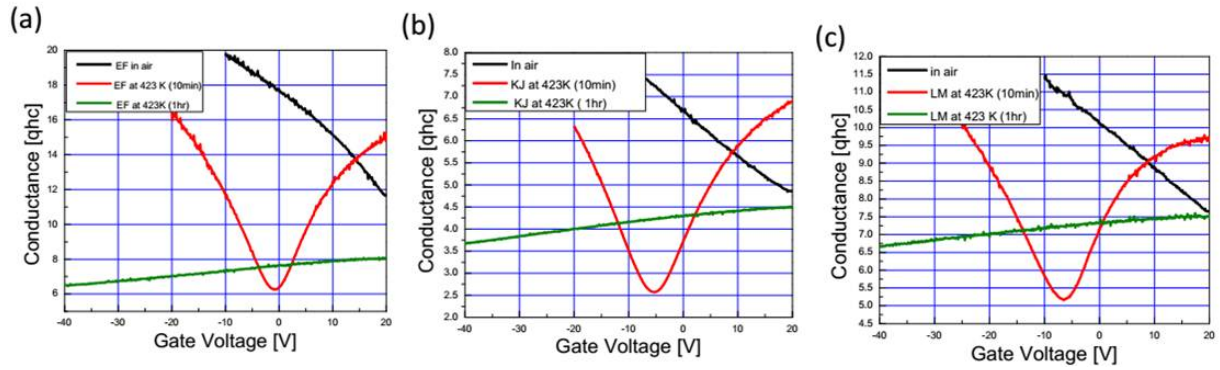

Figure 2.18: : (a) EF, (b) KJ and (c) LM: The Transport measurement of each of these devices shows shift of V_{min} to beyond -40 V after 1 hr annealing at 423 K in UHV chamber with the heater.

Figure 2.19: : (a), (b) Pictures showing heater with black color residue from outgassing of the stycast, and (c) Picture showing black color contamination on the wire selves used for tying the wiring on the Helit-ran.

Stycast is NASA certified to cause very small outgassing (TML and CVCM outgassing of 0.27 % and 0.08 % respectively). However it seems that even this little outgassing was sufficient to negatively dope graphene. Using tungsten wire, I custom made a heater to anneal graphene samples in UHV and obtained typical electrical transport characteristic of graphene (without any sign of contamination) is shown in Figure 2.20.

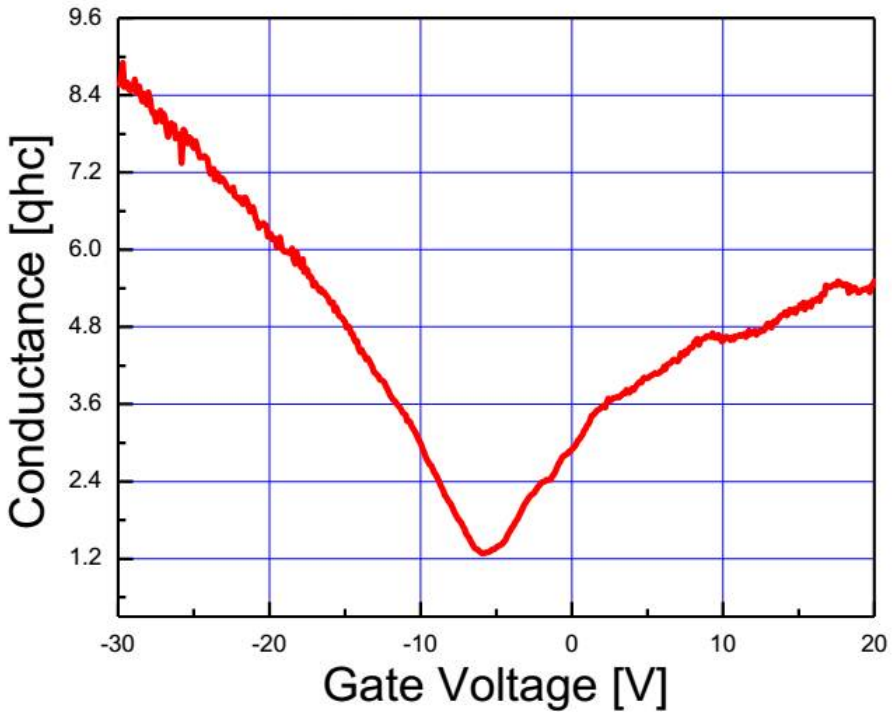

Figure 2.20: : Ambipolar transport characteristic of a two-probe graphene device after 24 hr annealing at in UHV, with minimum conductivity point within $\pm$10V.

2.1.3 Pin socket array

Pin grid arrays (PGAs) are used commercially for packaging integrated circuits. Their compact geometry, large contact density, and commercial availability have also made them useful for nanoscale and atomic physics. In these fundamental science applications, it is often necessary to use ultrahigh vacuum (UHV)-compatible PGAs. Nanoscale materials such as graphene, [43],[44] carbon nanotubes,[45],[46],[47],[48] and nanowires [49] possess extreme sensitivities to adsorbates because of their high surface to volume ratio. Such sensitivities necessitate experiments in UHV in which absolute control over adsorbates can be established. UHV transport measurements at temperatures ranging from 10 to 490 K have been carried out to discover the impact of adsorbates, [29], [50],[51],[52],[53] intentionally created atomic scale defects, [53] and substrate phonons [54] on graphene and nanotubes. UHV-compatible PGAs are used to package nanoscale

devices in these experiments. In atomic physics, there is significant interest in fabricating ion traps on chips with high spatial density [55],[56] for developing atomic clocks and quantum computing technologies. UHV is desired for increasing trapping times and ensuring the purity of trapped atoms and molecules in these experiments, [57],[58] and UHV-compatible PGAs are also used to package these on-chip ion traps. Thus, devices for both nanoscale and atomic physic necessitate UHV-compatible PGAs. Fortunately, these PGAs are readily available and can be purchased from Kyocera (San Diego, CA), Ametek (Lakewood, NJ), and other manufacturers. Since devices are extremely sensitive and do not tolerate soldering, PGAs require their complementary socket arrays (SAs) to establish electronic contacts. Typically, a given instrument has an SA fixed to the vacuum chamber and PGAs are exchanged to measure different devices. Commercial sockets, shown in Figures 2.21 (a) and (b), can be integrated with non-plastic insulating support to assemble SAs for the use in UHV as shown in Figures 2.21(c) and as demonstrated in previous studies.[29],[50],[55],[56]. Yet, these SAs based on commercial sockets should not be considered to be UHV-compatible. The gold plated housing for these commercial sockets, indicated by the shaded region in Figure 2.21(b), is composed of brass. Since the plating is thin and composed of a 0.25μm gold layer with a 1.25μm nickel base layer, even small scratches can cause zinc contamination detrimental to UHV as brass contains zinc. All commercial sockets use similar brass-based housing and, consequently, there are no UHV-compatible sockets available for assembling SAs. To address this, I designed completely UHV compatible sockets, which maintain reliable electronic contact down to cryogenic temperatures and survive repeated insertion-retraction cycles. Its design and construction in discussed in detail below.

Design and Construction of UHV-Compatible sockets and SAs

The cross-sectional mechanical drawing of the UHV compatible socket is shown in Figure 2.22(a). The socket has two components: (1) a gold-plated beryllium copper (BeCu) spring contact and (2) a stainless steel tube.

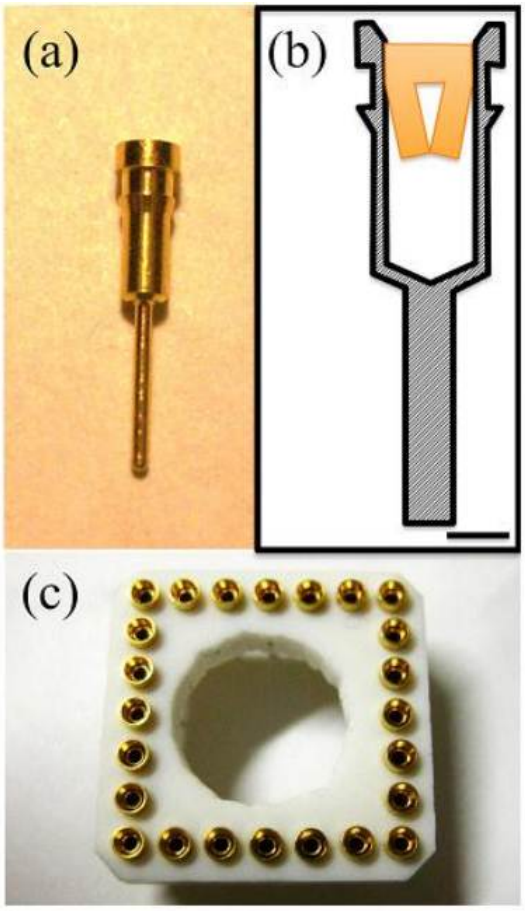

Figure 2.21: : (a) Photograph of a Samtec SC series socket. (b) Schematic cross section of a Samtec SC series socket. The orange region denotes the gold-plated BeCu spring contact. The shaded region represents the gold-plated brass casing for the spring contact. The scale bar is 1/32 in. (c) A socket array for a PGA fabricated from the commercial sockets. The insulating support is made from MACOR ceramic and sockets are glued using nonconductive epoxy.

A gold-plated BeCu spring contact, as shown in Figure 2.22(b), serves as the contacting electrode in the design. Spring contacts can be extracted from Samtec SC series sockets [Figure 2.21(a)]. To retrieve a spring contact, vertical cuts are made at the top of the brass housing of a Samtec socket using a wire cutter. The housing is opened and the spring contact is removed using small tweezers. Spring contacts are very thin and fragile. In order to ensure their survival under repeated insertion-retraction cycles, spring contacts are press-fitted into stainless steel tubes with 1/16 in. outer diameter and 0.010 in. wall thickness as shown in Figure 2.22(c).

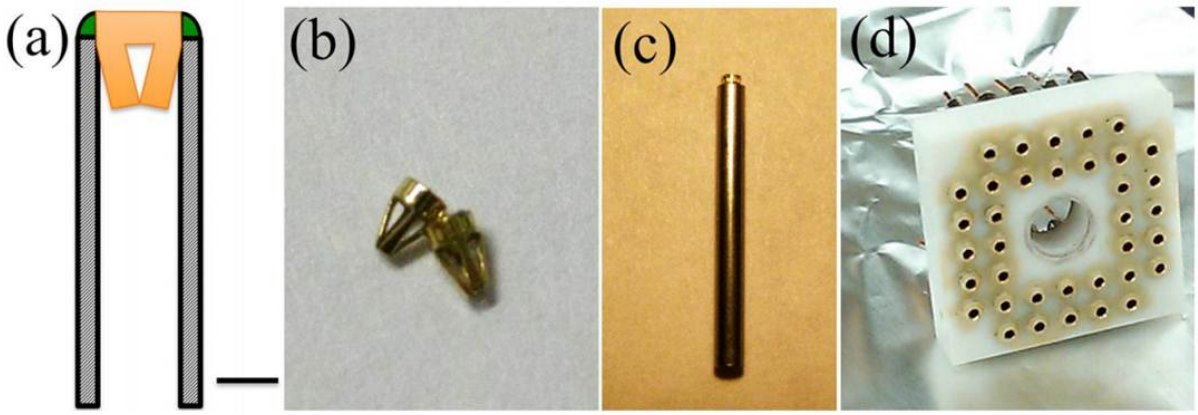

Figure 2.22: : (a) Schematic cross section of the custom socket. The orange region (grey in print) represents the gold-plated BeCu spring contact. The shaded region is the stainless steel tube. The green region represents the epoxy layers. The scale bar is 1/32 in. (b) A photograph of an extracted gold-plated BeCu spring contact. (c) The spring contact press-fitted in a stainless steel tube. (d) A socket array for a PGA fabricated from the custom sockets

Stainless steel tubes are first cut into appropriate lengths using a diamond saw and deburred with a small drill bit. Spring contacts and deburred stainless tubes are cleaned using acetone and isopropanol to remove any residues before press-fitting. Press-fitted contacts are then epoxied to tubes as shown in Figure 2.22(a). We apply conductive epoxy, H20E from Epoxy Technology, Inc (Billerica, MA), along the edge where the contact meets the steel tube. Once the conductive epoxy layer cures, nonconductive epoxy, H77 from Epoxy Technology, Inc. (Billerica, MA), is applied to increase the strength of the bond between the spring contact and the tube. These epoxies survive being baked up to $200\,^{\circ}\mathrm{C}$ without bond failure and with less than 1% of weight loss, according to tests performed by Epoxy Technology. Completed custom sockets are glued into a machinable ceramic plate [Macor, Corning, Inc. (Corning, NY)] with a pattern matching that of a PGA to assemble an SA as shown in Figure 2.22(d). Non conducting epoxy is used for gluing the sockets into the plate. A dummy PGA is used for the bonding procedure to ensure the proper alignment.

Characteristics

The completed custom SA is UHV-compatible, reliable down to low temperatures, and robust

under insertion-retraction cycles. We have performed transport measurements on a graphene device to demonstrate. Any adsorbates, which might be introduced by contamination, can affect the minimum voltage, $\mathrm{V_{min}}$, and the field effect mobility [29]. $\mathrm{V_{min}}$ is the gate voltage at which the conductivity is minimized and the mobility is proportional to the slope of the gate dependent conductivity curve. Figure 2.23 shows transport measurements performed on a graphene device. The device was first introduced into vacuum and baked along with the chamber to establish UHV. Pressures reaching down to 1.8×10^{-10} Torr can be achieved with the custom SA integrated to our UHV cryostat, which is LT-3B purchased from Advanced Research Systems, Inc.(Macungie, PA). Before baking, $\mathrm{V_{min}}$ is located at +2.7 V and after baking, during which the device reaches 380 K, $\mathrm{V_{min}}$ shifts to -1.7 V. The electron mobility improves and the hole mobility is slightly decreased. The observed change in transport property is minimal and can be attributed to changes in the properties of the substrate as substrate-bound adsorbates are desorbed. If the bakeout process did introduce contamination, annealing at higher temperatures should worsen the device. Yet, the transport property remains the same after annealing at 400 K indicating that there are no contaminations. As such, we conclude that the custom SA is UHV-compatible. Figure 2.23 also shows that the custom SA can also maintain reliable electronic contact down to 10 K.

In conclusion we have designed a new socket for PGAs that is UHV compatible and can maintain reliable electronic contact down to 10 K. These sockets can be used to fabricate high contact density SAs, which are useful for nanoscale and atomic physics experiments.

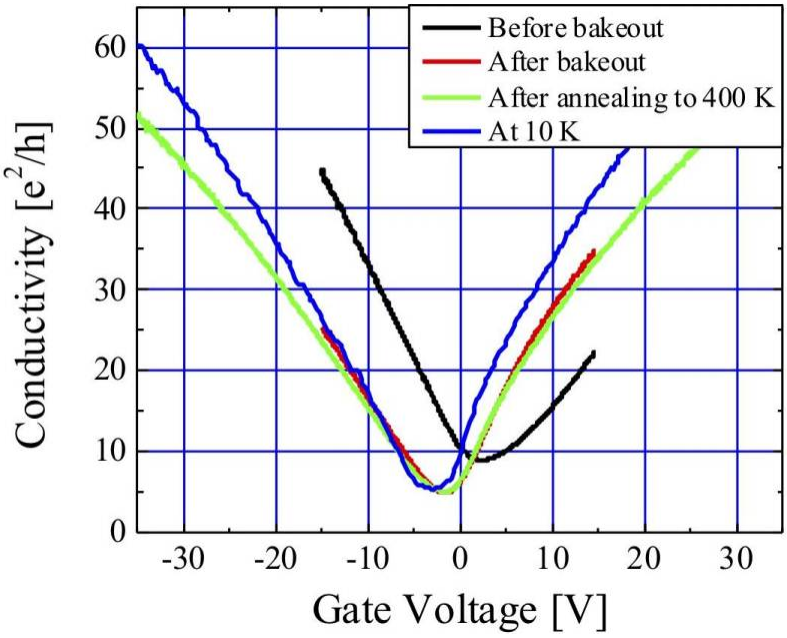

Figure 2.23: : Representative transport measurement performed on a graphene device, showing that the new sockets are UHV-compatible and reliable down to 10 K. Gate-dependent conductivity at room temperature in air, after baking, after annealing at 400 K is shown. In addition, gate dependent conductivity at 10 K is also plotted.

2.2 Raman and photoluminescence spectroscopy

2.2.1 Physical principle

2.2.1.1 Raman spectroscopy

Raman Spectroscopy technique is based on Raman scattering, in which light is inelastically scattered by an atom or molecule. It probes the vibrational and rotational modes of a molecule. An incident photon is absorbed and is reemitted by the atom or molecule at a shifted frequency. The reemitted photon may have a higher (anti-Stokes scattering) or lower (Stokes scattering) frequency than the incident photon. We usually measure the Stokes peaks as they are typically more intense. Since each molecule has its unique vibrational modes, this technique is widely used as a way

to nondestructively characterize a material. It gives information about bond strength, and bond environment.

2.2.1.2 Photoluminescence spectroscopy (PL)

PL is a nondestructive technique to probe electronic states of a material using an optical excitation. When incident photons on a material are absorbed, it undergoes photo-excitation transitions from a lower to a higher electronic states. When the excited state relaxes through a radiative process to the ground state, photons or light is emitted called PL. The quantum yield of PL intensity is related to the amount of radiative and non-radiative recombination rates. Thus PL provides information about electronic states, impurity level, and interface and is vastly used to characterize direct gap semiconductors as discussed in detail below for $\mathrm{MoS_2}$.

2.2.2 Implementation

2.2.2.1 Graphene:

Raman spectroscopy has been successfully used to study doping [59], functionalization [60], strain [61], and edge effects [62] in graphene. Moreover, Raman spectroscopy is the simplest way to identify single layer graphene. Figure 2.24(a) shows the typical Raman spectrum of graphene and graphite. It mainly consists of three peaks: D peak at $1360\mathrm{cm}^{-1}$, G peak at $\sim$ 1560 cm^{-1}, and 2D peak at $\sim 2700\mathrm{cm}^{-1}$. The G peak is due to a high frequency $\mathrm{E_{2g}}$ phonon at the Brillion zone center. The D peak is activated by defects and, therefore, it is used to estimate number of defects in the sample [63]. The 2D peak is a second order of the D peak, which is used to characterize number of layers of graphite.

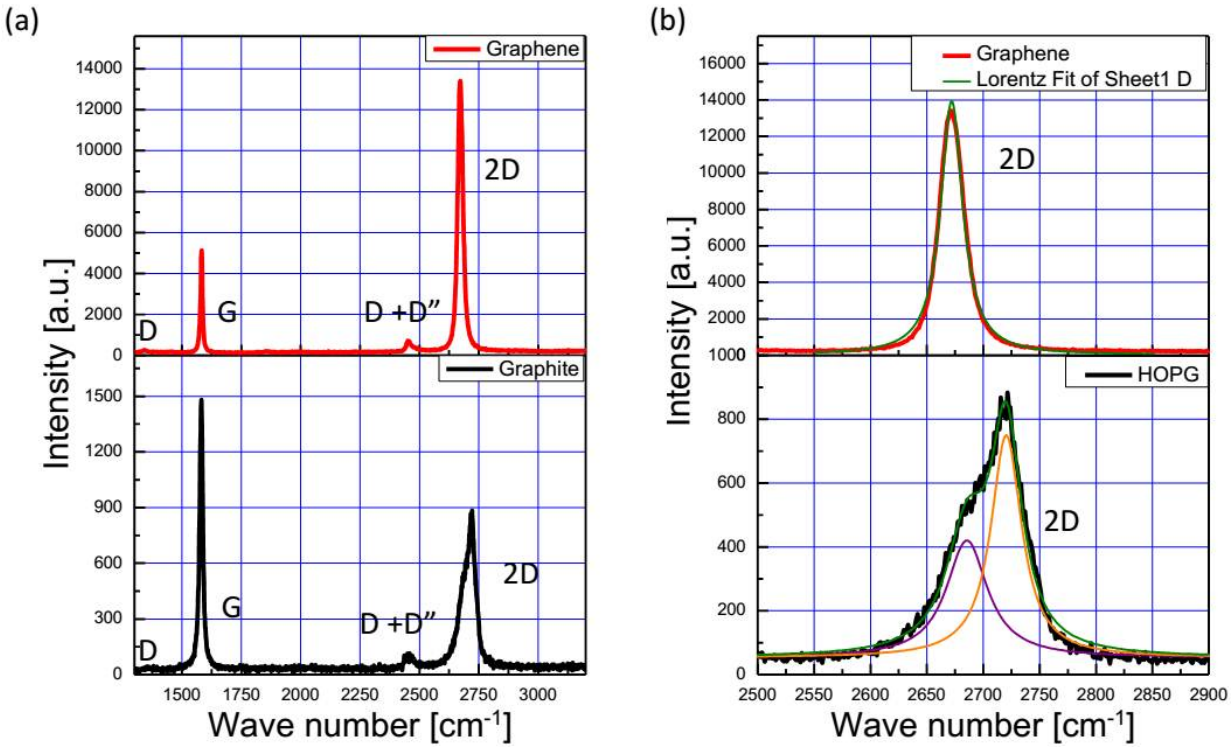

Figure 2.24: : (a) Raman Spectroscopy of graphene (top graph)and graphite (bottom graph) (b) Comparison of 2D peak in graphene (top graph) and graphite (bottom graph). Graphene 2D peak exhibits single Lorentz peak fit with FWHM $\sim 27\mathrm{cm}^{-1}$ and graphite has multiple Lorentz peak fits .

As shown in figure 2.24(b), graphene has a sharp 2D peak at $2675\mathrm{cm}^{-1}$ with single Lorentz fit and FWHM $\sim 27\mathrm{cm}^{-1}$, whereas graphite has the 2D peaks centered at $2700\mathrm{cm}^{-1}$ with multiple peaks Lorentz fits. The shift (blue) in the G and 2D peak indicates doping (hole) of the neutral graphene sample. Moreover, the mono and bi-layer graphenes do not exhibit a photoluminescence signal due to the negligible band gap under normal conditions. However a PL signal is observable in graphene under two possible circumstances as discussed earlier in Chapter 1 section 1.4.1.

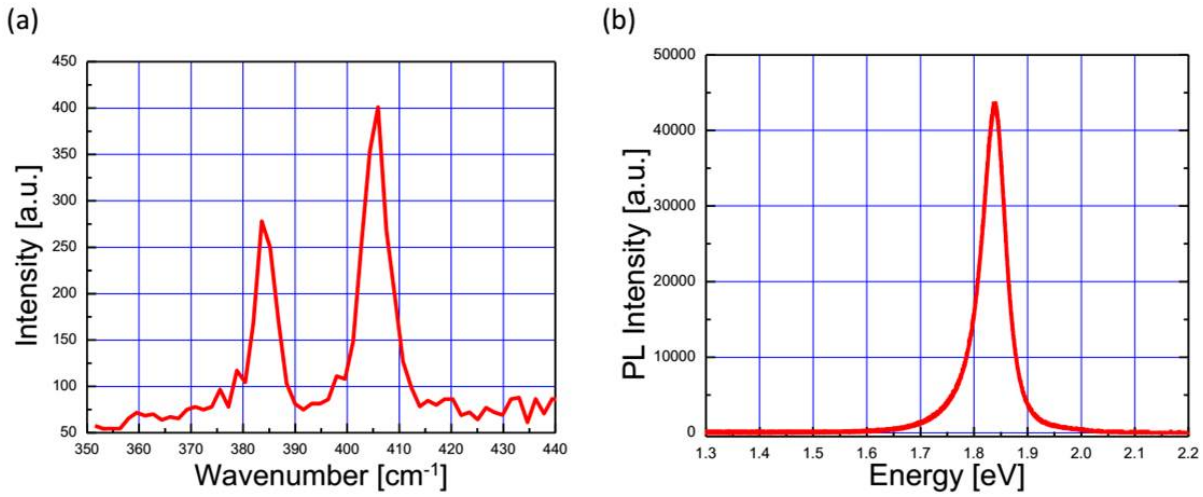

Figure 2.25: : (a) Raman spectroscopy of single layer MoS_2, showing the in plane ($E^{'}_{2g}$) vibration mode at $385cm^{-1}$ and the out of plane vibration mode (A_{1g}) at $405cm^{-1}$. (b) Photoluminescence spectrum of single layer MoS_2, which exhibits a sharp peak at 1.85 eV corresponding to a direct gap in the band structure.

2.2.2.2 Molybedenum disulfide (MoS_2):

As shown in Figure 2.25(a) the Raman spectrum of single-layer of MoS_2 consist of two peaks: a in plane ($E^{'}_{2g}$) and an out of plane vibration mode (A_{1g}) at $385cm^{-1}$ and $405cm^{-1}$, respectively [64]. These two modes are used to identify the number of layers in MoS_2, as the frequency of ($E^{'}_{2g}$) decreases and that of the A_{1g} peak increases with the number of layers of MoS_2. Moreover, single layer MoS_2 is a direct-band gap material with a high intensity PL signal at 1.8 eV, as shown in Figure 2.25(b). Thus, the modification of the electronic structure [65] and doping [66] of MoS_2 can be probed by photoluminescence spectroscopy.

2.3 Scanning tunneling and atomic force microscopy

2.3.1 Principles of STM/AFM

Scanning Tunneling Microscopy (STM): Ever since the development of this technique in 1982 by Binning and Rohrer, it has been an important tool to explore new phenomenon and widen the understanding of the nano-scale physics. It makes it possible to obtain atomic resolution images of surfaces, carry out atomic manipulation, and provides information about local electronic density of states. It is based on the principle that when a bias voltage is applied to a sharp tip and is brought very close (few $\mathring{A}$) to a surface in vacuum, a tunneling current starts flowing from tip to sample (should be conductive). The tunneling current is an exponential function of the separation between the tip and the sample, given as

$$I(z) \propto e^{[-2(2m\phi/\hbar)z]}, \tag{2.1}$$

where z is the distance between the tip apex and the sample, ϕ is the averaged work function between the tip and the sample, m is the mass of the electron, $\hbar$ is the Planck constant, and e the electron charge. So, if the separation increases, the current substantially decreases and vice versa. Figure 2.26 shows the schematic of a scanning tunneling microscope. The tip is mounted on a scanner, which is capable of x, y and z motion. In the constant current mode, as the tip scans over the sample it moves up and down in order to keep a constant separation between the tip and the sample. Thus, the tip movement gives the topography of the sample.

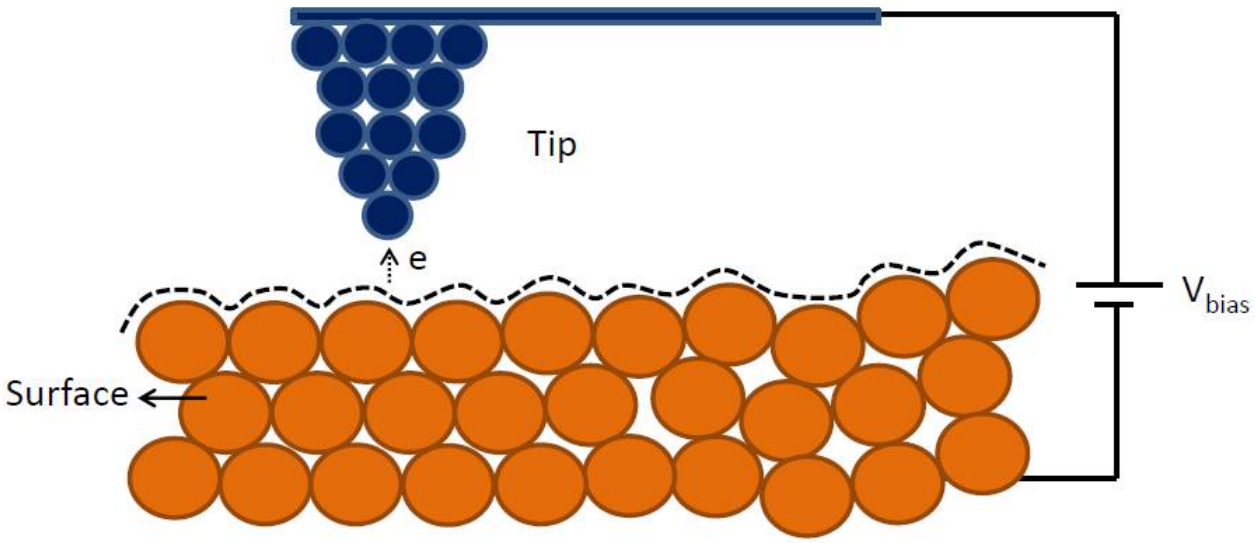

Figure 2.26: : Schematic of Scanning Tunneling microscope (STM).

Non-contact Atomic force microscopy (NC-AFM): A sensor with a tuning fork (Q plus) relies on the long range forces (F_z) between the tip and surface in non-contact atomic force microscopy (NC-AFM) to obtain atomic resolution images of both conductive and non-conductive samples. In the frequency-modulation (FM) mode of the AFM, the tuning fork is vibrated at fixed amplitude, A_{drive}, at a fixed frequency, f_{drive}, which is close to the natural frequency, f_0, of the tuning fork. On approaching close to the surface the, the inelastic and elastic interactions cause the amplitude and the frequency to change relative to the driving signal. This relative change in the frequency signal of the cantilever is used as a feedback signal and gives atomic resolution of the surface.

2.3.2 Implementation

2.3.2.1 STM tip preparation and characterization-

The STM tip is prepared from a tungsten wire of diameter 0.38 mm using electro-chemical method.

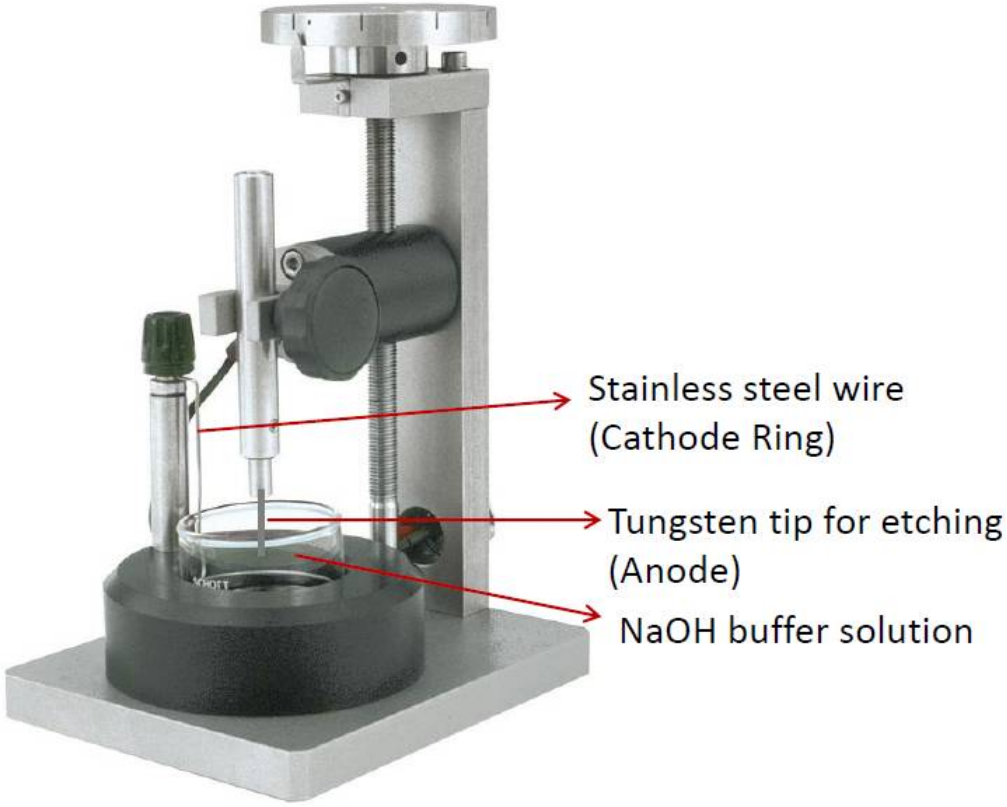

Figure 2.27: : Picture showing tip etching kit from Omicron Nanotechnology to prepare sharp tips (small apex radius) using the differential cut-off procedure. Source [Omicron Nanotechnology].

I used the tip etching Kit from Omicron Nanotechnology to prepare the tips using the differential cut-off procedure as described below. The quality of the etched tip greatly varies with the tip material and etching parameters.

The tungsten wire is cut with a sharp wire cutter to a length of at least 2 mm longer than the final length needed. A ring shaped cathode is made using a stainless steel wire of diameter 1 mm. The tungsten wire, serving as the anode is then lowered into the center of the cathode ring in such way that it is dipped about 2 mm into a beaker filled with a buffer NaOH solution (5.0 N), as shown in the Figure 2.27. Depending on the wire length inserted into the solution the initial current is set 50-70 mA and that the etching voltage (10 V) stops when the current drops below 20 mA.

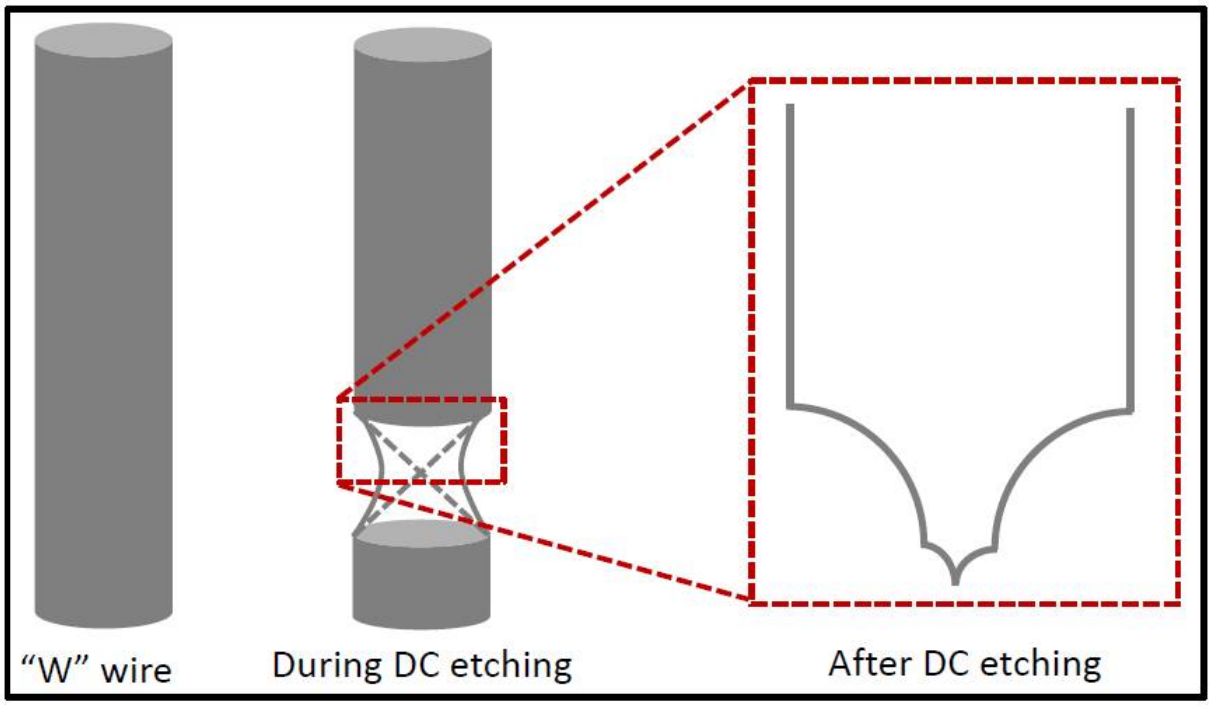

Figure 2.28: : Schematic showing tip shape during tip etching process.

I use sensitivity of 6 which is essential to allow etching voltage to respond appropriately to the tip etching (neither too slow nor too fast). As soon as the etching process ends, the tungsten piece below the cathode ring drops and a sharp piece is obtained as shown in Figure 2.28. The voltage must be turned off when the tungsten piece is dropped to obtain a sharp tip. The tip is next dipped in de-ionized water about 10 times to avoid formation of NaOH crystallites. The tip shape is routinely characterized under microscope. This method can be consistently used to obtain sharp tips. With time, the concentration of NaOH solution needs to be increased to avoid formation of a second meniscus due to decrease in solution level. The tips get oxidized in air, which hampers the tunneling current.

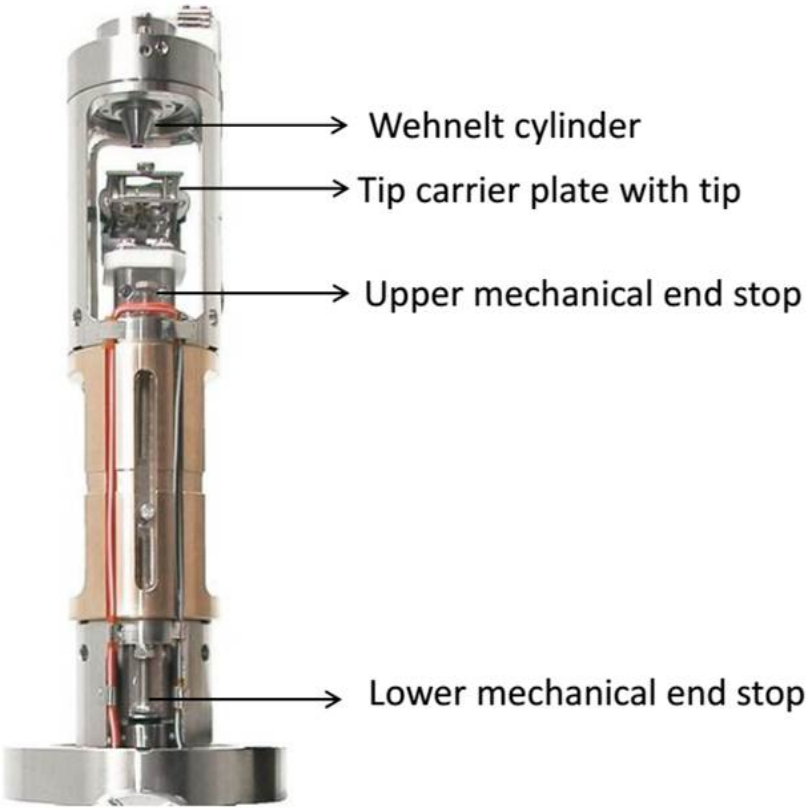

Figure 2.29: : Tip Preparation tool from Omicron Nanotechnology. Source [Omicron Nanotechnology]

I have used two methods to clean the oxide from the tip: in-situ vacuum annealing at 1000 °C and HF etching. Figure 2.29 shows the tip preparation tool from Omicron Nanotechnology, that I mostly used to remove oxide from STM tips in UHV. It has an advantage that it gives reliably sharp tips with stable tunneling current. In this method, the tip is heated to high temperature by electron bombardment from a thoriated tungsten filament. First, the filament current is increased to 1.9 A and biased to 1 KV. Then the tip is brought close ($\sim$1 mm) to the filament until an emission current of 1.67 mA is obtained. The tip is heated at these parameters for 6 sec to completely remove the oxide. Heating for more time makes the tip blunt due to melting. Once the oxide is removed the tip is ready to use for atomic scale imaging. However this method cannot be used to remove the oxide layer from the Q plus sensor with tuning fork for NC- AFM.

In this case the oxide can be easily removed by dipping the NC-AFM/STM tip (only the tip and not the cantilever prongs) in a buffer HF solution. Next, the tip is dipped into de-ionized water and immediately pumped in the STM after inspection under optical microscope. Tips should be etched in the buffer solution for 5 sec. Etching for less than 5 secs resulted in partial oxide removal, whereas etching for more than 5 sec made the tip blunt (large apex radius). This method routinely gives good NC-AFM tips, which helped me to obtain atomic resolution of various surfaces.

This buffer etching technique is not suitable to remove oxide from STM tips, as it does not yield stable a tunneling current, and hence making these tips non-ideal for probing local density of states of the scanning material by scanning tunneling spectroscopy.

2.3.2.2 Device fabrication requirements for STM experiments

2.3.2.2.1 Special provisions for locating samples:

A conducting sample is required in order to perform STM. Exfoliated graphene flakes are usually $20 \times 20 \mu\mathrm{m}^2$ in size. Thus approaching the STM tip onto graphene devices can be very challenging, without crashing the tip into insulating gate dielectric. Although our custom designed STM/AFM from Omicron Nanotechnology has a long focus optical microscope, which improves the device visibility inside the cryostat. However still some device fabrication design modifications are necessary to be able to find and safely approach graphene with the STM tip. For this reason the electrical contacts to graphene are usually made 15-20 μm wide as shown in the Figure 2.30(a). The tip is first approached on one of the 300 μm $\times$ 300 μm contact pads and then it is pulled back about 20-30 steps from the surface. Next, the tip is moved along this particular electrode towards graphene to find the Au/graphene interface. Alternately, for small sized graphene flakes (5 μm $\times$ 5 μm), a one probe device can also be made by completely surrounding graphene as shown in Figure

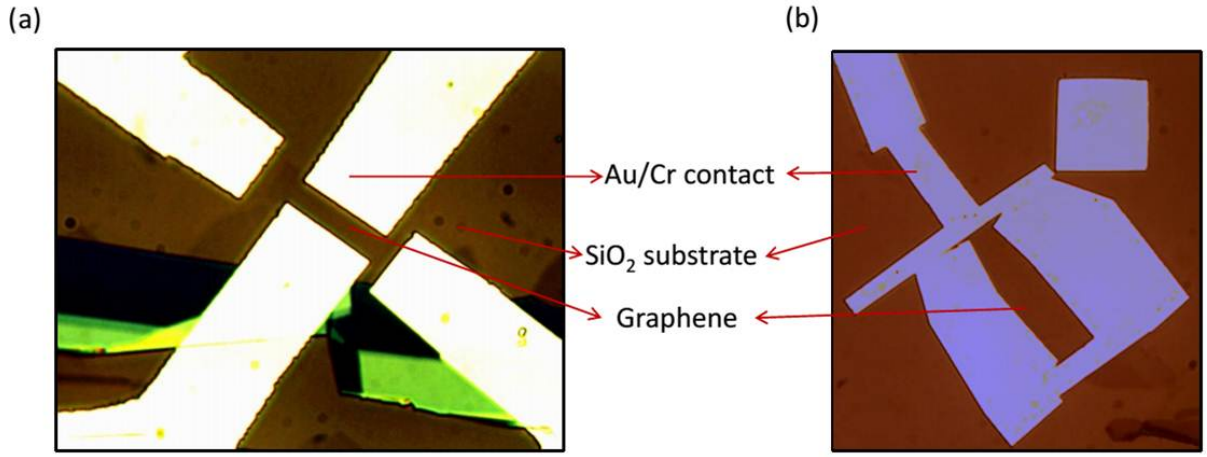

Figure 2.30: : (a)Four probe Au(50 nm)/Cr(5 nm) metal contact on graphene on SiO_2 for STM studies. (b) A one probe metal contact where graphene is surrounded by the contact.

2.30(b). Standard ebeam lithography is employed to pattern the contacts. The Au (50 nm)/Cr (5 nm) metal contacts are evaporated using thermal evaporator. Figure 2.31 shows the optical image of the STM tip approached on graphene device on SiO_2, obtained with the Omicron long focus microscope.

2.3.2.2.2 Device sample plate:

The STM has a special provision to carry out in-situ transport measurements in the low temperature cryostat. The sample plate has four contacts. The design of the contacts make it difficult to wire bond, so four Au contacts were made by the shadow mask method on the insulating sapphire and glued down on the sample plate as shown in the Figure 2.32.

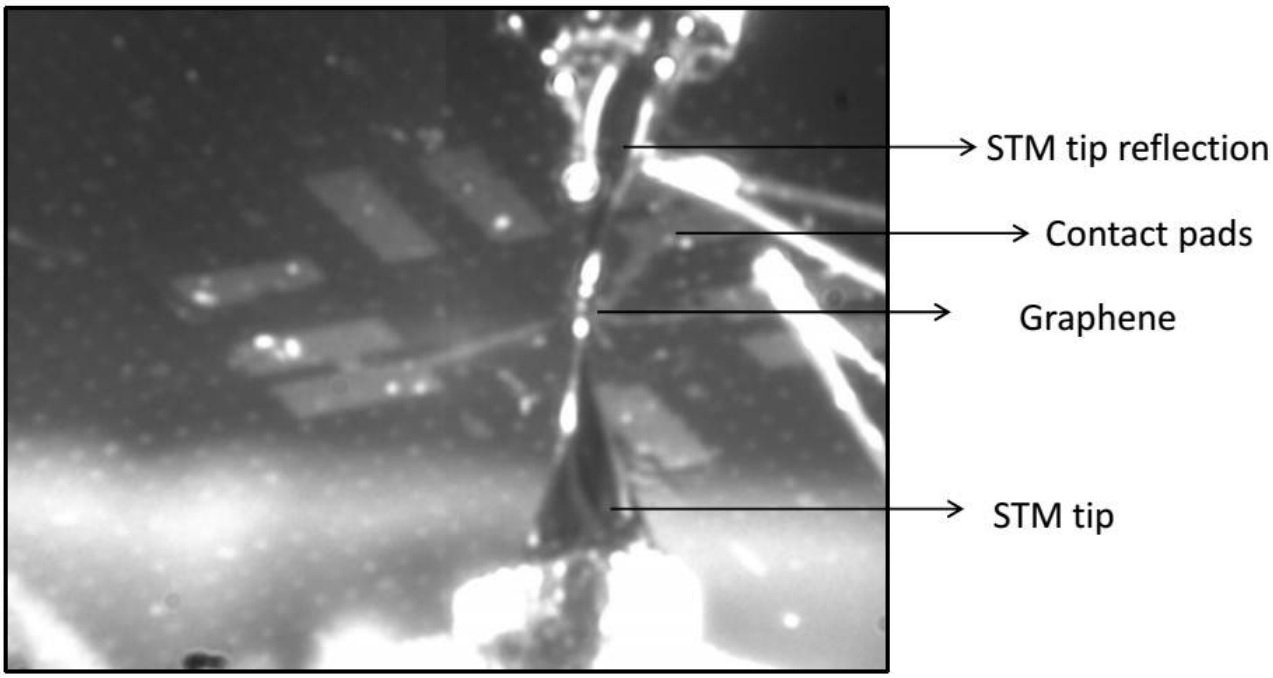

Figure 2.31: : The optical picture of the STM tip a few $\mathring{A}$ away from the grapheme device on SiO_2 substrate.

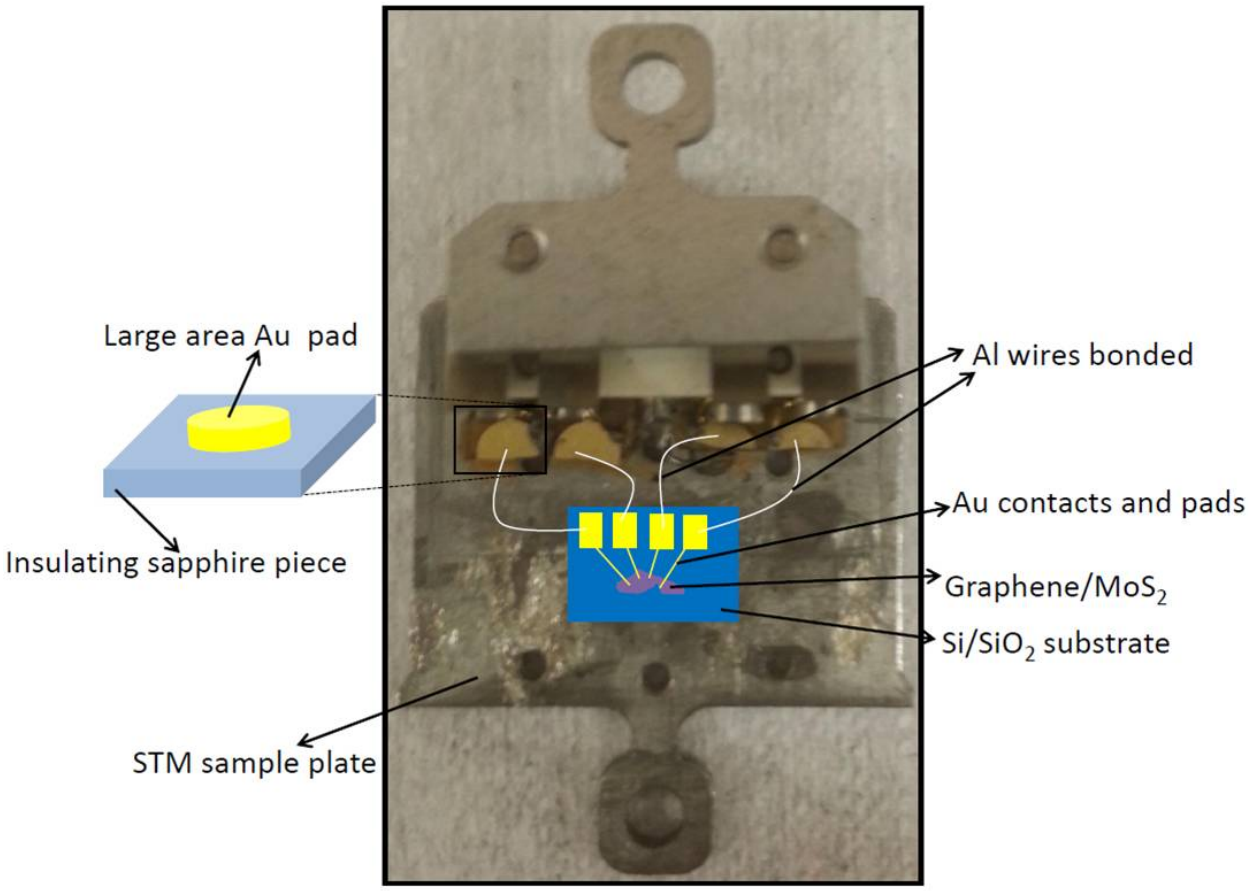

Figure 2.32: : Schematic showing the STM sample plate with modifications for the 4-point contact device measurements.

CHAPTER 3: IMPACT OF CALCIUM ON TRANSPORT PROPERTY OF GRAPHENE

Graphene, a single layer of graphite, possesses unusual electronic properties characterized by relativistic Dirac physics and extraordinary field effect mobility. As such, graphene is highly useful for both fundamental science and applications [28],[43],[67]. Various extrinsic scatterers can sensitively influence the utility of graphene by obscuring the intrinsic property and affecting the performance of graphene-based electronics. As such, understanding the impact of extrinsic scatterers is essential for graphene science and technology. The impact of long-range Coulomb scatterers is most well investigated among various types of scatterers. There are two previous theory results, which define the current understanding on Coulomb scatterers. Gate-dependent conductivity for various areal densities of Coulomb scatterers has been calculated using the Boltzmann kinetic theory with random phase approximation (RPA) [27]. In addition, electron-hole asymmetry in scattering strength, unique to the Dirac physics, has been predicted for charged scatterers [68]. The previous measurements of the transport property as a function of the density of potassium adsorbates [29] showed apparently striking agreement to the theory. Potassium rendered conductivity linearly dependent on the carrier density and induced electron-hole asymmetry. Yet, sufficient discrepancies existed between the theoretical and experimental results. Quantitative differences were seen in the impact of doping by potassium and in the electron-hole asymmetry, while the behavior of the minimum conductivity was completely unexplained by the theory. These discrepancies can signal the failure in the existing theory, or they can be due to properties specific to potassium adsorbates such as density-dependent charge transfer and spatial ordering.

We have measured the impact of calcium adsorbates on the transport property of graphene. Our results parallel the previous results on potassium adsorbates. Quantitative disagreements with the

existing theory are seen for the effect of doping and the electron-hole asymmetry, while the theory fails completely to describe the minimum conductivity. Minor discrepancies make it impossible to confirm or deny the validity of the theoretical calculations although they suggest that the theory at least underestimates static screening by graphene. Failure to explain the minimum conductivity is most likely due to the inability of the Boltzmann theory to describe the transport property when the Fermi wavelength is exceedingly large. Our results indicate that new experimental capabilities to minimize the contribution from the disordered substrate and to measure the number of impurities simultaneously with conductivity measurements are essential for confirming the existing theory on the impact of charged impurities on graphene.

The graphene device was fabricated from mechanically exfoliated graphene on 280 nm thermal silicon oxide on highly doped silicon using electron beam lithography. The graphene sheet was etched into the Hall bar geometry using oxygen plasma after contacts were metallized [69]. The device was annealed in $\mathrm{Ar/H_2}$[32] to remove the resist residues prior to transport measurements performed in an ultra-high vacuum (UHV) chamber, enabling a direct interaction between calcium adsorbates and the graphene sheet. Transport measurements were performed at 20 K in UHV at increasing coverage of calcium, which was evaporated from a homemade evaporator using calcium granules as the source material.

Figure 3.1(a) shows a representative gate dependent conductivity of the graphene device at 20 K with definitions of the parameters discussed in this paper. The minimum voltage, $\mathrm{V_{min}}$, is defined as the gate voltage at which the minimum conductivity, σ_{min}, is observed. We call this location the minimum point. Red dotted lines describe the gate dependence of conductivity away from $\mathrm{V_{min}}$. These lines intersect above zero conductivity at the residual conductivity, σ_{res}. The plateau width is the gate voltage range where conductivity deviates from the linear behavior and the width is determined by intersecting a line through the minimum conductivity and the dotted lines.

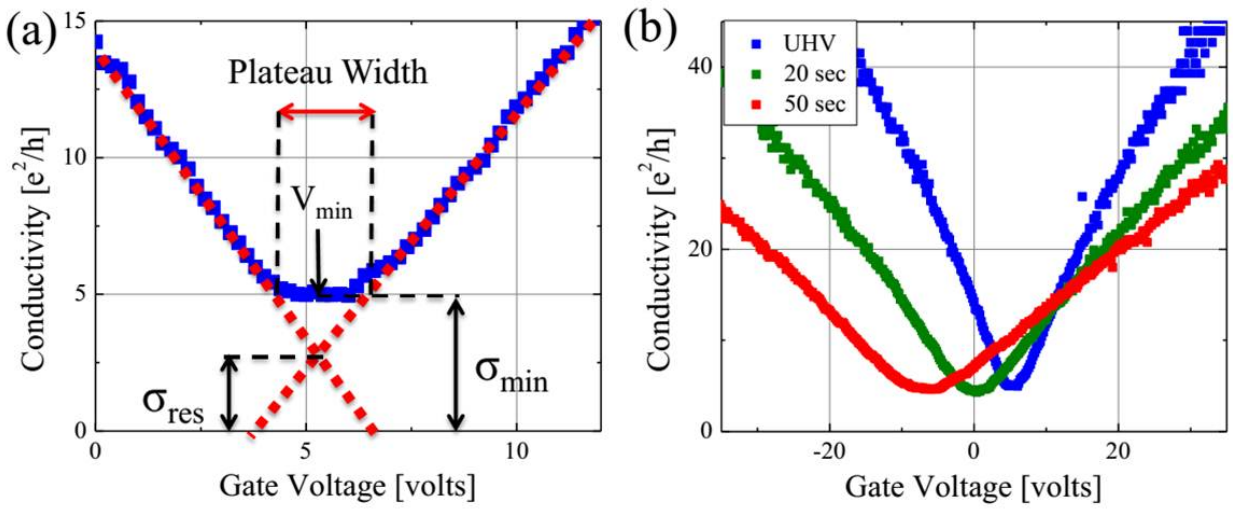

Figure 3.1: (a) Gate dependent conductivity of the graphene device used for the experiment.The figure shows the definition for the plateau width ($\mathrm{V_{min}}$), minimum conductivity (σ_{min}) and residual conductivity (σ_{res}). Dotted red lines are used to determine the plateau width and residual resistivity. (b) Gate dependent conductivity of the graphene device at increasing levels of calcium adsorbates.

Gate-dependent conductivity, $\sigma(\mathrm{V_g})$, is well-described as $(1/\mathrm{ne}\mu + 1/\sigma_{\mathrm{c}})^{-1}$ in the limit of high n, where n is the number of carriers, e is the charge of an electron, μ is field effect mobility and σ_{c} is a constant conductivity as observed previously [29],[70],[71]. The first term has been attributed to the scattering induced by the long-range Coulomb impurities with mobility inversely proportional to the number of impurities. σ_{c} has been suspected to be due to short-range impurities or white noise impurities [70]. Field-effect mobility is assumed to be gate independent in this paper and determined by fitting a linear line to the dependence of n/$\sigma(\mathrm{V_g})$ and finding its intercept at n = 0. Figure 3.1(b) shows measured conductivity at increasing coverage of calcium. The impact of calcium on graphene is qualitatively similar to that of potassium. Upon increasing the coverage, we observe that $\mathrm{V_{min}}$ shifts to more negative values, mobility is significantly reduced, conductivity is rendered linearly dependent on gate voltage, minimum conductivity varies non-monotonically, and plateau width is increased. In the following discussion, each feature will be quantitatively compared to the theoretical calculations.

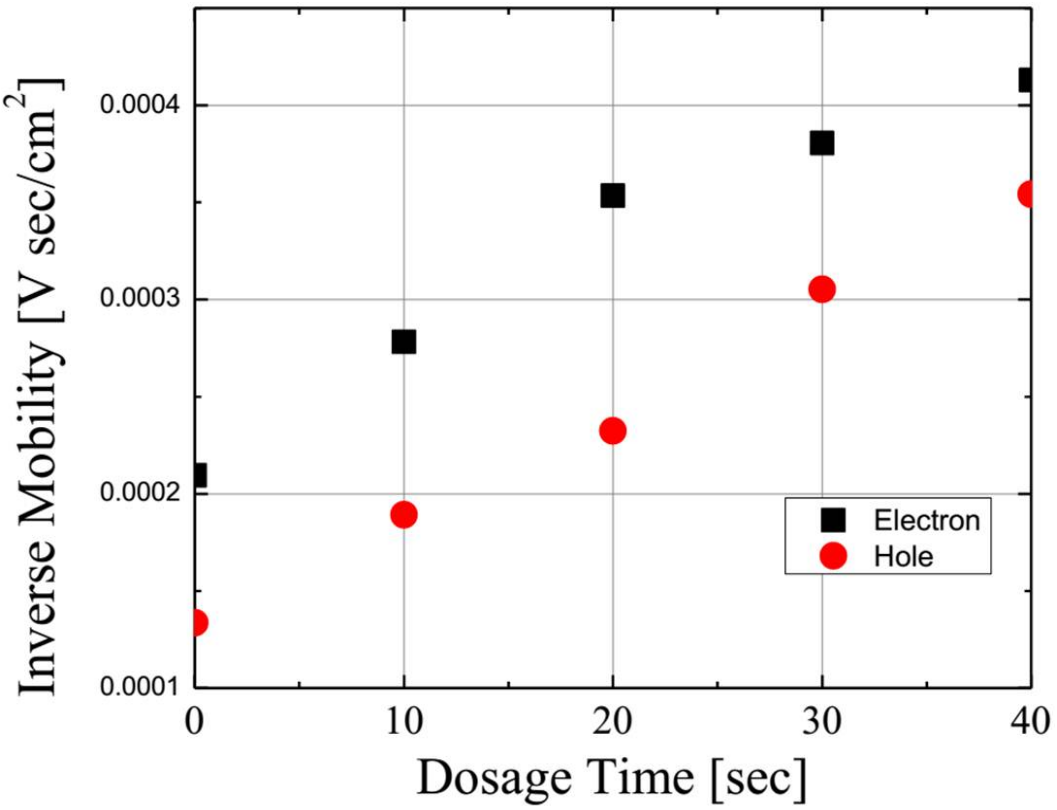

Figure 3.2: Inverse electron and hole mobility as a function of the calcium dosage time.

The dependence of electron and hole mobility on the observed shift of $\mathrm{V_{min}}$, $\mathrm{V_{Shift}}$, is as shown in Figure 3.2. Constant evaporation rate was achieved by maintaining the same power on the calcium evaporator. In this case, the accumulated exposure time is proportional to the number of adsorbates assuming a constant sticking coefficient. The figure shows that there is a linear relationship between the number of adsorbates on the surface and inverse mobility as observed previously [29] and in consistency with the Boltzmann-RPA calculation [27]. Figure 3.3(a) shows the dependence of V shift on inverse electron and hole mobility. The observed behavior is well described by a power law. The exponents are found to be 1.51 for holes and 1.37 for electrons. The Boltzmann-RPA theory calculation finds the exponents to be 1.2-1.3 [27] and finds the power law behavior to be the hallmark of nontrivial, weak screening by graphene. Yet, this agreement of the experimental and theoretical exponents is only partially relevant.

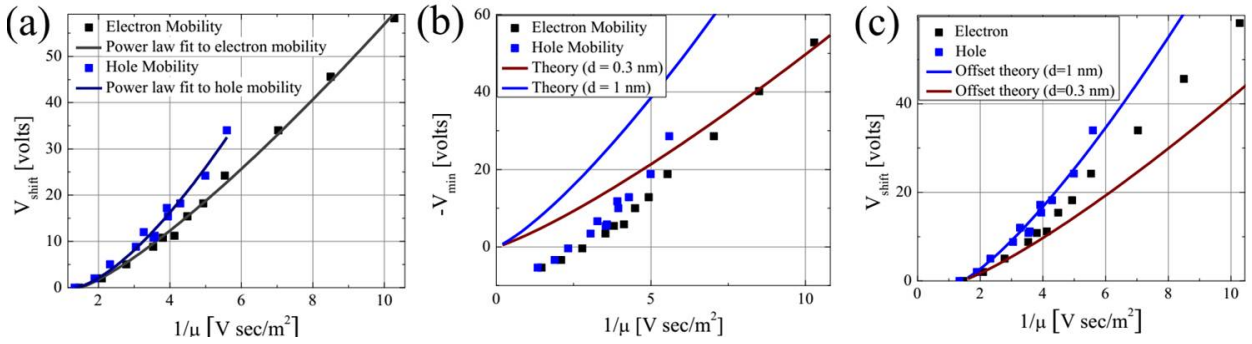

Figure 3.3: $\mathrm{V_{shift}}$ as a function of inverse electron and hole mobility. A power law behavior is observed for both electron and hole mobility. (b) $\mathrm{V_{min}}$ as a function of inverse electron and hole mobility. Solid lines are calculated values for charged impurities located 0.3 nm and 1 nm away from graphene. (c) Theoretical curves have been offset in the x-axis by 1.4 $\mathrm{Vsec/m^2}$.

The theory considered only one type of charged impurities and $\mathrm{V_{min}}$ was assumed to be equal to $\mathrm{V_{Shift}}$. A direct comparison of the theoretical curve to our results shows an offset as shown in Figure 3.3(b), which is likely due to the extra charge transfer from the substrate-bound charged impurities, not considered by the theory. Shifting the theoretical curves, we find that the results are close to the theoretical curve generated using an unrealistic adsorbate-graphene distance of 1 nm as shown in Figure 3.3(c). The distance is approximately 3 $\mathring{A}$ for both potassium and calcium as measured and calculated previously [72],[73]. Such underestimation of $\mathrm{V_{Shift}}$ at a given scatterer concentration indicates that graphene screens calcium more effectively than expected from the Boltzmann-RPA theory calculation. Increased screening is most likely due to extra carrier density induced by the substrate-bound impurities and removal of the substrate impurities should allow more complete testing of the theory.

Electron-hole asymmetry in mobility is expected to depend on the static dielectric constants of graphene and the substrate as well as the charge transferred per adsorbate [68]. $\mu_\mathrm{e}/\mu_\mathrm{h}$ remains to be approximately 0.9 from before dosing to increasing coverage of calcium adsorbates as shown in Figure 3.4(a), indicating that both the substrate-bound Coulomb impurities and calcium adsorbates induce the same asymmetry.

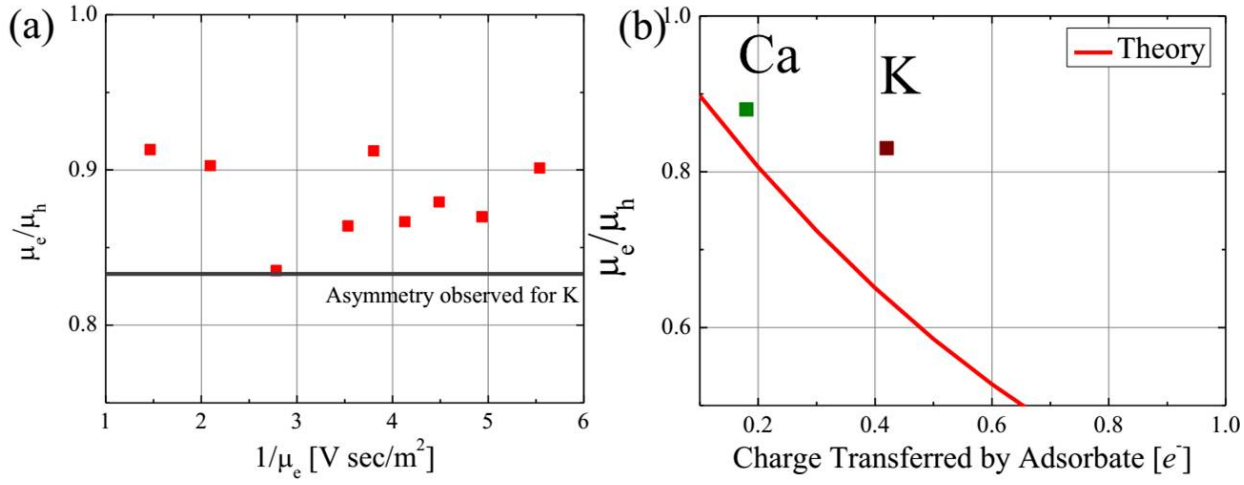

Figure 3.4: (a) μ_e/μ_h at increasing coverage. (b) Theoretical μ_e/μ_h at different Z for adsorbates. Green and brown dots indicate the experimental values for calcium and potassium. Values of charge transfer for potassium and calcium are as calculated previously [73].

Figure 3.4(b) shows the comparison of the observed asymmetry to the theoretical expectation for μ_e/μ_h. The theoretical ratio is generated using $\kappa_{\text{substrate}} = 2.45$ and $\kappa_{\text{grapheneRPA}} = 2.41$, which are dielectric constants due to the substrate and the graphene lattice on SiO_2 substrates [74]. As shown, decreased asymmetry for calcium compared to potassium is as expected by the theory as calcium has been calculated to transfer less charge than potassium [73]. The observed smaller ratios for both calcium and potassium can be due to underestimation of either charge transfer from adsorbates or screening by graphene. Direct simultaneous determination of both the adsorbate density and transport property should enable the elucidation of the nature of the observed asymmetry.

The impact of calcium adsorbates on σ_{min} is poorly described by the previous theoretical calculations. σ_{min} fluctuates little near $4.5e^2/h$ at increasing coverage as shown in Figure 3.5(a), while the Boltzmann-RPA theory calculation predicts a monotonic, decreasing behavior with respect to the coverage. This nearly constant behavior seen for calcium and non-monotonic behavior seen for potassium [29] indicate the failure of the theory to describe the transport property of graphene at the minimum point.

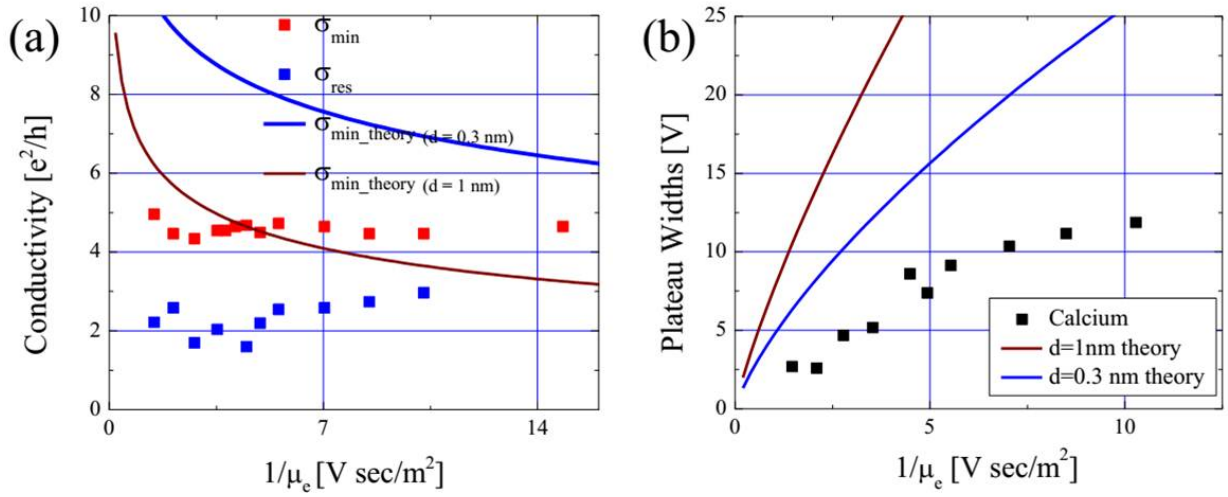

Figure 3.5: Comparison of observed data and theory of (a) minimum and residual conductivity and (b) plateau widths.

In addition, the observation of near constant $\sigma_{\rm res}$ near $2.5{\rm e}^2/{\rm h}$, which is similar to the previous results on potassium adsorbates, is also in complete disagreement with the theory. The Boltzmann approximation is expected to be inaccurate when the Fermi wavelength approaches infinity at the Dirac point. Yet, the Boltzmann-RPA theory has been expected to be accurate at the minimum point because the inhomogeneity introduced by the substrate-bound impurities ensures the Fermi wavelength to be finite except at the few points where the Fermi level crosses the Dirac point. The observed $\sigma_{\rm min}$ and $\sigma_{\rm res}$ demonstrate that these crossing points are sufficient to make the Boltzmann-RPA theory inadequate in describing the minimum point.

Unlike $\sigma_{\rm min}$ and $\sigma_{\rm res}$, the plateau widths show qualitative agreement to the Boltzmann-RPA theory. The heoretical result remains closer to our experimental results away from the minimum point. The observed widths are smaller than the theoretical values in contradiction with the Boltzmann-RPA theory as the charged scatterers bound on the substrates should be contributing to widen the plateau. Such discrepancy can be due to the experimental inaccuracy in determining the plateau. Minimizing the contribution from the substrate impurities should enable better experiments.

In conclusion, we have measured the impact of calcium adsorbates on the transport property of graphene to determine if the discrepancies seen in the previous measurements using potassium adsorbates are systematic to all charged impurities or specific to the interaction between potassium and graphene. We find that similar behavior is manifested by graphene under the influence of calcium. Our results indicate that the Boltzmann-RPA theory has not been properly confirmed by experiment and is inadequate at the minimum point. Further tests on the previous theoretical calculations must minimize the influence of the substrate as have been achieved by hexagonal boron nitride [75] and count the density of charged scatterers while measuring their impact on the transport property.

CHAPTER 4: UNCOVERING THE DOMINANT SCATTERER IN GRAPHENE ON SILICON OXIDE.

4.1. Impact of atomic hydrogen adsorbates on graphene on SiO_2.

Freely suspended graphene sheets display high-field-effect mobility, reaching 2×10^5 cm^2/Vs [76], [77]. High mobilities allows for a wider utilization of graphene sheets in testing relativistic quantum mechanics, exploring two dimensional physics, and creating new electronic, optoelectronic, and spintronic device technologies [4],[43], [67]. Yet, suspended graphene sheets are fragile and impractical for most experiments and applications. Substrate-bound graphene sheets are easier to handle but possess low-carrier mobilities, which can even vary by an order of magnitude from sample to sample. Poor and unpredictable transport properties reduce the utility of substrate-bound graphene sheets for both fundamental and applied sciences. Therefore, understanding the impact of substrates is crucial for graphene science and technology.

Charged impurities, [27], [30] ripples,[33] and resonant scatterers [37],[36],[38], [39] have been considered for modeling the transport property of graphene field-effect transistors (FETs). Previous experimental studies have explored the impact of charged impurities [29] and resonant scatterers [40],[78],[79],[80] by using adsorbed impurities or creating vacancies on graphene sheets. Yet, these studies revealed only the impact of adsorbates or vacancies and did not shed information on the nature of the native scatterers already present in the samples. Furthermore, experiments using different dielectric environments have provided contradictory results on the role and importance of charged impurities[31],[71]. Thus, there are no conclusive experimental results revealing the nature of the native scatterers that limit the transport properties of graphene on SiO_2.

We have measured the impact of low-energy atomic hydrogen on the transport properties of graphene as a function of coverage and the initial field-effect mobility. Our transport measurements and Raman spectroscopy measurements show that hydrogen exerts a short-range scattering potential which introduces intervalley scattering. Hydrogen transfers a small but finite amount of charge, as indicated by the gate-dependent transport measurements. The resistivity added by hydrogen remains proportional to the number of adsorbed hydrogen and, therefore, adheres to Matthiessen's rule even at the highest coverage. This shows that adsorbed hydrogen remains rather dilute and does not interfere with other pre-existing scattering mechanisms. The added resistivity at high-carrier densities varies approximately as n^{δ} , where n is the carrier density and $\delta \approx$ -1.5. Importantly, the saturation coverage of atomic hydrogen is found to be proportional to the inverse initial mobility and, therefore, to the number of pre-existing scattering sites. Finally, our results show that the reactivity to atomic hydrogen is a characteristic manifestation of the most dominant scatterer in graphene sheets on $\mathrm{SiO_2}$.

The graphene FETs in our measurements are prepared using the conventional method [81]. Transport properties are measured using the four-probe method citedevicedim. The initial, prehydrogenation mobility ranged from 1900 to 8300 cm^2/Vs for different graphene devices. Each device is hydrogenated at constant temperature between 11- 20 K [82]. We use a commercial atomic hydrogen cracker, EFM H from Omicron GmBH, which utilizes a tungsten capillary heated to 2500 K by an electron beam. The cracker also generates high-energy ions which are steered away from graphene using an electric deflector. The dosage rate of atomic hydrogen [83] is maintained constant throughout the measurements using a variable leak valve. The total dosage or accumulated areal dose density can be very different from the actual hydrogen coverage depending on the sticking coefficient. Transport properties are measured at increasing dosages.

Figure 4.1 shows the impact of atomic hydrogen adsorption on the conductivity of graphene sheets.

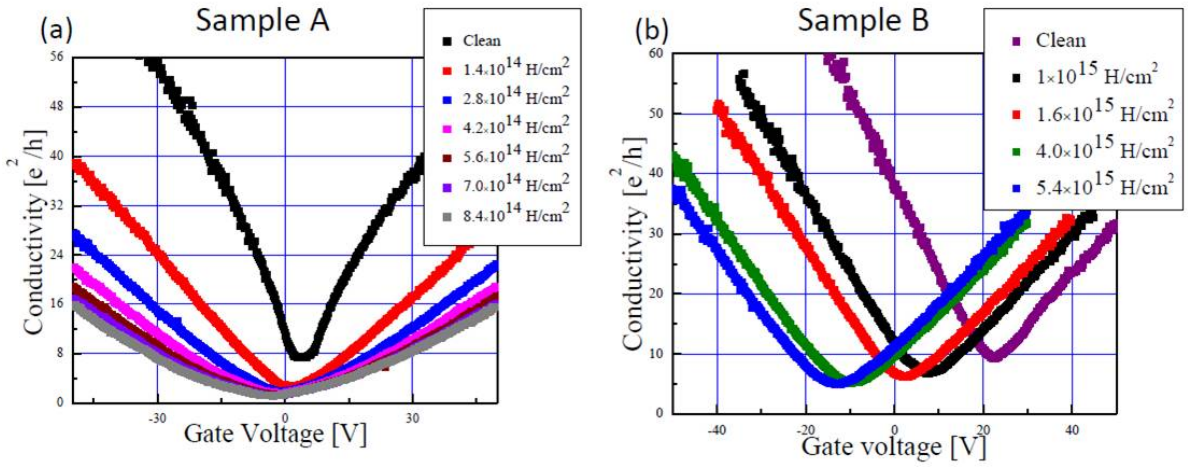

Figure 4.1: (a), (b) Impact of atomic hydrogen on the transport properties of graphene sheets (samples A and B) for increasing areal dosage density. Sample A was measured at 12 K and B at 20K, respectively. The areal densities, the number of impinging hydrogen (which may not be necessarily adsorbed on graphene), are (a) purple: clean (zero), black: 1×10^{15}/cm^2, red: 1.6×10^{15}/cm^2,green: 4×10^{15}/cm^2, blue: 5.4×10^{15}/cm^2, and (b) black: clean (zero), red: 1.4×10^{14}/cm^2, blue: 2.8×10^{14}/cm^2, brown: 5.6×10^{14}/cm^2, and silver: 8.5×10^{14}/cm^2.

The changes induced by hydrogen adsorption saturate above a certain dosage. These changes are: (i) a shift in the gate voltage at which the conductivity is minimal (V_{min}), (ii) an increase in the intensity of the D peak in the Raman spectra, (iii) a monotonic decrease in the conductivity minimum, and (iv)an additional gate-dependent resistivity which varies as $\mid V_g - V_{min} \mid^{\delta}$, where $\delta \approx$-1.5 at large $\mid V_g - V_{min} \mid$. The gate dependence of the conductivity becomes superlinear at high-dosage levels as a result of this exponent. Below, we discuss each change in more detail.

A finite charge is donated to graphene by the adsorbed hydrogen, as indicated by the shift of V_{min} upon hydrogenation. The observed sign of the charge transfer from atomic hydrogen to carbon is consistent with a previous experiment [84] and theoretical calculations [85],[86] [25,26] but different from hydrogenation studies using atomic hydrogen derived from a hydrogen plasma.[79],[80] It is not possible to determine the amount of charge transferred per adsorbed hydrogen directly from our experiment, as the sticking coefficient of hydrogen on graphene is unknown.

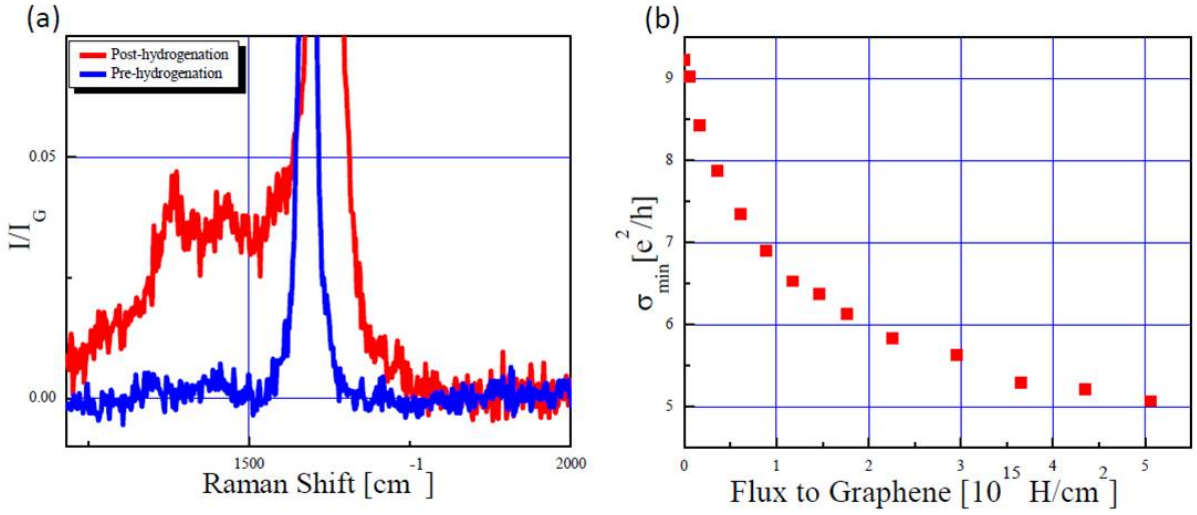

Figure 4.2: (a) Raman spectra acquired for sample A before and after hydrogenation. The observed intensity has been normalized to the peak height of the G-band. (b) Minimum conductivity as a function of increasing dosage in sample A.

Previous experiments [79],[80],[84] do not agree on the amount of charge transfer from hydrogen. Theoretical studies show 0.076 to 0.161e (Ref.26) or 0.16 to 0.25e (Ref.25) donated per hydrogen (e denotes the electron charge), depending on the degree of allowed lattice relaxation [86] or the position of hydrogen.[85] Below, these calculated values are used to estimate the saturation coverage of hydrogen.

Raman spectroscopy and the impact of atomic hydrogen on the minimum conductivity reveal that atomic hydrogen introduces intervalley scattering and, therefore, exerts a short-range scattering potential. [87] [27] Figure 4.2(a) shows Raman spectra acquired at room temperature in air both before hydrogen dosing and after achieving saturation at low temperature. The intensity of the D peak in the Raman spectrum is larger upon adsorbing hydrogen. The relative intensity of the D peak to the G peak, I_D/I_G, which can be used to estimate the adsorbed hydrogen density,[88],[89],[90] is 0.0034 $\pm$ 0.0021 and 0.0182 $\pm$ 0.0056 before and after hydrogen adsorption, respectively.[31] The small values observed for this D-G ratio even at saturation are likely due to the small desorp-

tion barrier for hydrogen, as discussed below. Figure 4.2(b) shows that the minimum conductivity decreases monotonically as a function of hydrogen dosage. The minimum conductivity at saturation ranges from 0.52 to $5.1\mathrm{e}^2/\mathrm{h}$ for different devices. Since long-range scatterers have been found to vary the minimum conductivity non-monotonically and not below $4\mathrm{e}^2/\mathrm{h}$, [27],[29] our transport measurements are also consistent with hydrogen exerting a short-range scattering potential.

Figure 4.3(a) shows the added resistivity due to atomic hydrogen at different dosage levels as a function of $\mathrm{V_g} - \mathrm{V_{min}}$. The impact of atomic hydrogen is nearly electron-hole symmetric and the added resistivity varies approximately as $\mid \mathrm{V_g} - \mathrm{V_{min}} \mid^{-1.5}$ at large $\mid \mathrm{V_g} - \mathrm{V_{min}} \mid$ for all samples, as shown in Figure 4.3(b). The resistivity exponent differs from the -1 value expected for Coulomb impurities and the electron-hole symmetry is consistent with a resonant scatterer positioned very close to the Fermi level (i.e., a midgap resonant state). [91] The observed exponent also agrees with calculated exponents for resonant scatterers with a finite on-site amplitude [92] as well as for Gaussian-correlated scatterers. [22], [93] As shown in Figure 4.3(c), we find that the curves of added resistivity versus gate voltage for successive dosage levels collapse on top of each other when divided by the induced shift in $\mathrm{V_{min}}$, $\mathrm{V_{shift}}$, indicating that the added resistivity at different dosage levels is proportional to $\mathrm{V_{shift}}$. Therefore, the number of adsorbed hydrogen atoms is directly proportional to $\mathrm{V_{shift}}$. For long-range scatterers such as potassium adsorbates, [29] $\mathrm{V_{shift}}$ does not vary linearly with the number of adsorbates. Such nonlinearity has been attributed to incomplete screening of the potential imposed by potassium on graphene.[27][6] Therefore, we conclude that the excess charge of adsorbed atomic hydrogen is effectively screened by graphene. All samples we have measured show a similar behavior (for instance, see Figure 4.3(d) for sample B). Deviations from the observed normalization by $\mathrm{V_{shift}}$ are found only at low-dosages and can be attributed to uncertainty in determining $\mathrm{V_{min}}$ at low-dosage. The observed normalization also shows that the scattering cross-section of hydrogen does not vary appreciably even at higher dosage levels and that hydrogen does not modify other scattering mechanisms.

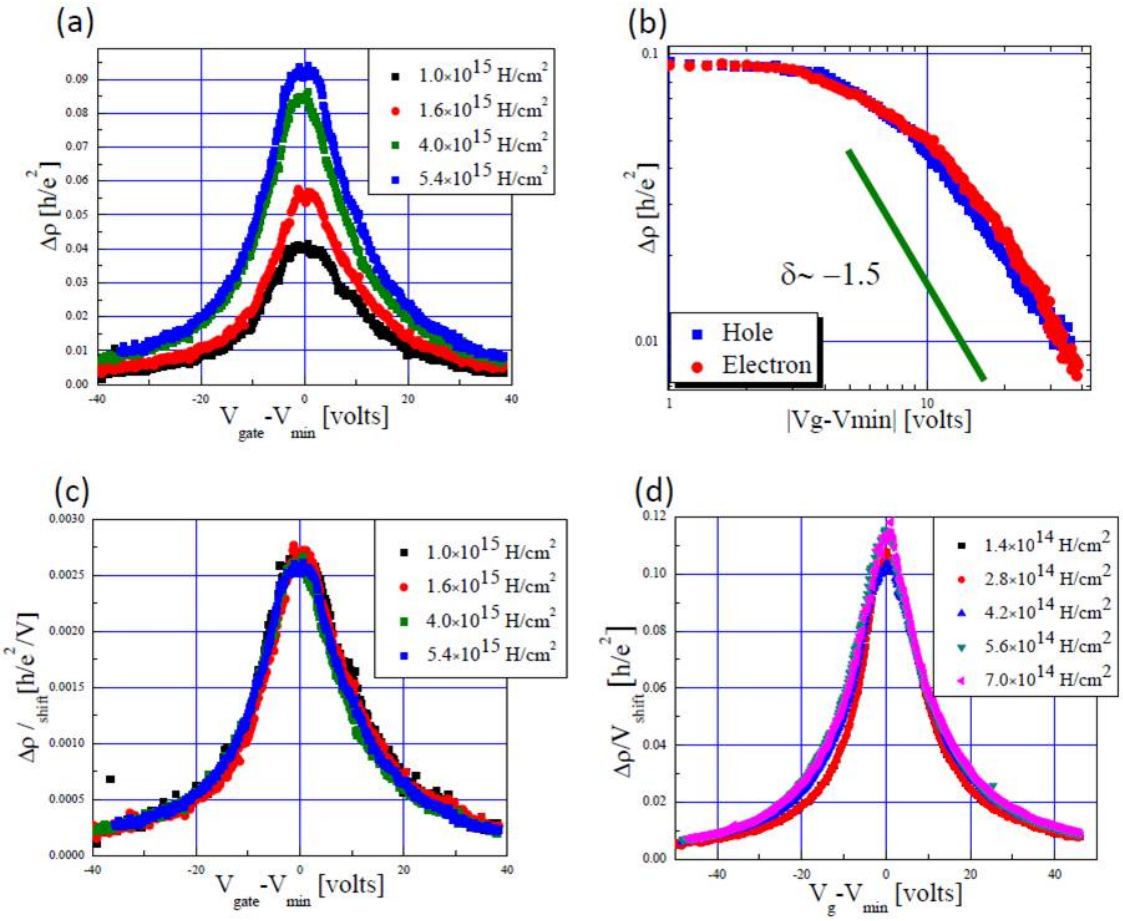

Figure 4.3: (a) Resistivity added by hydrogen as a function of $V_g - V_{min}$ at different areal dosage density. (b) Gate dependence of the added resistivity as a function of $V_g - V_{min}$ at the areal dosage density of 5.4× 10^{15} H/cm^2. The green line indicates the slope for an exponent of -1.5. (c) Added resistivity as a function of $V_g - V_{min}$ at different areal dosage normalized to $V_g - V_{min}$. [(a)-(c) for sample A] & (d) Same as in (c) but for sample B.

Therefore, the added resistivity by hydrogen follows Matthiessen's rule, $R_{total} = R_{adsorbates} + R_{substrate} + R_{graphene}$, where $R_{adsorbates}$ and $R_{substrate}$ are due to scattering by adsorbates and the substrate, respectively, and $R_{graphene}$ is the intrinsic resistance of the graphene sheet.

Figure 4.4 (a) shows V_{shift} , which is proportional to the number of adsorbed hydrogen, as a function of the accumulated hydrogen dosage. The behavior is well described by a saturating exponential function, with a saturation voltage denoted V_{sat}.

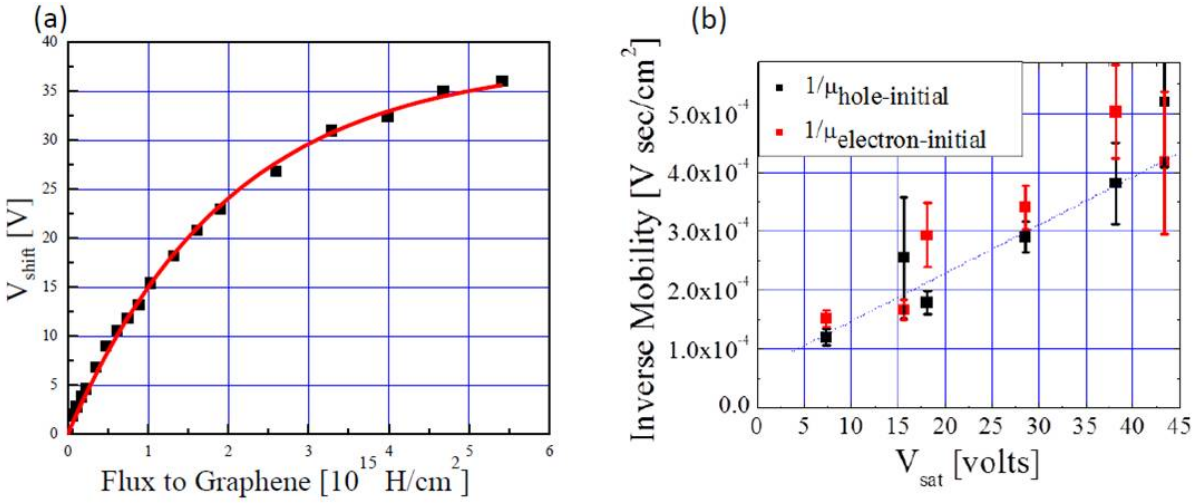

Figure 4.4: (a) V_{shift} as a function of the increasing areal dosage density for sample A. (b) Initial maximum electron and hole mobility as a function of the saturation voltage shift, V_{sat}, for different samples.

A wide range of V_{sat} is observed for different samples, from 7.34 to 43.4 V. The maximum shift of 43.4 V implies that the observed maximum coverage of hydrogen is 0.012 assuming the predicted charge transfer [86] of 0.076e per adsorbed hydrogen. We find no correlation between experimental temperatures and saturation voltages. Figure 4.4(b) shows that the saturation coverage for different samples is inversely proportional to their initial maximum electron and hole field-effect mobility. [94] Since the inverse mobility is proportional to the number of scatterers, our data show that the number of native scatterers is proportional to the number of possible adsorption sites for hydrogen. By extrapolation to the limit where these sites are absent, we obtain a mobility of $(1.5 \pm 0.3) \times 10^4 \mathrm{cm}^2$ /V s, as determined by a linear fit. This extrapolated mobility value is still an order-of-magnitude lower than the field-effect mobility measured for suspended graphene sheets, [76],[77] showing that there are still other, less important, scatterers reducing the mobility of graphene on SiO_2. Interestingly, the extrapolated value is similar to the maximum mobility observed on SiO_2 in previous studies [95],[9] suggesting that the reactivity to hydrogen is the signature of the most dominant type of native scatterers for all graphene devices on SiO_2.

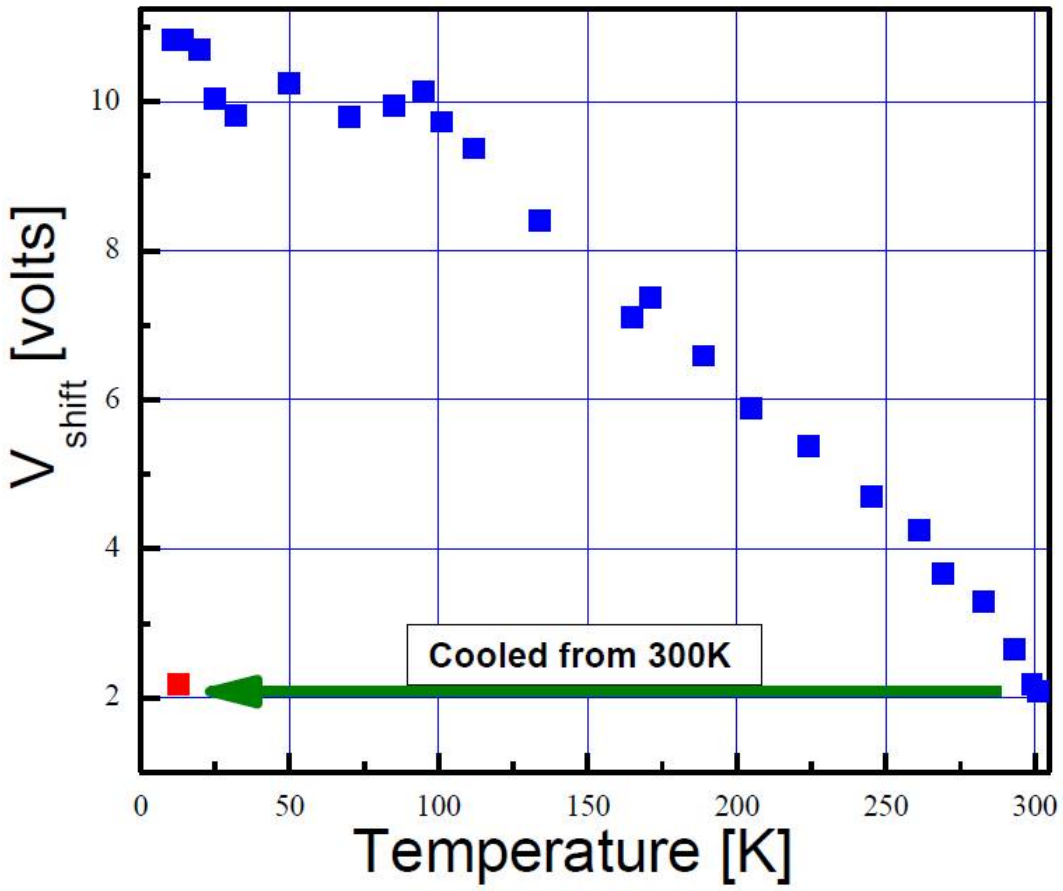

Figure 4.5: V_{shift} at increasing temperature for sample C after reaching saturation coverage by atomic hydrogen at 11 K. Data acquired at a warming rate of 0.45 to 6 K/min. Red point indicates V_{shift} when the warmed hydrogenated device is cooled down again from 300 K.

V_{shift} induced by the adsorbed hydrogen is reduced as the temperature is raised, as shown in Figure 4.5. The value of V_{shift}remains constant when warmed samples are again cooled, indicating that the observed reduction in V_{shift} is due to the desorption of hydrogen. This temperature dependence indicates that the desorption energy of adsorbed hydrogen on graphene is much smaller than the previously reported values of approximately 1eV on graphite. [96] A small desorption energy explains the small D peak observed in the Raman spectra of the hydrogen-dosed samples acquired at room temperature and suggests that atomic hydrogen is not forming a fully relaxed covalent bond to carbon. Furthermore, we also know that the maximum thermal energy of impinging atomic hy-

drogen barely exceeds the barrier of 0.21 eV calculated for the attachment of atomic hydrogen to planer graphite. [97]Therefore, atomic hydrogen is binding only to unusual, chemically-activated sites, which do not relax to a full sp^3 configuration upon adsorbing hydrogen.

It is possible that the reactivity of graphene sheets is enhanced by adding curvature or changing the Fermi level. Wrinkles [98],[99] and ripples [33] can perturb the sp^2 bonds, generating chemically-activated sites for hydrogen. Charge puddles [27] may also increase the reactivity of graphene sheets. However, the data presented in this section cannot determine the sites with affinity to atomic hydrogen in graphene on SiO_2.

In conclusion, we used atomic hydrogen to probe the nature of native scatterers in graphene. Hydrogen exerts short-range scattering potential in graphene, as indicated by Raman spectroscopy and the impact on the minimum conductivity. Charge is transferred from hydrogen to carbon and the Coulomb potential created by the induced charge on hydrogen is effectively screened by carriers in graphene. The adherence of the added resistivity to Matthiessen's rule also shows that: (i) adsorbates do not influence the resistivity caused by other factors (such as lattice defects, phonons, etc.) and (ii) the number of adsorbed hydrogen, n_H, is proportional to $\mathrm{V}_{\mathrm{shift}}$. Finally, the number of hydrogen adsorption sites is found to correspond to the number of native scatterers; in the absence of these scatterers, the carrier mobility of graphene sheets will reach $1.5 \times 10^4 \mathrm{cm}^2$ /V s. The scatterers uncovered in this study dominate the transport properties of graphene-based FETs on SiO_2 and the affinity to atomic hydrogen is the hallmark of these scatterers. Our results provide an important insight into the nature of the scatterers which limit mobility of graphene sheets on substrates.

4.2. Counting the dominant scatterer in graphene on SiO_2

In the last section 4.1 we discovered that atomic hydrogen counts the number of native scatterers in graphene on SiO_2, in terms of V_{sat}. To quantitatively find the number of native scatterers one needs to calculate the charge transferred from the adsorbed hydrogen to graphene. This can be accomplished by doing temperature desorption study of hydrogenated graphene samples as I will describe in his chapter. We correlate the number of scatterers to field effect mobility of graphene devices on SiO_2, which is the most commonly used substrate for graphene science and technology, and find that the scattering strength of the dominant scatterer responsible for the observed variability is consistent with charged impurities.

Charged [27] and resonant impurities [100],[36],[38], [39],[92] are both suspected to be the origin for the variability. These impurities exert radically different scattering potentials: charged impurities exert Coulomb scattering potential and resonant impurities apply atomic scale scattering potential. Scattering strengths of these impurities are known: charged impurities near graphene are observed to affect the mobility as $1/\mu_{\mathrm{FE}} = (2 \times 10^{-16})\mathrm{n_{charged}}\mathrm{Vsec/cm^2}$ [29] and resonant impurities as $1/\mu_{\mathrm{FE}}$= $1 \times 10^{-15}\mathrm{n_{resonant}}\mathrm{Vsec/cm^2}$ [40]. The scattering strength of the dominant scatterer has never been measured, rendering quantitative determination of the origin of the variability impossible. Qualitative evidences have not been conclusive. The typical density of charged impurities of $50 \times 10^{10}/\mathrm{cm^2}$ on SiO_2 is consistent with the maximum observed mobility on the substrate using the above formula. Yet, the typical density does not explain the variability. Furthermore despite isolation of graphene from SiO_2 substrates by inserting hexagonal boron nitride [101] and suspending graphene [77] drastically increases the maximum mobility, large variability remains even in such devices. Finally, gate-dependent resistivity of graphene can be fitted to theoretical expectations [27],[38],[39],[102],[103] by choosing correct impurity density, potential, and locations, but such analysis remains speculative because these adjustable parameters cannot

be independently confirmed.

Graphene field effect transistors (FETs) are fabricated from mechanically exfoliated graphene on SiO_2 using conventional e-beam lithography [104]. Devices are cleaned down to atomic scale in Ar/H_2 at 350 $^\circ$C for 3 hours [32] and annealed in ultra-high vacuum at above 400 K for approximately 12 hours to remove any impurities adsorbed from air before each experiment. Devices are exposed to atomic hydrogen generated using hydrogen cracker (as described in last section) at temperatures ranging from 8 to 15 K. Hydrogen is introduced by means of a leak valve and a constant hydrogen flux of approximately 3.7 $\times 10^{12}\mathrm{H}/\mathrm{cm}^2$/sec is maintained. After the effect due to hydrogen is saturated, desorption is measured as a function of temperature. After each measurement, devices are dehydrogenated at above 400 K for longer than 12 hours to recover hydrogen-free graphene.

Figure 4.6(a) shows an example of the impact of atomic hydrogen on the transport properties of graphene with the initial mobility of 13400 cm^2/V sec. As discussed in last section 4.1, upon dosing with atomic hydrogen, the gate voltage $\mathrm{V_{shift}}$ at which the conductivity is minimized ($\mathrm{V_{min}}$) shifts to more negative values. The amount of voltage shift to V_{min} induced by hydrogen, v, is proportional to the number of atomic hydrogen adsorbed on the surface. Furthermore, adsorbed hydrogen atoms behave as isolated scattering sites and, therefore, are not clustered. The effect of atomic hydrogen is observed to saturate and $\mathrm{V_{saturation}}$, $\mathrm{V_{shift}}$ at the saturation limit, was found to be proportional to the initial inverse carrier mobility indicating that the dominant scatterer has enhanced affinity towards hydrogen. Finally, atomic hydrogen is weakly bound to graphene and is readily desorbed as shown in Figure 4.6(b). $\mathrm{V_{shift}}$ decreases and eventually approaches zero as devices are annealed at 400 K.

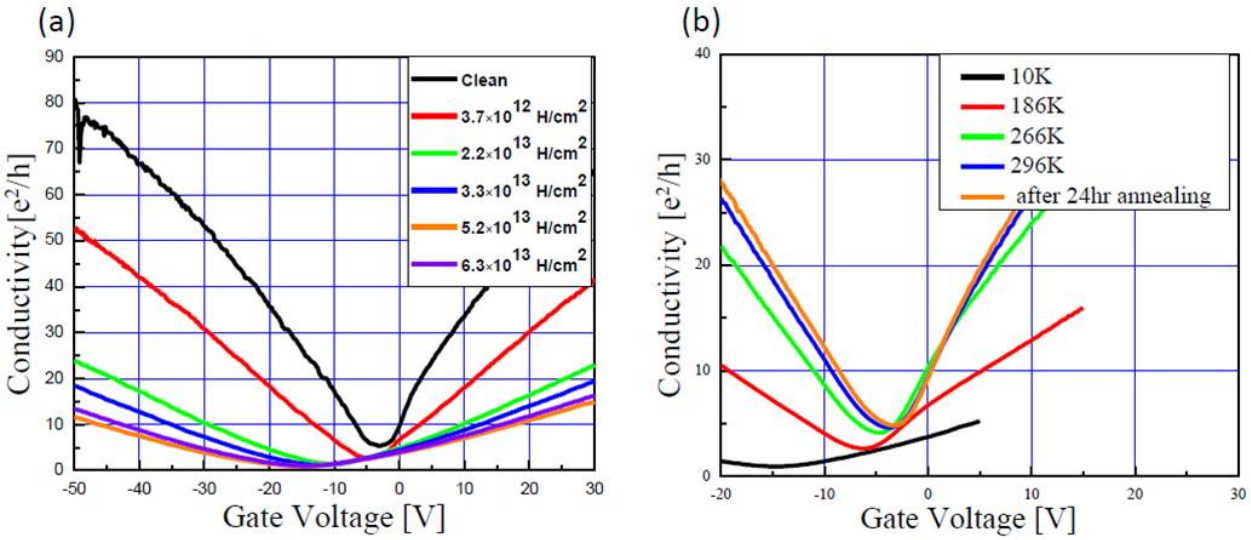

Figure 4.6: (a) Conductivity as a function of gate voltage for a representative device. Black curve shows the transport in undoped clean graphene sample. (b) The temperature dependent measurements of hydrogenated graphene. As the temperature is increased from 10 K to 400 K the dehydrogenation of graphene is evident from the decrease in V_{shift}.

In this paper, we determine charge transfer from atomic hydrogen to the scattering sites to correlate the mobility to the number of the dominant scatterer to find the scattering strength of the scatterer and identify the cause for the variability.

The interaction strength between hydrogen and graphene is expected to be proportional to charge transfer per hydrogen and can be measured by observing desorption characteristics. Figure 4.7(a) shows the temperature dependence of V_{shift} as the representative graphene device shown in Figure 4.6(a) is warmed from 15 to 300 K. Hydrogen desorbs from graphene nearly continuously in this temperature range, indicating a large range of desorption energies from 40 to 1000 meV assuming 1st order desorption. The observation of a range of desorption energies is unexpected since atomic hydrogen physisorbs with desorption energy of 31.6 meV [105] or chemisorbs with 1.4 and 1.8 eV [106], [107] on graphite. Figure 4.7(b) shows desorption characteristics of hydrogen from another device with the initial mobility of 6000 cm^2/V sec.

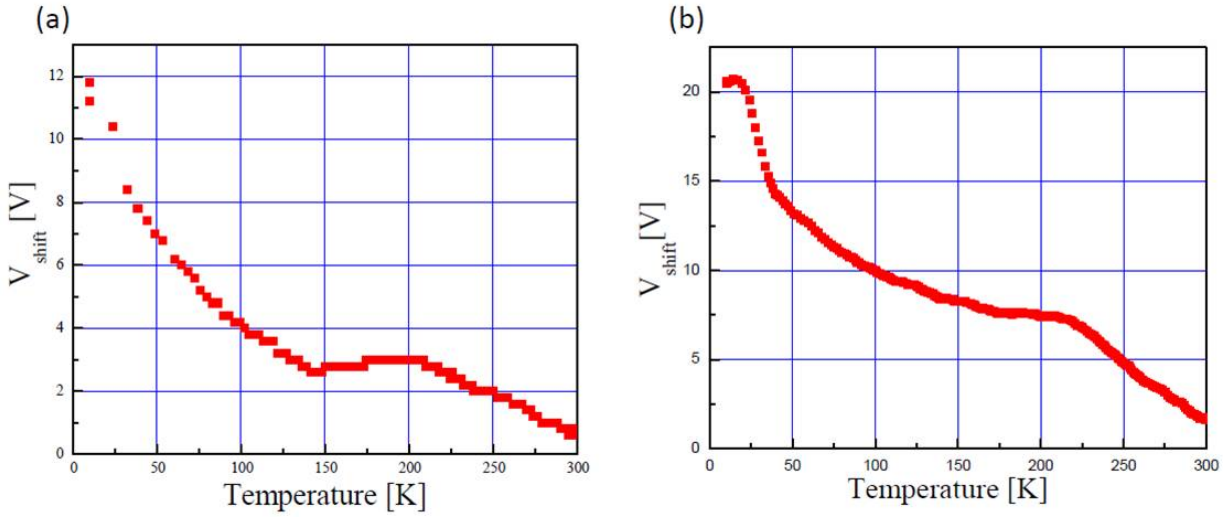

Figure 4.7: (a), (b) V_{shift} as a function of temperature for two different graphene devices. The heating rate of 4.2 to 1.0 K/min was used for both these samples.

Similar desorption behavior is observed, but there are some differences. We perform desorption measurements on four devices with mobility ranging from 5100 to 13400 cm^2/V sec in order to understand the differences in desorption characteristics. Multiple measure-anneal cycles are carried out on each device in order to understand the impact of annealing.

These experiments reveal that only hydrogen with a particular range of desorption energies "counts" the dominant scatterer. Figure 4.8(a) shows that the V_{shift} in temperature range of 150-200 K is proportional to the inverse initial mobility. Outside of this temperature range, the amount of V_{shift} induced is not correlated to the initial mobility as shown in Figure 4.8 (b-c). As such, we conclude that only hydrogen, desorbing between 150 and 200 K, count the dominant scatterer. The same scatterers are also responsible for the variations in device performance observed after thermal annealing as all data fall on the same slope. A linear fit shows that $1/\mu$ = (6.67 $\pm$1.07) $\times$ $10^{-5}V_{shift(150-200K)}$ + $(1.09 \pm 0.24) \times 10^{-4}$Vsec/$cm^2$. The maximum value for mobility with $V_{shift(150-200K)}$ at zero corresponds well to the maximum observed mobility of graphene on silicon oxide, consistent with these hydrogen atoms counting the dominant scatterer on SiO_2.

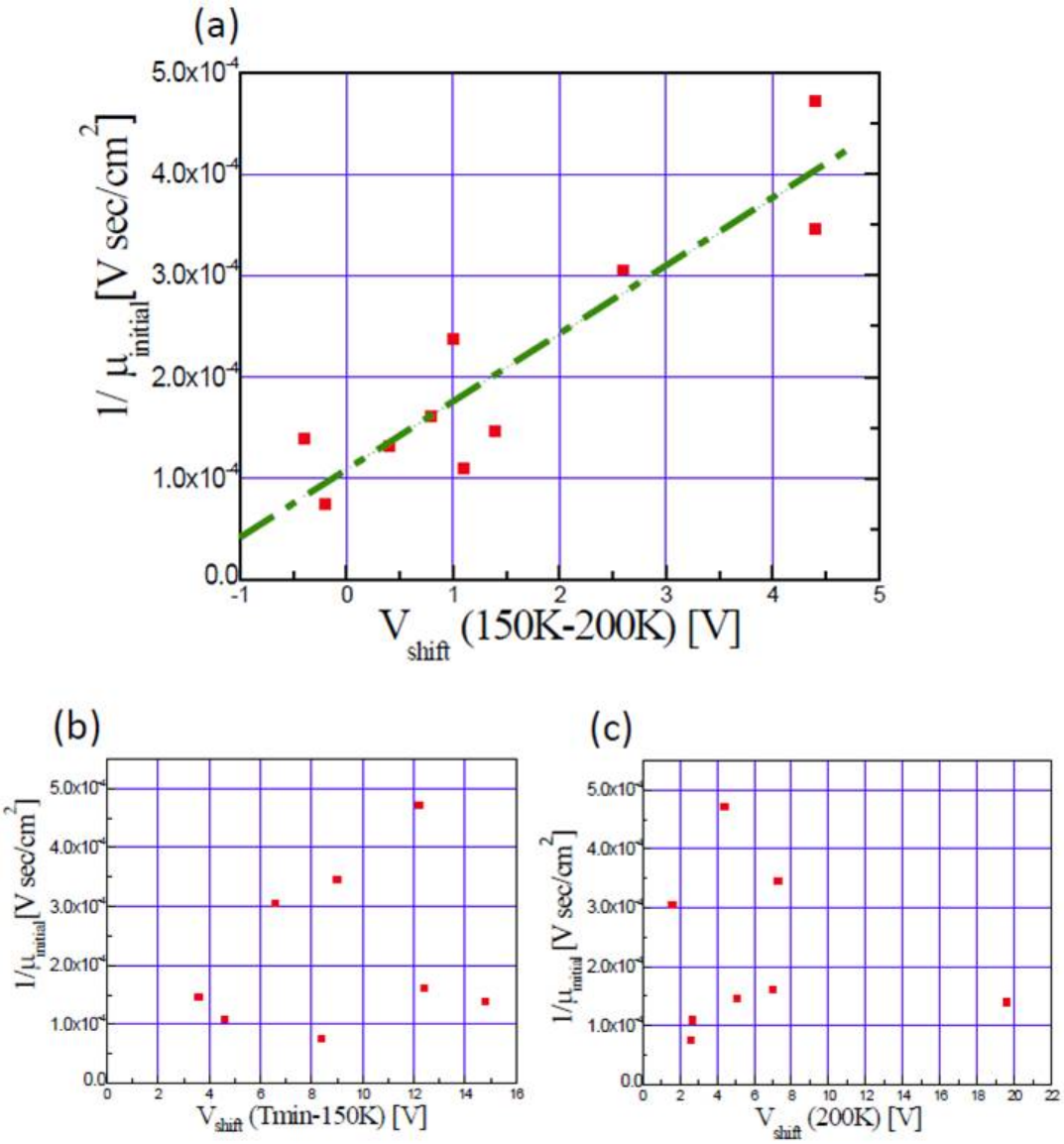

Figure 4.8: V_{shift} in specific temperature ranges as a function of inverse initial mobility of all the measured graphene samples showing (a) V_{shift} in temperature range 150-200K, (b) V_{shift} below 150 K and (c) V_{shift} above 200 K.

Furthermore, the intercept also indicates that other scattering mechanisms are responsible to reduce the maximum mobility down to $\sim 10,000 \mathrm{cm}^2$/V sec on SiO_2 from higher mobility seen on hexagonal boron nitride or in suspended devices.

Finding charge donated per hydrogen, desorbing between 150 and 200 K, is necessary to determine the relationship between the mobility and the number of scattering sites and, therefore, the scattering strength of the dominant scatterer. For 1st order desorption,

$$E_{desorption} = kT_{max}[ln(fT_{Tax}/\beta) - 3.64], \tag{4.1}$$

where k is the Boltzmann constant, $\mathrm{T_{max}}$ is the temperature of maximum desorption rate in K, f is the attempt frequency in Hz, and β is the heating rate in K/sec [108]. While the attempt frequency is difficult to determine directly, it is often assumed that f = kT/h, where T is the surface temperature and h is the Planck's constant. Using $\mathrm{T_{max}}$ ranging from 150 to 200 K, we find the desorption energy ranging from 440 to 600 meV for hydrogen counting scattering sites. In order to calculate charge donated by these special hydrogen atoms, the total energy calculations are carried out within the density functional theory (DFT), using the grid-based real-space method with the projected augmented wave (PAW) method implemented in GPAW code [calculations done by Talat Rahman's group in UCF]. Wave functions, electron densities, and potentials are represented on grids in real space with the grid spacing of about 0.15 $\mathring{A}$. For simulating atomic hydrogen absorption on a clean graphene sheet, we use a supercell consisting of a (2×2) or (3×3) graphene sheet, hydrogen atoms that yields an H-(24×2) or H-(3×3) adsorbate on graphene, and vacuum slab of approximately 20$\mathring{A}$. The Brillouin zone in both case are sampled by a (7×7×1) or (5×5×1) Monkhorst-Pack grid2, respectively. Our calculation shows that hydrogen adsorbs on graphene with desorption energies of 40 meV or 0.73 eV with charge transfer of 0.004 and 0.06 electrons per hydrogen. Since the higher desorption energy found in our calculation is similar to the counting hydrogen we use charge transfer of 0.06 electrons per hydrogen to analyze our experimental data. This value, the data presented in Figure 4.8(a), and the gate capacitance yield $1/\mu = (5.2 \pm 0.84) \times 10^{-17}\mathrm{n} + (1.09 \pm 0.24) \times 10^{-4}\mathrm{Vsec/cm^2}$, where n is the number of adsorption sites, which is the number of the dominant scatterer since adsorbed hydrogen is known not to

cluster. The observed scattering strength is nearly 20 times smaller than expected for the resonant scatterers and 4 times smaller than expected for charged impurities. Therefore, our data strongly favors charged impurities as the dominant scatterer responsible for the variability in mobility of graphene on SiO_2.

In conclusion, we used atomic hydrogen to count the impurity density in graphene on SiO_2. Atomic hydrogen desorbs with various characteristic energy on increasing the sample temperatures. We find that the amount of adsorbed hydrogen with desorption energy ranging from 440 to 600 meV is correlated to the number of scatterers. The relationship between the number of scatterers and the initial field effect mobility shows that charged impurities are responsible for the variability observed in the performance of graphene-based field effect transistors on SiO_2.

CHAPTER 5: STM/AFM IMAGING OF GRAPHENE.

5.1 Graphene on different substrates.

When graphene is exfoliated or transferred on any substrate, the graphene-substrate adhesion interactions determine its morphology. The electronic properties of graphene are expected to be altered by the substrate corrugations [109],[33]. Moreover substrate phonons with large momentum, which can induce intervalley scattering, are suspected to induce large carrier scattering in graphene at room temperature. Previous temperature dependent resistivity measurements agree with theoretical consideration of the contribution from substrate phonons. Inelastic tunneling spectroscopy of graphene should be able to directly observe such contribution from substrates [110]. However, so far no direct evidence has been seen in the tunneling spectroscopy due to similar energies for phonons in SiO_2 and graphene. We expected to observe substrate phonon scattering effects by performing scanning tunneling spectroscopy on graphene exfoliated/transferred on various substrates.

STM/AFM was employed to probe graphene morphology at atomic scale on three different substrates: SiO_2, hexagon boron nitride (h-BN) and sapphire. Figure 5.1 shows the schematic of the graphene device with Au contact on substrate, where the sample is grounded and the STM tip is biased.

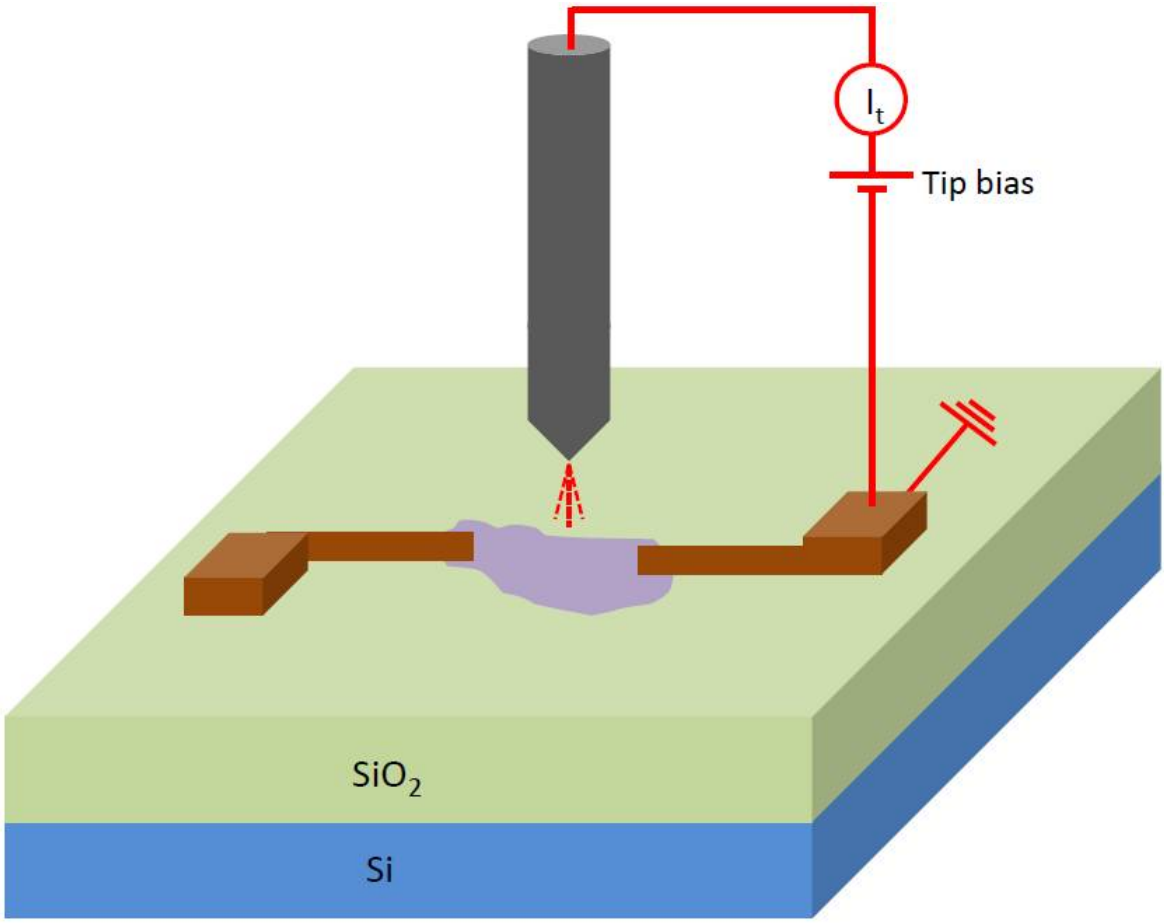

Figure 5.1: Schematic of scanning tunneling microscopy graphene device setup.

5.1.1 Graphene on SiO_2.

Figure 5.2 (a) shows 100 nm $\times$ 100 nm scanning tunneling microscopy image of CVD graphene transferred on SiO_2 substrate As reported in earlier studies, we observe that graphene morphology has 1nm high ripples due to partial conformation of graphene to SiO_2surface [32],[111],[112]. The atomic resolution image of the graphene hexagonal lattice is shown in Figure 5.2(b). The SiO_2 surface has charge traps and is highly corrugated. These charge traps not only scatter charge carriers in graphene as well as electronically breaks it down into electron and hole puddles at low charge carrier density [113].

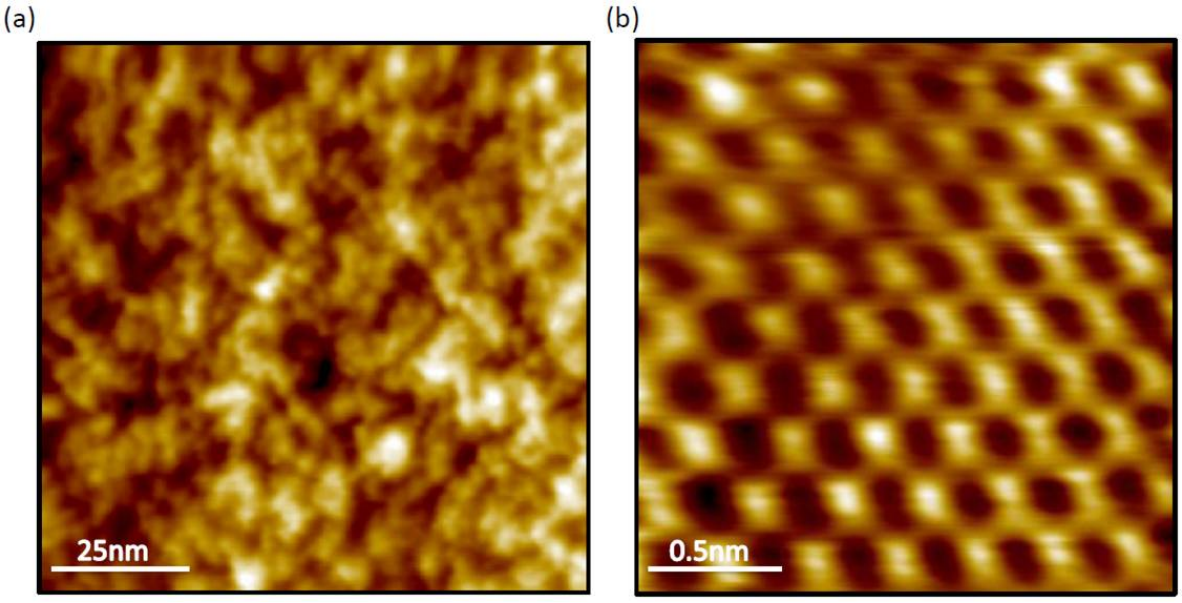

Figure 5.2: (a) 100 nm $\times$ 100 nm STM image of graphene on SiO_2 and (b) Atomic resolution of the same graphene sample.

These charge fluctuations make it difficult to study physics near the Dirac point.

5.1.2. Graphene on hexagonal Boron nitride (h-BN)

Lui et al. [35], reported high resolution atomic force microscopy of graphene on mica, with height variations less than 25 pm. However at ambient conditions, defects in mica act as nucleation sites and result in formation of epitaxial water adlayer on its surface.[114] Meanwhile hexagonal boron nitride emerged as another flat and inert substrate with relatively less charge puddles [75]. Moreover since the dielectric properties of h-BN are similar to SiO_2, so it is also suitable for use as gate dielectric. The electronic transport measurements of graphene on hBN have been demonstrated to exhibit high mobility of 100,000 cm^2/V sec [101].

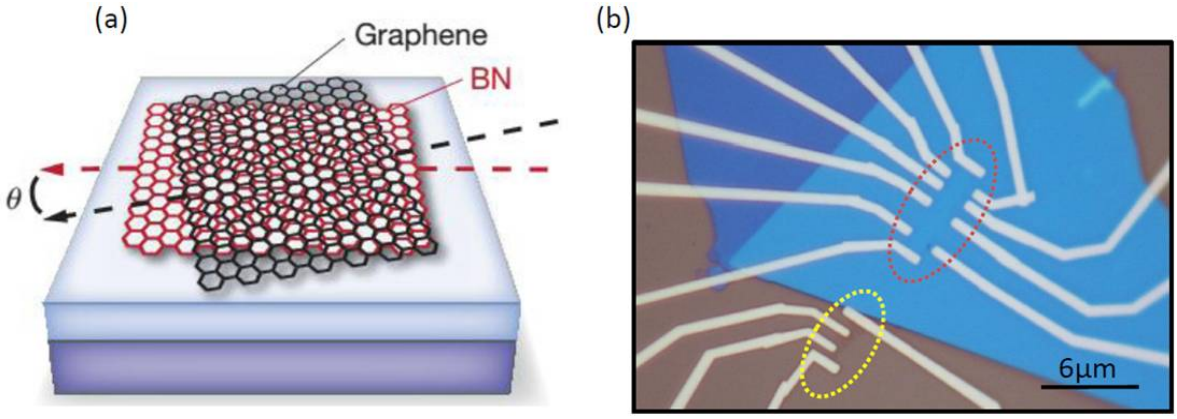

Figure 5.3: (a) Schematic of graphene on h-BN with emergence of Mori$\acute{e}$ pattern and (b) Optical image of Bernal-stacked bilayer graphene device on h-BN (area highlighted by red dots) and SiO_2 (area highlighted by yellow dots).

Additionally h-BN has a hexongal lattice structure similar to that of graphene, with lattice constant only 1.8% longer. Due to this when graphene is placed on h-BN as shown in schematic in Figure 5.3(a), the coupling between them results in distinct periodic modulations referred to as morie pattern [115],[116], [117]. The length of these modulations depends on the mismatch between the two lattices. Figure 5.3(b) shows optical image of Bernal-stacked bilayer graphene device on h-BN and SiO_2. We used room temperature high resolution non-contact AFM to image the mori$\acute{e}$ pattern generated by bilayer graphene on h-BN. Figure 5.4 shows the triangular mori$\acute{e}$ pattern with wavelength 15.5 ± 0.9 nm. This is comparable to the mori$\acute{e}$ wavelength ~ 14 nm expected for graphene on h-BN [115],[116], [117], suggesting near zero angle mismatch between bilayer graphene and h-BN. Furthermore our collaborators carried out the transport measurements of this device in the presence of externally applied high magnetic fields. Since the periodic potential created by this mori$\acute{e}$ pattern is of the order of the magnetic field, the 2D electrons exhibit a self-similar recursive energy spectrum known as Hofstadter's butterfly [101]. This is the first experimental realization of Hofstadter's butterfly energy spectrum after its theoretical prediction forty years ago. Thus mori$\acute{e}$ supperlattices arising in graphene on h-BN can give rise to very rich physics.

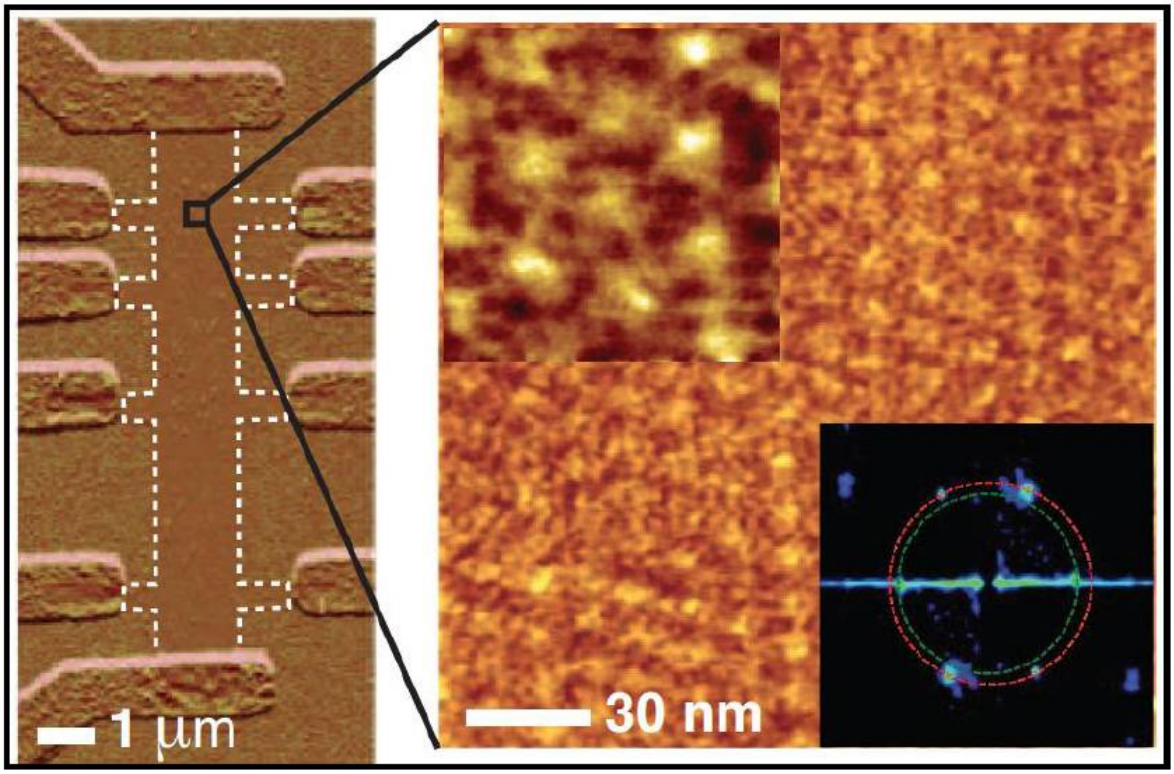

Figure 5.4: Left figure shows a non-contact AFM image of multi-terminal Hall bar device of bilayer graphene on h-BN. Right shows high resolution image in a magnified region. The moiré pattern is evident as a triangular lattice (upper inset shows a further magnified region). FFT of the scan area(lower inset) confirms a triangular lattice symmetry with period 15.5 $\pm$ 0.9 nm. Imaging was performed at room temperature using V_{bias} =0.2 V and f =20 Hz.

5.1.3. Graphene on sapphire

Figure 5.5(a) shows the AFM topography image of sapphire substrate, taken at ambient conditions. The sapphire surface is reconstructed by annealing in air at 1000 °C for 2hrs (15), resulting in atomically flat terraces as shown in Figure 5.5(b). The step height and width of these terraces is about 0.27 $\pm$ 0.03 nm and 60 $\pm$ 10 nm respectively. As seen in Figure 5.5(c) after reconstruction the sapphire surface also has few bigger terraces.

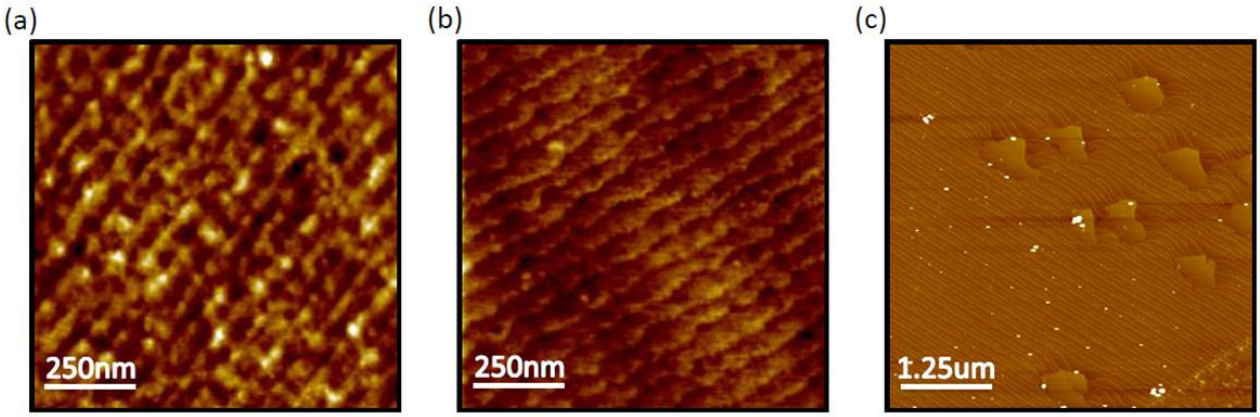

Figure 5.5: (a) AFM image of sapphire before and (b) after reconstruction of its surface, and (c) AFM image showing varying size terraces on the sapphire surface.

Before mechanical exfoliation of graphene on sapphire, it is cleaned by dipping in piranha solution (H_2SO_4 : H_2O_2= 3:1) for 10 min, is followed by an ultra-sonic treatment in water for 5 minutes. The acidic treatment of the substrate leaves OH group on the surface, making the substrate hydrophilic. This results in a water layer adsorption on its surface. After device fabrication the graphene surface was cleaned down to atomic scale using H_2/Ar annealing.

Figure 5.6(a) shows the 500 nm $\times$ 500 nm STM image of graphene on sapphire taken at 4 K. Graphene conforms to the terraces on the sapphire surface and exhibits unique bright (high) and dark (low) features everywhere on its topography as seen in Figure 5.6(b). Figure 5.6(c) shows 30 nm $\times$ 30 nm scan of graphene on a big terrace of sapphire. On further decreasing the scan area to investigate these bright and dark features, we obtain atomic resolution in Figures 5.6 (d), 5.6(e) and 5.6(f). This suggests that graphene itself is atomically clean and these bright and dark features are arising from below the graphene surface.

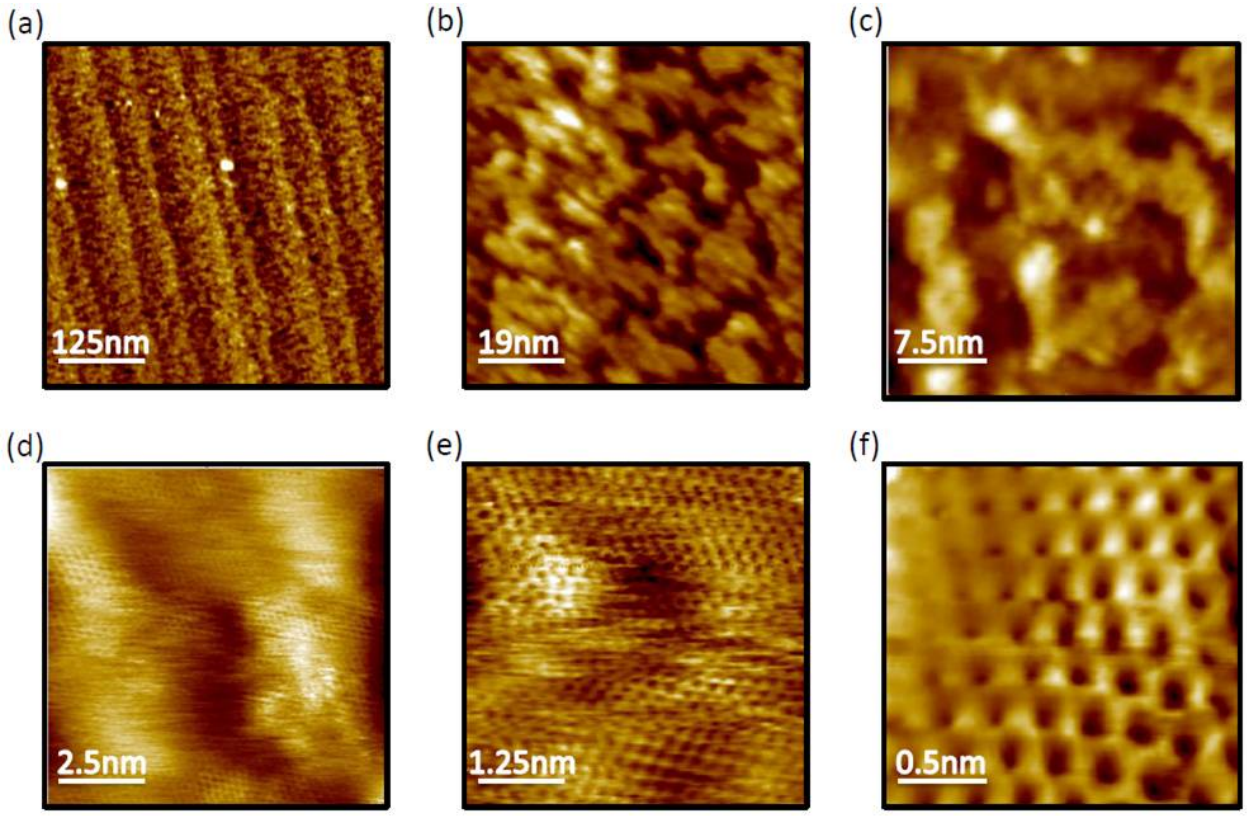

Figure 5.6: (a) STM topography of graphene on sapphire, (b) 77.9 nm $\times$ 77.9 nm scan of graphene, showing bright and dark region, (c) zoom in of these dark/bright spots, (d), (e)and (f) Topography of graphene on sapphire showing atomic resolution of the graphene on sapphire in different scan areas. These images confirms that graphene is atomically clean and these dark/bright spots are coming from interface between graphene and sapphire.

Figure 5.7(a) and 5.7(b) shows the three-dimensional topography of the graphene, conforming to the step edge of the sapphire terrace. The dotted lines represent the edge of the terraces in Figure 5.7(a). Previously AFM study of graphene on sapphire surface, has observed water layer adsorbed on the sapphire surface after acidic treatment [118]. We believe that these bright features correspond to protrusions in the graphene morphology due to underlying water layer.

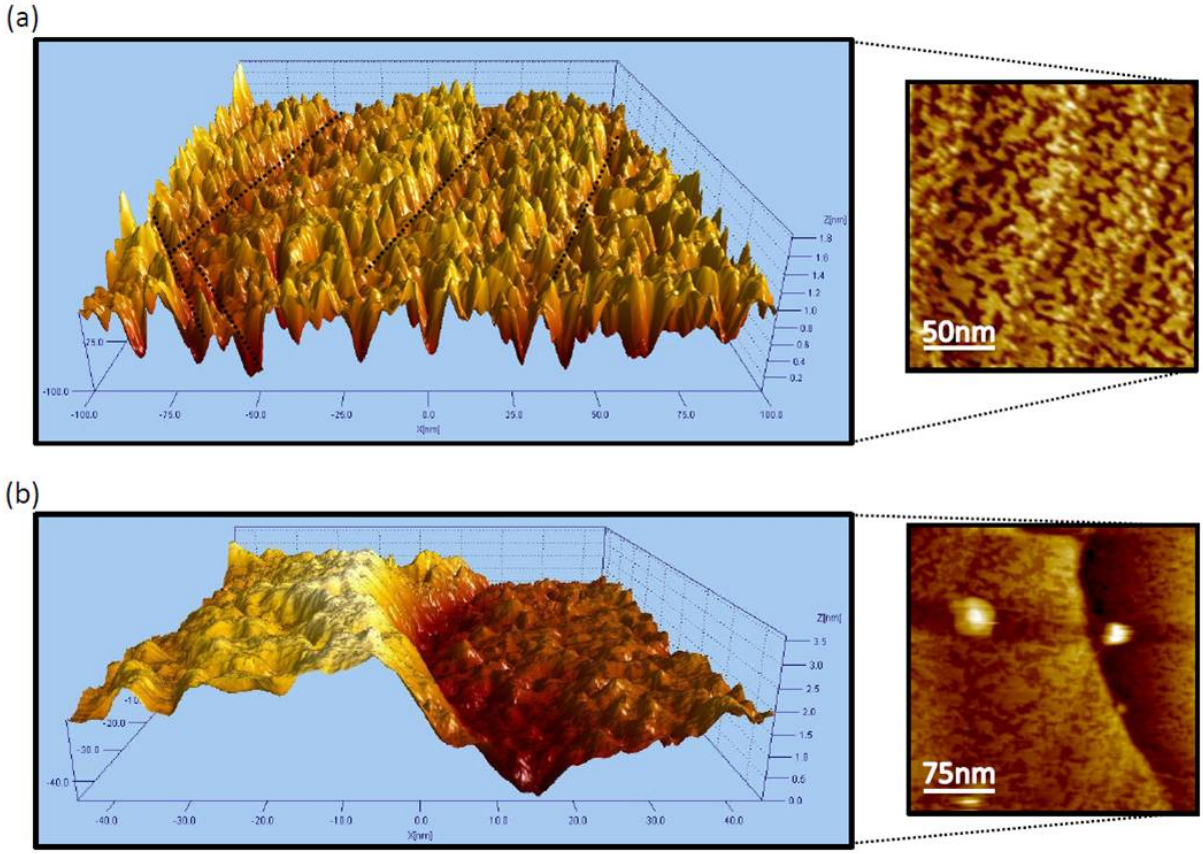

Figure 5.7: (a) and (b) The three dimensional rendering of graphene morphology on sapphire substrate. The graphene is clearly following the underlying substrate for different height steps.

5.2 Artifically created disorder in graphene

Graphene itself is non-magnetic, however artificially created atomic vacancies can be a source of magnetism [119]. These defects greatly influence its electronic, mechanical and magnetic properties. Using STM studies, it has been demonstrated that a single carbon vacancy in graphite gives rise to a sharp resonance near Fermi level associated with formation of local magnetic moment [120].

Chen et al reported electronic transport measurement of graphene with artificially created Ar^+ vacancies. Their data exhibit that the local moment associated with defects is strongly coupled to the conduction electrons in graphene and give rise to gate tunable Kondo effect [121]. However one expects Kondo effect to be strongly suppressed in graphene due to its low density of states. The fact that during the experiment, Ar^+ irradiated graphene sample was exposed to air make observed Kondo effect due to vacancy ambiguous. The STM/STS studies of artificially created vacancy in graphene in controlled environment can be really helpful in understanding if reaction of vacancies with magnetic impurities on exposure to air lead to observed kondo effect in graphene.

For carrying out these studies we first choose to study Ar^+ defects on highly ordered pyrolytic graphite (HOPG) crystal in UHV at 5 K. Figure 5.8(a) shows every adatom of freshly cleaved atomically clean HOPG. Carbon vacancies are created by in-situ bombardment of the surface with 140 eV Ar^+ ion for 10 sec. This energy is above the threshold energy (100 eV) for creation of carbon vacancy by Ar^+ ion. The defects are visible as protrusions (bright spots) on the 40 nm $\times$ 40 nm topography of HOPG after ion bombardment as shown in Figure 5.8(b). Each protrusion on the graphite is a manifestation of the ion impact [122]. The defect density on graphite was found to be 7×10^{12} /cm^2.

Figure 5.9(a) shows a small area-scan with multiple carbon vacancy on the surface of the graphite. The 3D view of the same defect clearly shows reconstruction on the surface of the graphite due to change of local electronic density of states caused by the defect as shown in Figure 5.9(b).

The STM images of a defect acquired at constant current and different bias voltage are shown in Figure 5.10 (a), and (b). Figure 5.11(a), (b), and (c) similarly shows STM topography of another defect on the graphite surface at different bias voltages. In these images at a particular bias voltage, the tunneling current is due to the contribution of electronic states between the Fermi level of the tip and the sample.

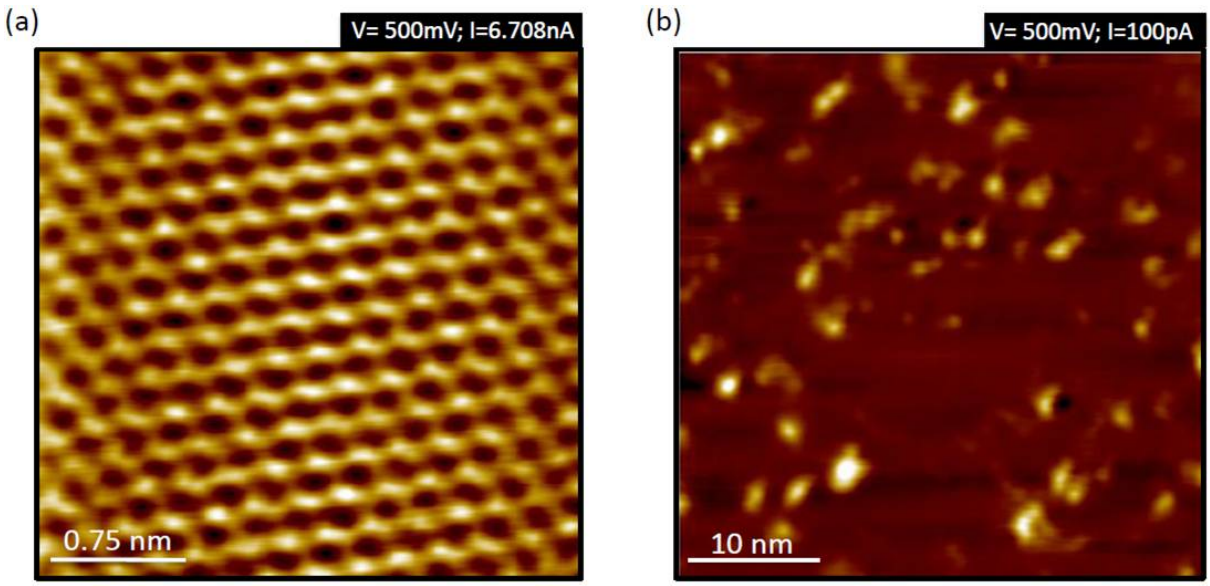

Figure 5.8: (a) STM image of atomically clean HOPG surface and (b) STM morphology of HOPG after Ar^+ ion bombardment. The missing carbon appear as protrusion or bright spot in this image.

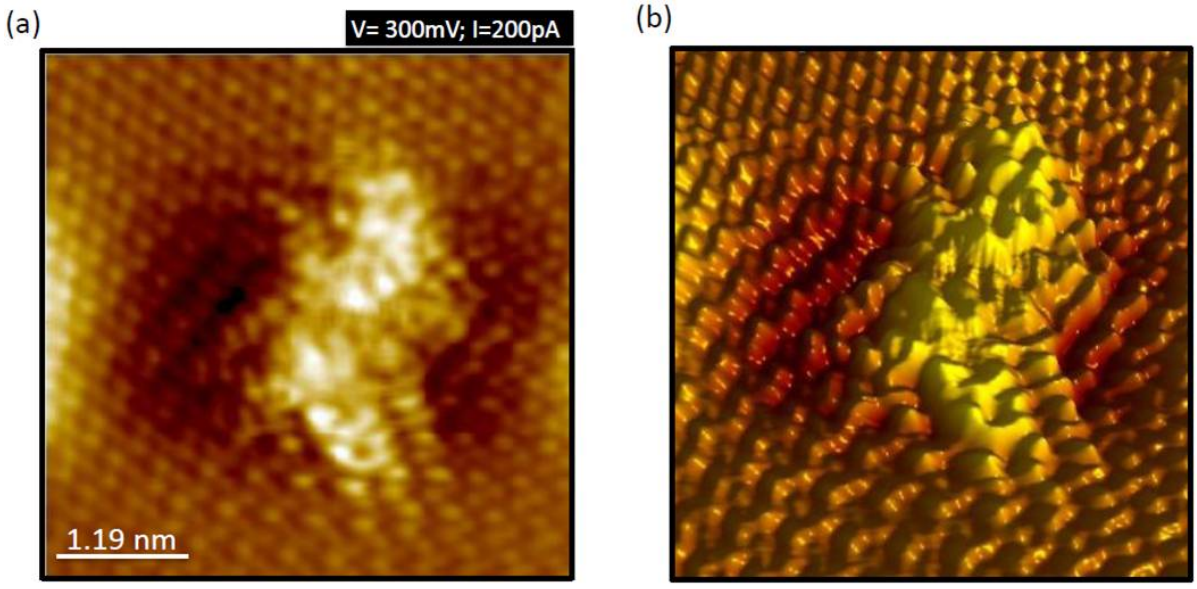

Figure 5.9: (a) and (b) Zoom in STM image of a defect on the HOPG surface and 3D rendering of this defect showing reconstruction on the surface of the HOPG

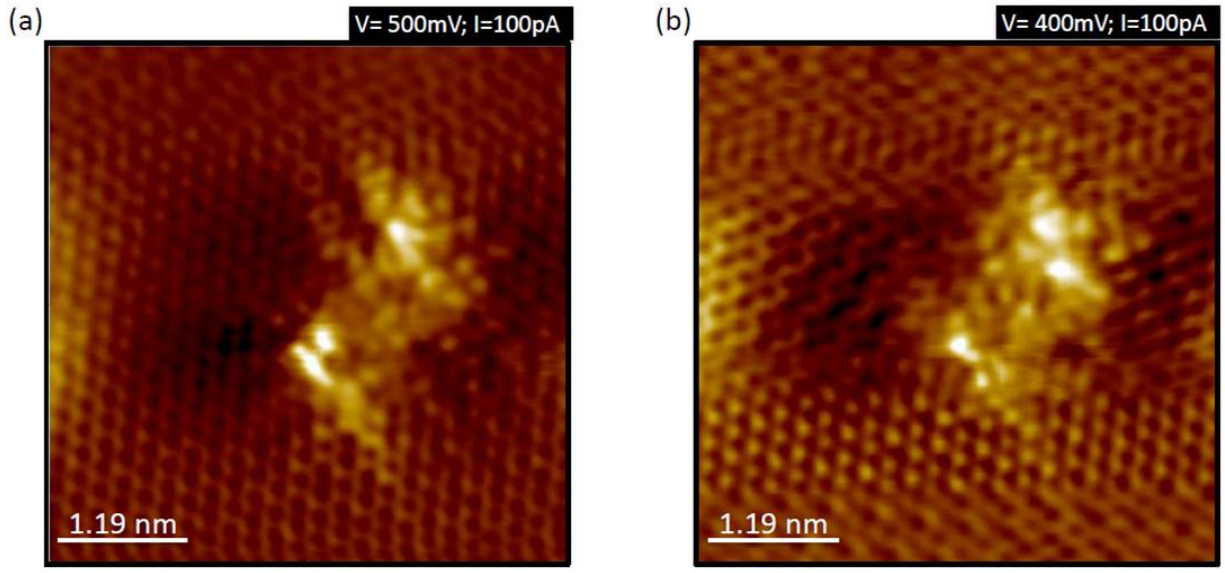

Figure 5.10: : (a) and (b) STM image of same defect on HOPG taken at a constant current and different voltages.

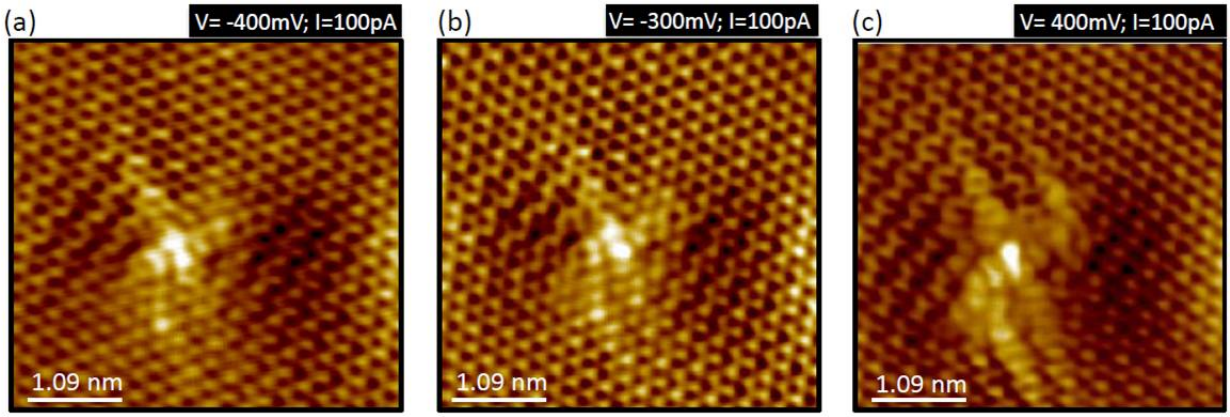

Figure 5.11: : (a),(b) and (c) STM image of another defect on HOPG taken at a constant current and different voltages. The images show $\sqrt{3} \times \sqrt{3}$ reconstruction on the HOPG surface due to this defect.

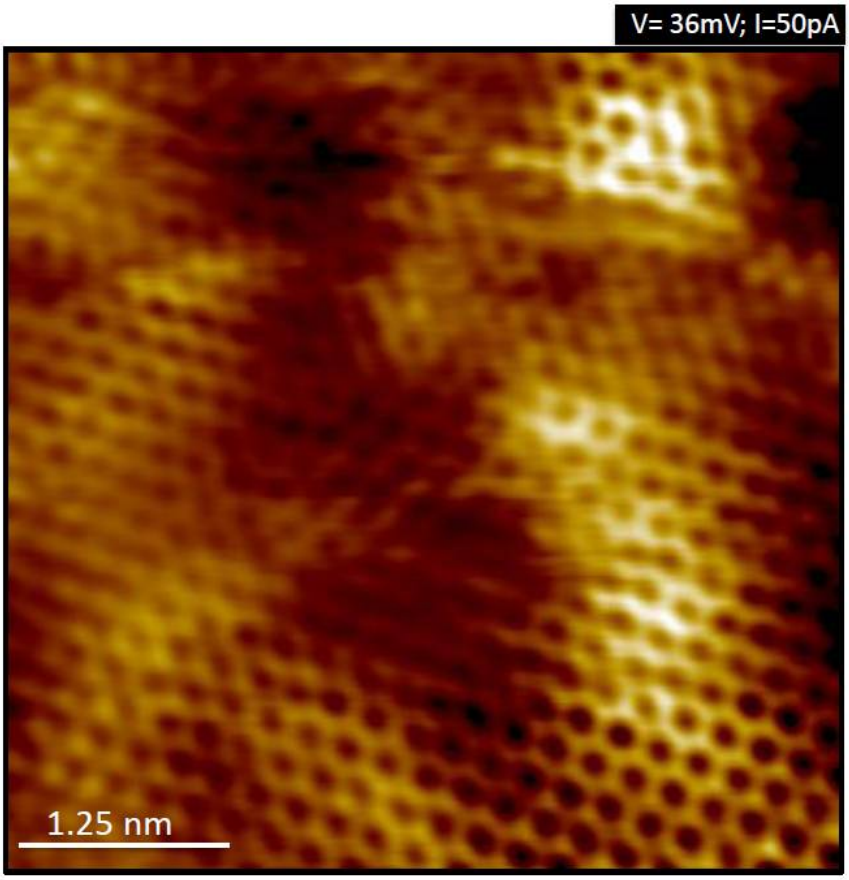

Figure 5.12: : 5 nm $\times$ 5 nm area scan, showing a atomically clean CVD graphene on SiO_2.

After reproducibly creating and successfully imaging defects on graphite, we changed the sample to CVD graphene. Figure 5.12 shows STM topography of atomically clean graphene on SiO_2 before irradiation with Ar^+ ions. Figure 5.13 (a), (b) and (c) show carbon vacancy on the graphene surface after bombardment with 140eV Ar^+ ion for 10sec. These defects again appear as high protrusion on the graphene surface.

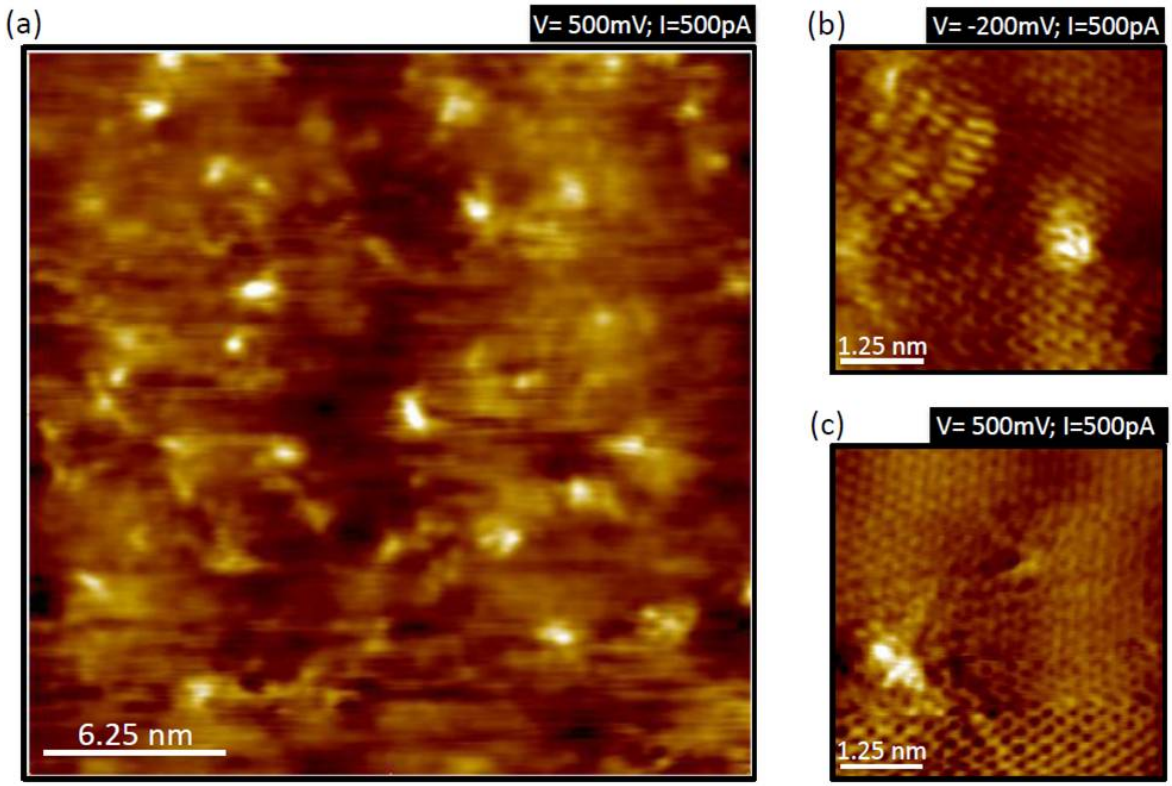

Figure 5.13: : (a), (b) and (c) STM morphology of graphene surface after exposure to Ar^+ ions. Clearly the defects are visible as protrusion or bright spots.

Higher resolution imaging of one such defect at a constant current and different bias voltages is shown in Figure 5.14 (a), (b), (c), (d), (e), and (f). These images clearly show that for positive tip bias the occupied and for negative bias unoccupied states contribute to the tunneling current.

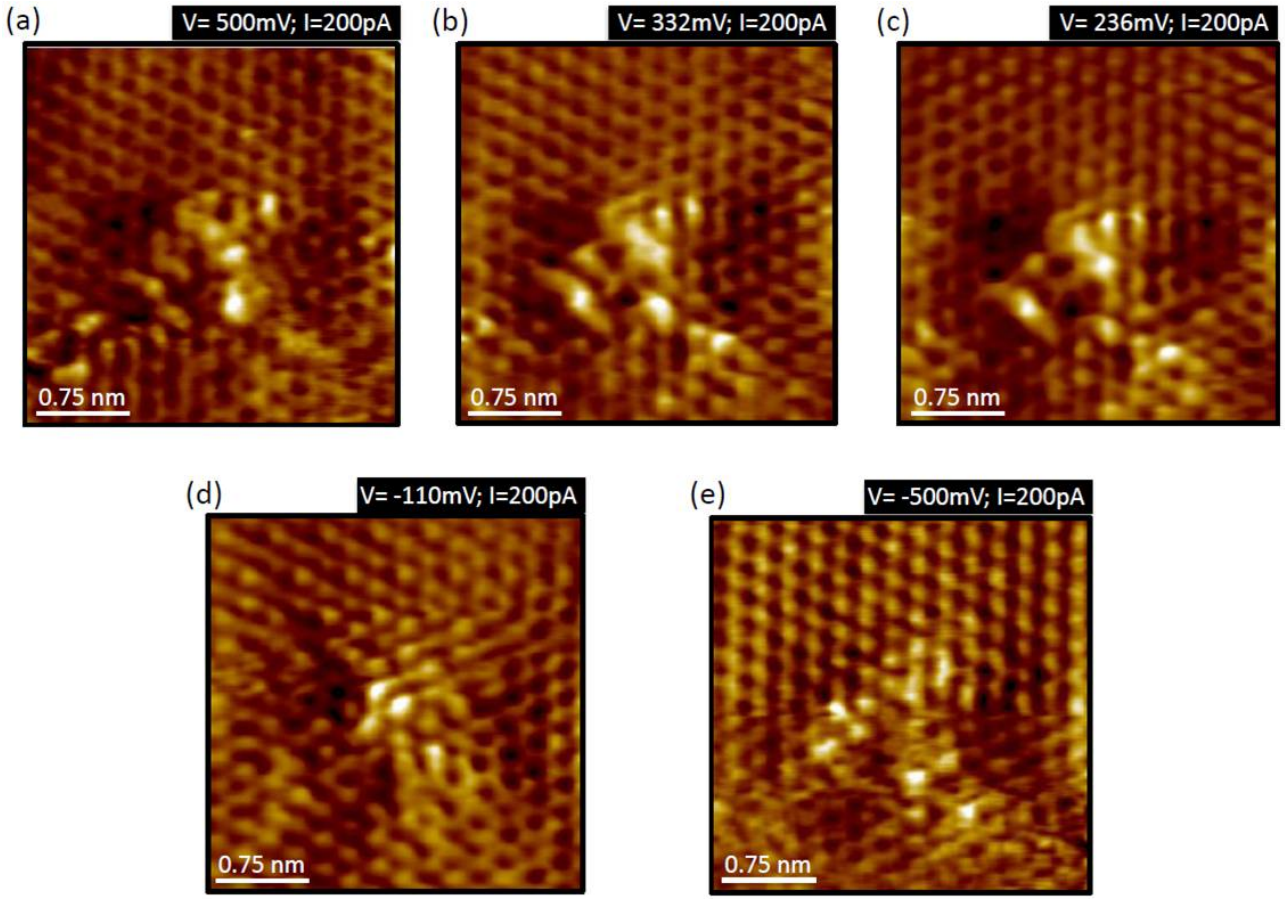

Figure 5.14: : (a), (b), (c), (d), (e) and (f) STM image of same defect, taken at constant current and different voltage. These images clearly show that for positive tip bias the occupied and for negative bias unoccupied states contribute to the tunneling current.

We successful created atomic scale defects on the surface of the graphene and graphite. Defect structures on the graphene surface were found to vary significantly. Local densities of states probed using STS did not show any signatures of enhanced densities of states near the charge neutrality point.

CHAPTER 6: FUNCTIONALIZATION OF MOLYBDENUM DISULFIDE.

So far researchers have seen that the optically direct bandgap in the single-layer MoS_2 can be modified to optically indirect band gap by using uniaxial tensile mechanical strain in the range of 0-2.2% [1].An alternate way to modify the bandgap can be by functionalizing MoS_2. DFT calculations show that atomic hydrogen/fluorination dosage can render MoS_2metallic [123]. This means that we can use functionalized MoS_2 to derive full range of 2D integrated circuit technology.

In order to study the impact of ad-atoms on electronic properties of MoS_2 we carried out hydrogenation (section 6.2)and fluorination (section 6.3) of single- layer MoS_2 on SiO_2. Theoretical calculations show ad-atoms can induce ferromagnetism as well as metal-semiconductor transition.

6.1 Comparison of monolayer CVD MoS_2 and bulk MoS_2- defects

Figure 6.1(a), and (b) show the STM topography of different areas on freshly cleaved naturally occurring type1 (small crystal) bulk MoS_2 purchased from SPI. The image clearly shows that the MoS_2 surface is riddled with defects on its surface. These intrinsic defects can be both S and Mo vacancy. Another freshly cleaved type2 (large crystal) MoS_2 also showed similar vacancies on its surface as shown in Figure 6.2(a) and (b). The atomic scale imaging clearly shows that the naturally occurring bulk MoS_2, used (commercially purchased) for exfoliating single layer can be highly defected.These defects vary in size as some of them are $<$ 1nm and some are even 2nm or bigger.We believe that these defects are responsible for lower intensity of PL peak at 1.8 eV and limited mobility for exfoliated single layer MoS_2 based FETs.

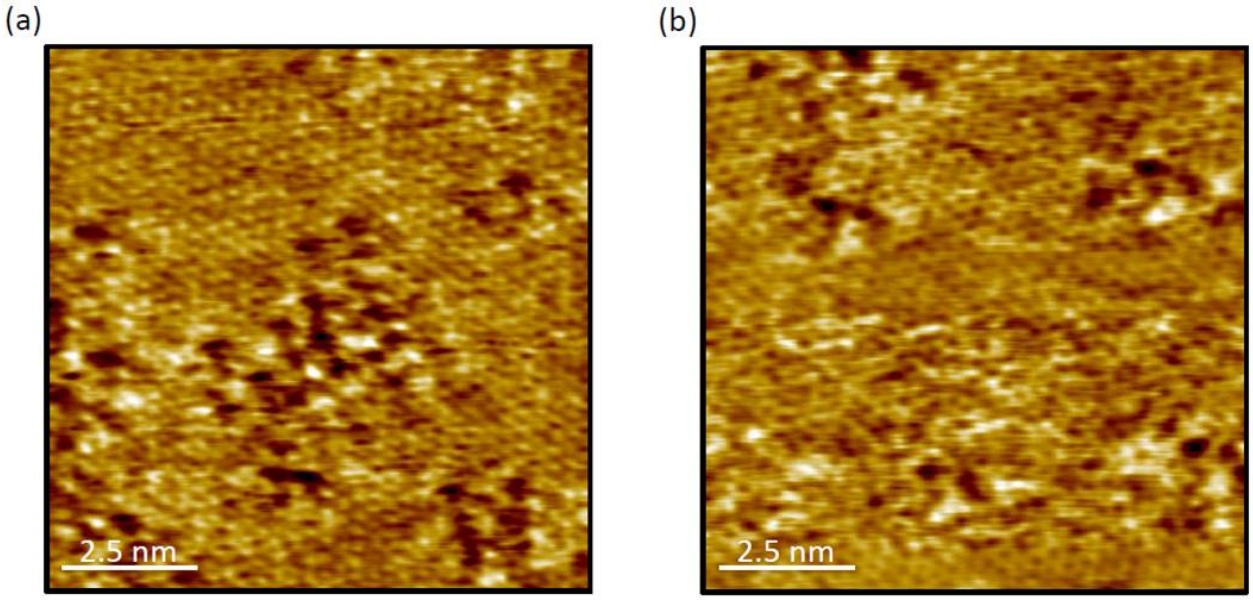

Figure 6.1: (a) and (b) 10 nm $\times$ 10 nm area scan of two different locations on freshly cleaved type1 (small crystal) bulk MoS_2.

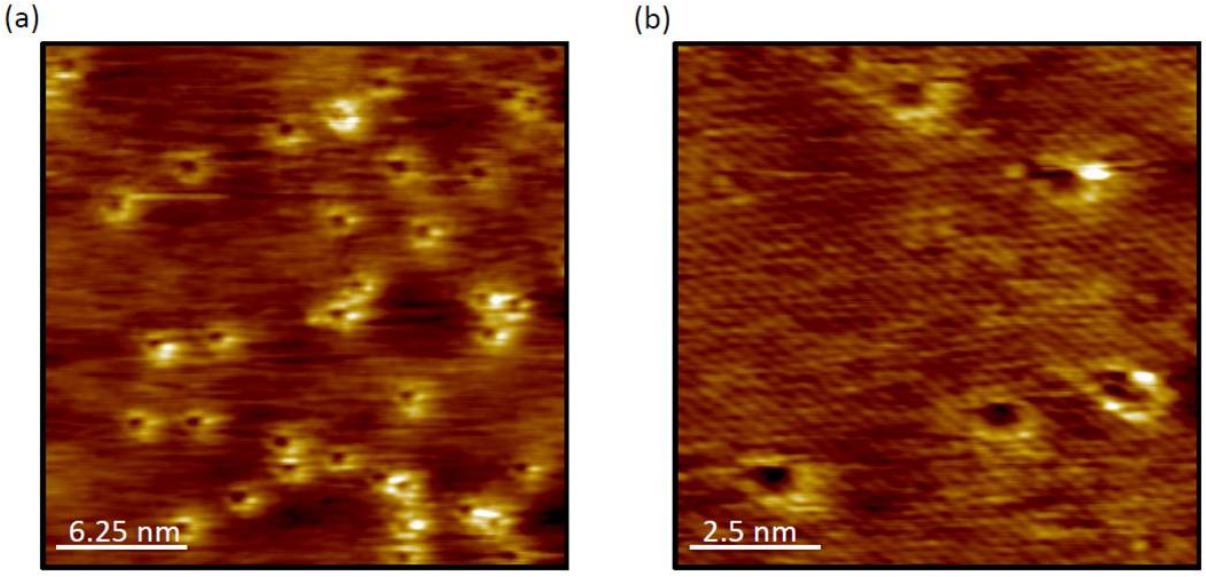

Figure 6.2: (a) STM topography of 25 nm $\times$ 25 nm area of freshly cleaved type 2 (large crystal) bulk MoS_2 and (b) Another STM scan showing defects in 10nm $\times$ 10 nm area on the same crystal at a different spot.

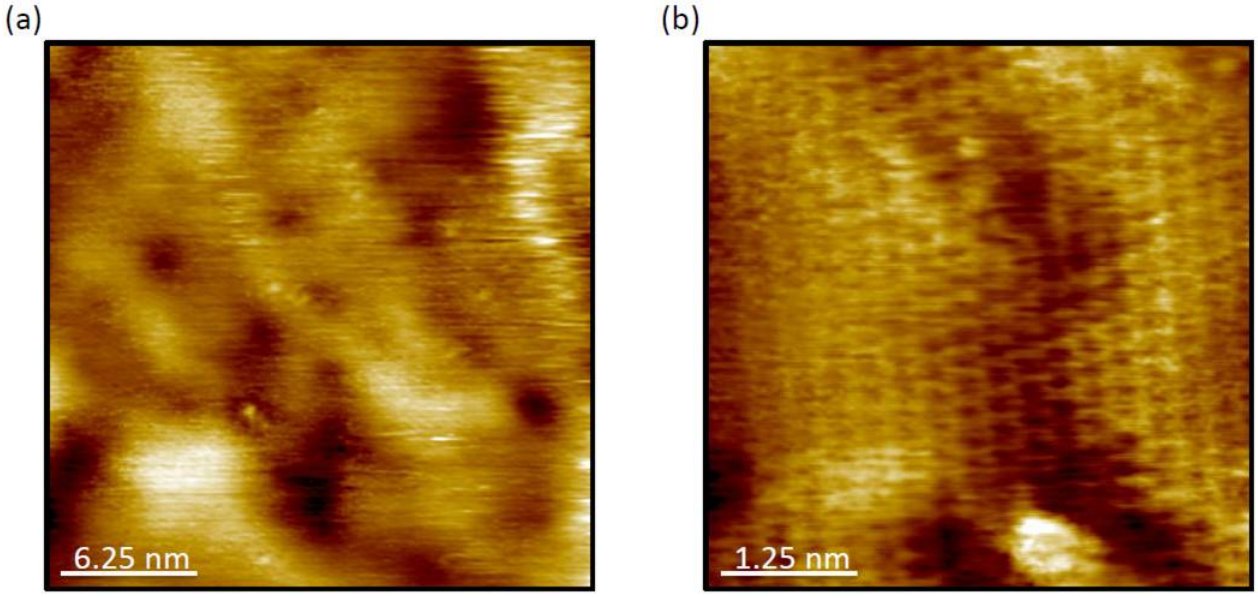

Figure 6.3: (a) STM topography of 25 nm^2 area of CVD single layer MoS_2 on SiO_2 and (b) Zoom in 5 nm $\times$ 5 nm scan showing hexagonal lattice of MoS_2. These images clearly show that CVD grown single layer MoS_2 also has few defects and adsorbates on its surface.

The Figure 6.3(a) and (b) shows the STM image of single layer CVD MoS_2 on SiO_2 substrate. Mostly the surface is atomically clean with few adsorbates on its surface. Also there seems to be far less number of atomic vacancies on the surface of CVD grown MoS_2 as compared to the bulk crystal.This may explain the higher intensity of the PL signal for CVD grown single layer MoS_2. The comparison of the PL spectrum of exfoliated and CVD grown single layer MoS_2 is shown in Figure 6.4(a) and (b).

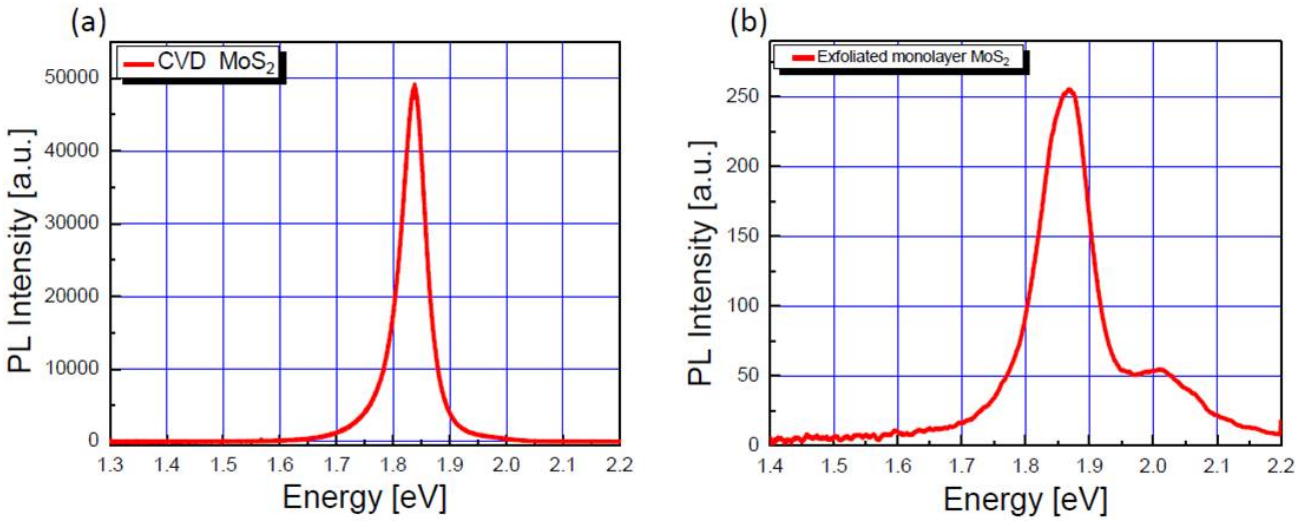

Figure 6.4: (a) High intensity photoluminescence peak at 1.83 eV for single layer CVD MoS_2 on SiO_2, and (b) The exfoliated MoS_2 on SiO_2 exhibit low intensity photoluminescence peak at 1.85 eV corresponding to direct band gap transition at K′.

6.2 Hydrogenation of single layer MoS_2

This study is carried out on CVD grown high quality single layer MoS_2 sample, shown in the Figure 6.5. The hydrogen plasma, generated in a 13.56 MHz capacitive coupled reactive ion chamber is used to hydrogenate the sample. It is operated at power density of 0.04 W/cm^2 (or power 5watt) and chamber pressure of 50 mTorr so that the MoS_2 is exposed to the low energy plasma.

Generated plasma is dominantly consisting of H_3^+ ions whose densities are an order magnitude greater than H^+ and H_2^+ ions. The reactive ion chamber used in this study doesn't have a provision to measure the absolute energy of the ions and the possible modifications to the chamber for such energy measurements were not recommended by the manufacturing company.

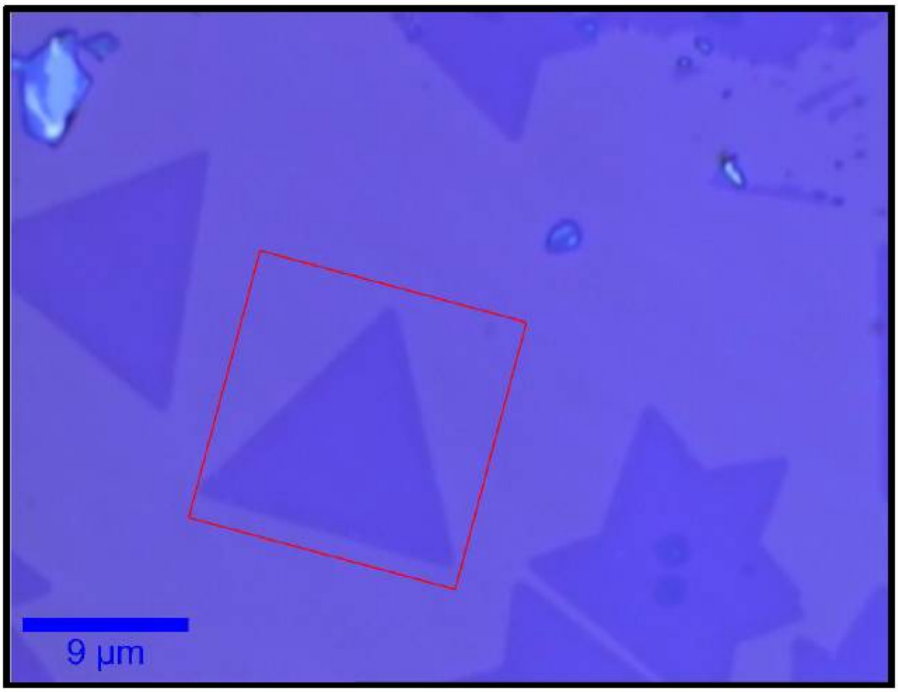

Figure 6.5: The optical image of single layer MoS_2 on SiO_2 substrate.The triangle shaped MoS_2 used in the experiment is marked by a red square box.

According to ref[124] (operating at similar plasma generation parameter as my experiment) the plasma ion energy can be estimated to be $\leq$15 eV. However, on estimating using ref [125] and ref[126] it can be about 55 eV (note in ref [125] they are using rf of 60 MHz and in ref [126] they have not given energy). Further the sample is exposed to hydrogen plasma for 1sec to minimize the damage may be caused due to these ions. For $E \leq mc^2$, the maximum energy transferred by these hydrogen ions in collision to the sample can be estimated by using the simplified binary collision equation

$$T_{max} = E\frac{4Mm}{(M+m)^2}, \tag{6.1}$$

Where E and m is the energy and mass of the bombarding hydrogen ions, and M is the mass of the Mo or S atom in MoS_2. The hydrogen ion of energy 15 eV (50 eV) will transfer approximately maximum of 2 eV (5 eV) energy to MoS_2 lattice.

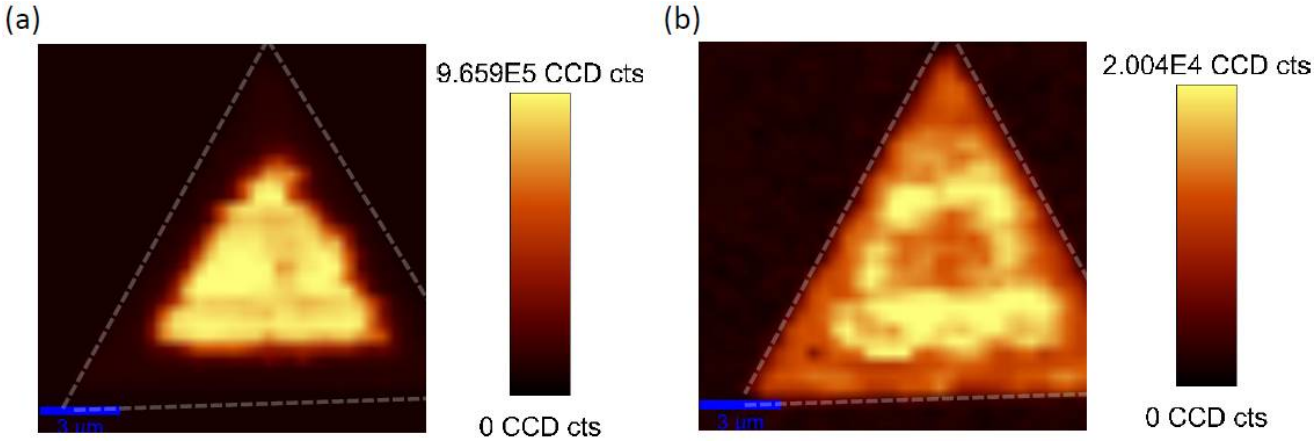

Figure 6.6: (a) PL mapping of the MoS_2 triangle before hydrogenation and (b) after hydrogenation. It is clear that PL intensity is decreased after hydrogenation treatment.

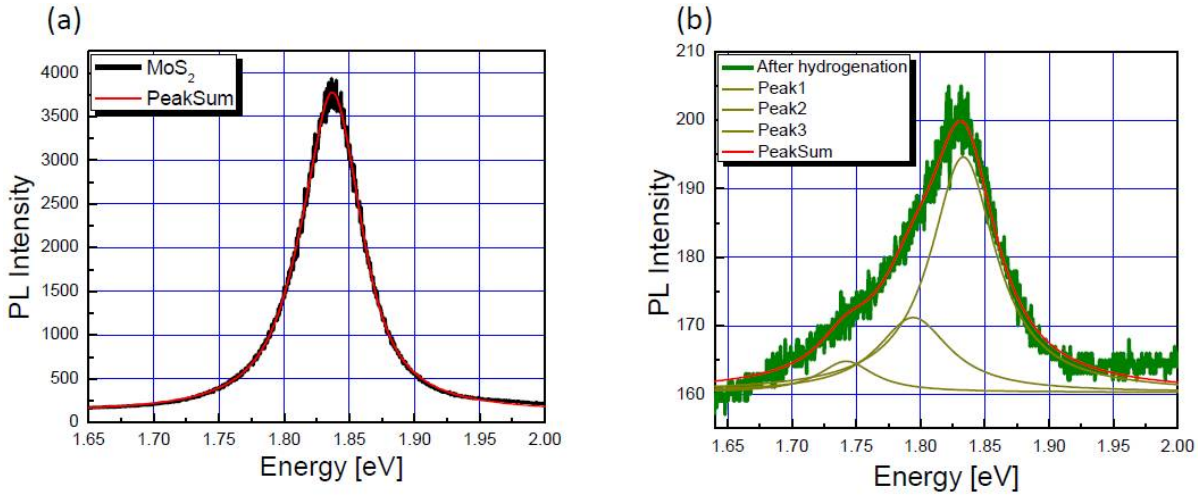

Figure 6.7: (a) PL spectrum of MoS_2 before hydrogenation has a peak at 1.83 eV. (b) PL spectrum of MoS_2 after hydrogenation has peaks at 1.83 eV and 1.78 eV.

These estimations indicate that hydrogen ion may not have energy needed to knock out sulfur atom and make vacancy in our sample [127].

The mapping of 15 μ m $\times$ 15 μm pristine CVD MoS_2 sample indicates spatial variation in PL intensity [128] as seen in Figure 6.6(a). The sample, particularly along the edges of the triangle has low PL intensity.

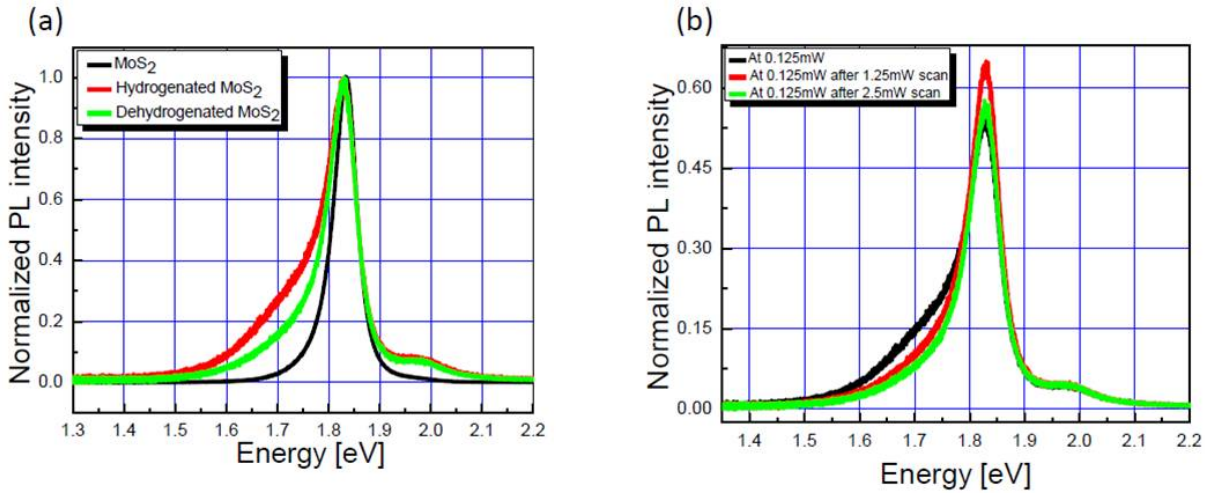

Figure 6.8: (a) Comparison of normalized PL signal of untreated, hydrogenated, and dehydrogenated MoS_2. (b) Localized dehydrogenation of MoS_2 with laser annealing

After hydrogenation, mapping of the same MoS_2 triangle shows quenching of PL signal in Figure 6.6(b). Interestingly, the PL signal is quenched non-uniformly as evident in at the center of the triangle. This may be related to the CVD MoS_2 growth mechanism but is not fully understood yet. The comparison of the single PL spectrum before and after hydrogenation is shown in Figure 6.7(a) and Figure 6.7(b). After hydrogenation a side peak appears at 1.78 eV. Such a peak at 1.78 eV has previously been reported due to defect induced bound exciton in $\mathrm{MoS_2}$ [129]. In order to study the interaction of hydrogen with MoS_2 I used local laser heating to selectively desorb the hydrogen. This peak starts to disappear on laser heating at power density of 1.59 mW/$\mu\mathrm{m}^2$ with scan time of 30 sec as shown in Figure 6.8(a) and Figure 6.8(b). Although the side peak disappear 90 $\%$ with successive laser heating, the PL intensity doesn't recover fully. This can be due to two possible reasons: (1) No hydrogen is bonding to $\mathrm{MoS_2}$ surface and the 1.78 eV is due to defects created by hydrogen plasma. The laser annealing in air can be healing these defects, which is observed as the decrease of this side peak. Also, the desorption of adsorbates like water, hydrocarbons, etc. on laser annealing can result in partial recovery of PL signal.

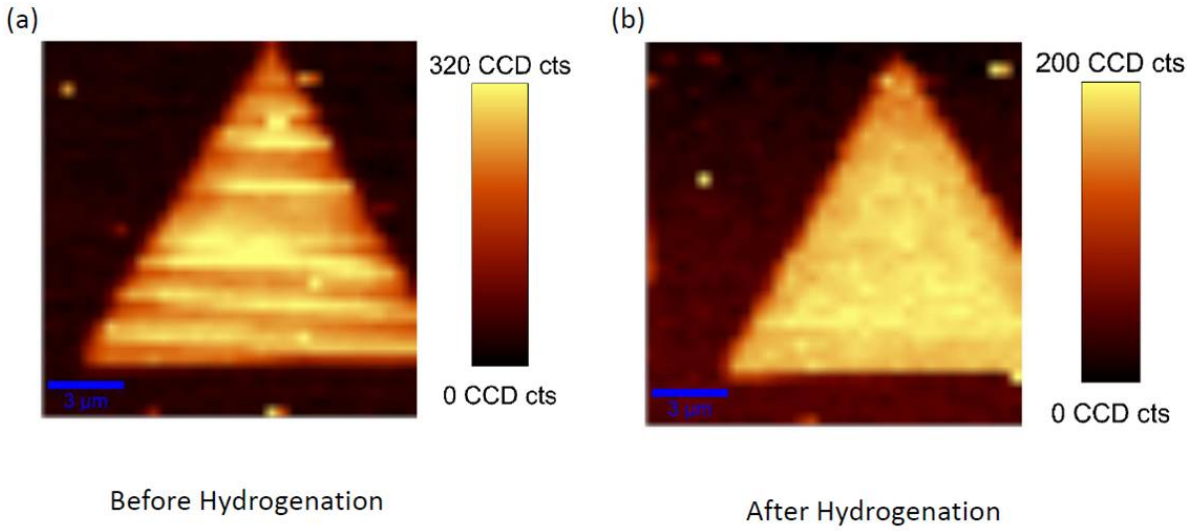

Figure 6.9: Raman mapping of MoS_2 before hydrogenation (left) and after hydrogenation (right)

However, I would like to add that only slight changes in the Raman peaks after hydrogenation clearly indicate that these defects are not disrupting the lattice of MoS_2 (discussed below) and that there only few defects being created by plasma (2) There is no damage due to low energy plasma. Hydrogen is binding to the surface which is seen as the side peak at 1.78 eV and laser annealing is desorbing hydrogen.

Upon hydrogenation, the Raman peaks do not disappear, further indicating that the basic lattice structure of molybdenum disulfide remains robust under hydrogenation as shown in Raman mapping of the same area in Figure 6.9. For the peak E'_{2g} (at 383 cm^{-1}) and A_{1g} (at 404 cm-$^{-1}$) the phonon frequency decreases by 1cm-$^{-1}$ .This shift is very small and indicates almost no doping effect due to hydrogenation and very gentle hydrogenation of the sample. The FWHM (full width half maximum) of peaks at E'_{2g} and A_{1g} increases after hydrogenation from 3.19 cm^{-1} to 4.25 cm^{-1} and from 4.24 cm^{-1} to 5.38 cm^{-1} respectively as shown in Figure 6.10 and Figure 6.11. Further it is not possible to confirm hydrogen binding to MoS_2 from Raman spectroscopy as S-H peak is masked by peak corresponding to photoluminescence peak of MoS_2.

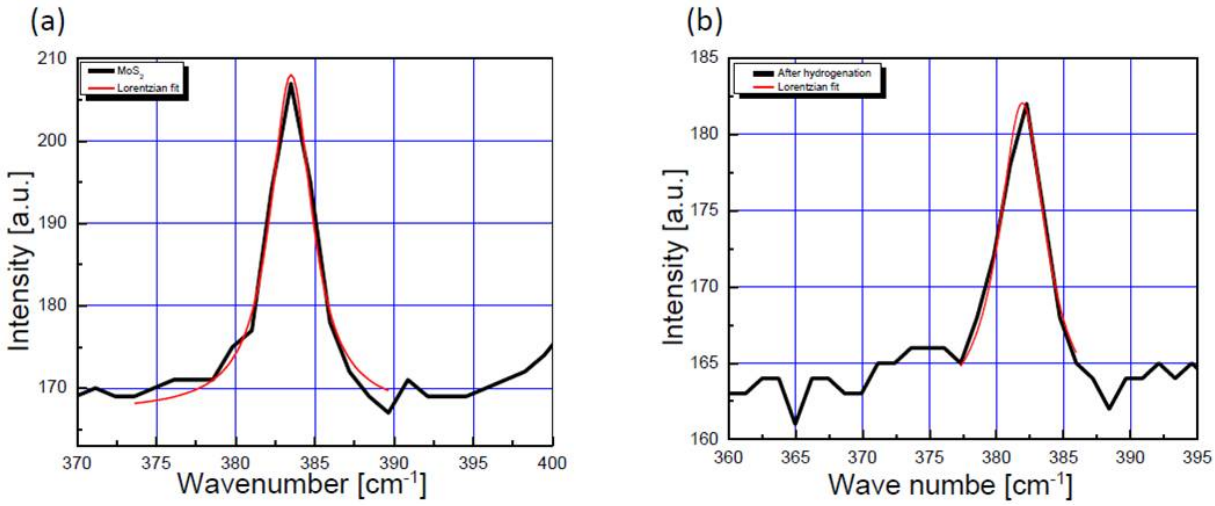

Figure 6.10: : FWHM of peak $\mathrm{E}^{'}_{2g}$ at 383 cm^{-1} before hydrogenation (left) and after hydrogenation (right).

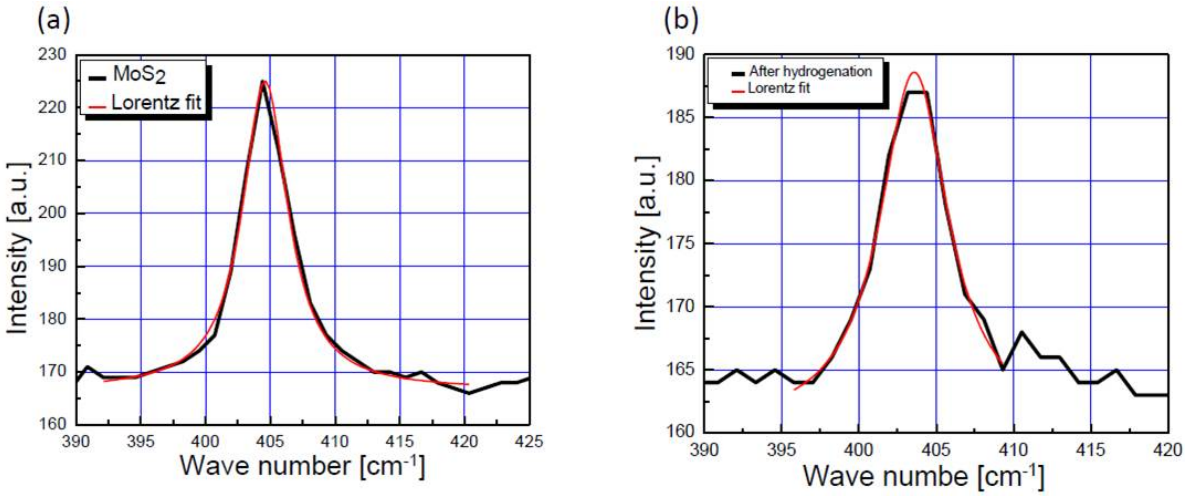

Figure 6.11: : FWHM of peak $\mathrm{A}^{'}_{1g}$ at 404 cm^{-1} before hydrogenation (left) and after hydrogenation (right).

In conclusion the observed side peak at 1.78 eV can be due to combination of both hydrogen binding to $\mathrm{MoS_2}$ and few defects formed during exposure to hydrogen plasma or either of these. The present study using PL and Raman spectroscopy is insufficient to conclude if hydrogen is binding and causing any modifications in electronic properties of $\mathrm{MoS_2}$. Furthermore the exposure to air after hydrogenation of the sample and optical measurements in ambient conditions, make it

even more difficult to conclude about the experimental observation. Transport measurements along with scanning tunneling imaging/spectroscopy before and after in-situ hydrogenation can help to understand modification of electronic properties of MoS_2 upon hydrogenation. Currently studies are being carried out to in-situ hydrogenate the MoS_2 devices in UHV STM using low energy hydrogen generated using hydrogen cracker.

6.3 Fluorination in monolayer MoS_2

The bulk MoS2 was fluorinated using CF_4 plasma in the reactive ion etcher. The plasma was generated using parameters: RF power-5 Watt, chamber pressure 100 mTorr, CF_4 flow- 5 sccm and sample exposure time- 1 sec.

We employed x ray photoelectron spectroscopy (XPS) study to understand binding of fluorine to the surface of bulk MoS_2 (purchased from SPI). We used Mg K α light of photon energy, hυ=1235.6 eV as X-ray source and MAC-2 electron spectrometer. The naturally occurring bulk MoS_2 has some carbon impurities and all the spectra were energy calibrated by assigning maximum in C1s spectrum to 284.5 eV. Figure 6.12 clearly shows that spectra exhibits a small F 1s binding energy peak at 690 eV after fluorination. However at this point it is not clear if this is due to bonding of fluorine to carbon impurities or the sulfur atom in MoS_2.

We then annealed the fluorinated sample in UHV in steps for 30 mins each at 100 °C, 200 °C and 250 °C to investigate defluorination of MoS_2 as shown in Figure 6.13. On heating at 100 °C the peak shifts to 689 eV and becomes smaller in intensity. Further heating at 200 °C doesn't further change the peak.

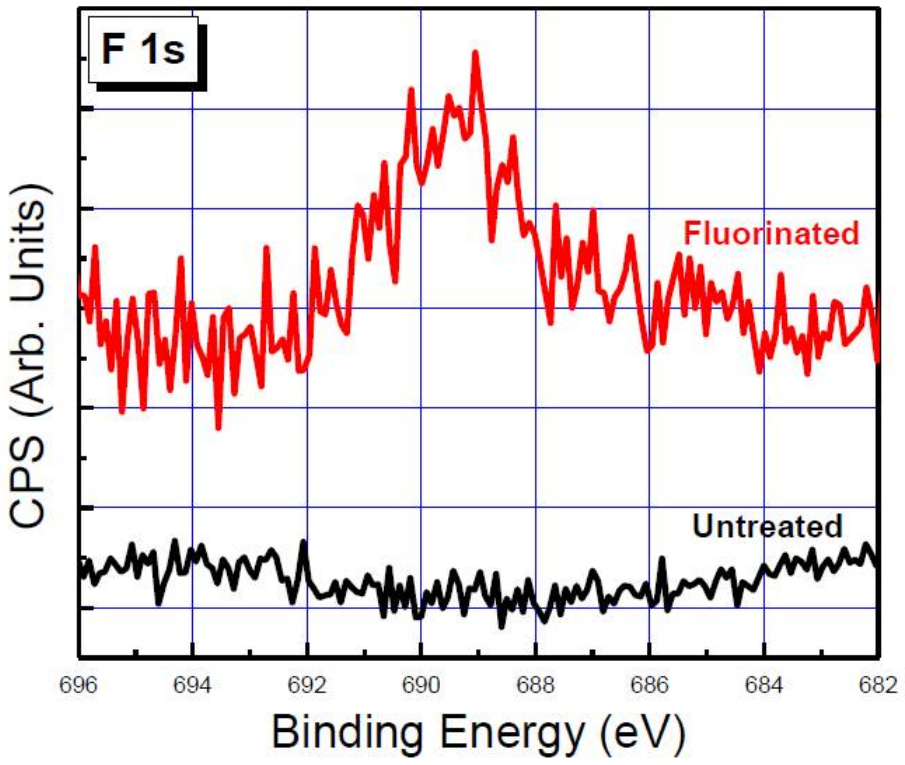

Figure 6.12: : F 1s X -ray Photoelectron Spectra of untreated (black) and fluorinated (red) bulk MoS_2.

At 250 °C the F 1s peak disappears and we obtain same spectrum as for the untreated MoS_2 sample. This tells us that fluorine is completely desorbed by annealing at 250 °C.

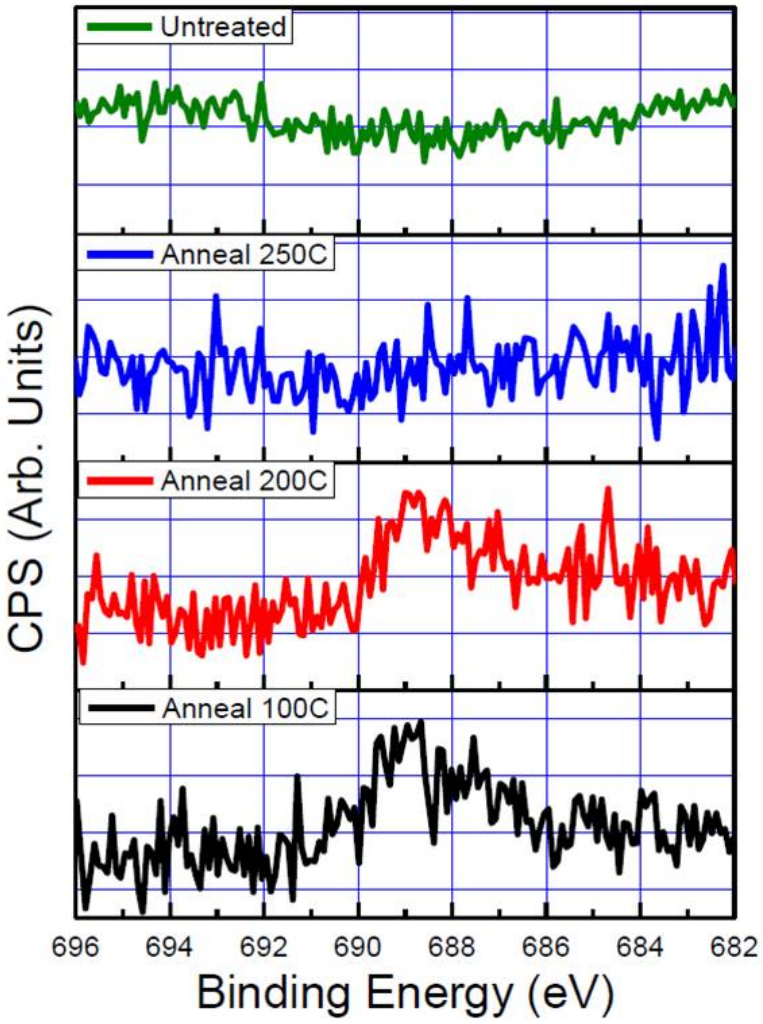

Figure 6.13: : F 1s XPS spectra of fluorinated bulk MoS_2 after annealing the sample in UHV for 30 mins at 100C °C (black), 200 °C (red), and 250 °C (blue). On comparison with the spectra of untreated bulk (green) MoS_2 it becomes clear that fluorine desorbs after annealing at 250 °C

Furthermore the Mo 3d and S 2p peaks show shifting to lower binding energy of about (0.5 $\pm$ 0.1) eV on fluorination as shown in Figure 6.14. This can be explained as a lowering of the Fermi level of MoS_2 toward the valence band maximum by $\sim$ 0.5 eV (i.e. p-doping) [130] The annealing increases the binding energy but it is not recovered all the way back to initial value. This can be due to removal of other absorbed species, in addition to fluorine from the surface.

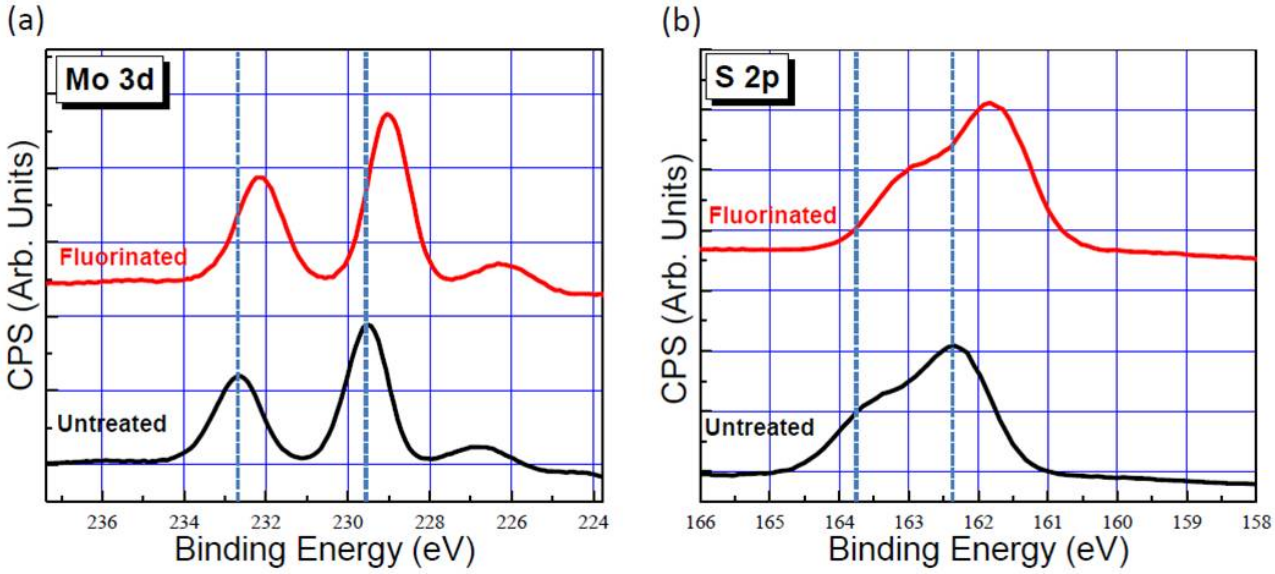

Figure 6.14: : (a)The comparison of XPS spectra of Mo 3d of untreated and fluorinated bulk MoS_2 (b) S 2p spectra comparison of untreated and fluorinated bulk MoS_2. Both these spectra shows that on fluorination the sample is p-doped.

The XPS studies clearly indicate that we are causing dilute fluorination of bulk MoS_2 sample using low energy CF_4 plasma and UHV annealing at 250 °C completely desorbs the fluorine from the surface.

Fluorination of monolayer MoS_2: We studied the fluorination of monolayer MoS_2 on SiO_2 substrate by carrying out STM studies and PL studies at room temperature. Figure 6.15 shows the MoS_2 device, made by evaporating Al contacts using TEM grid (hole width 90μm and distance to next hole is 35μm) as a shadow mask. The CF_4 plasma generated at same parameters as in the case of the bulk sample was used for fluorinating MoS_2 sample. Figure 6.16(a) shows the 50 μm by 50 μm topography of single layer CVD MoS_2 on SiO_2. We observe that like graphene single layer MoS_2 is also not atomically flat on SiO_2 substrate. It has ripples which are about (700 $\pm$ 200) pm high, which is expected due to surface roughness of SiO_2 substrate [32]. The hexagonal lattice of MoS_2 can be clearly seen in 7 nm $\times$ 7 nm area scan in Figure 6.15(b).

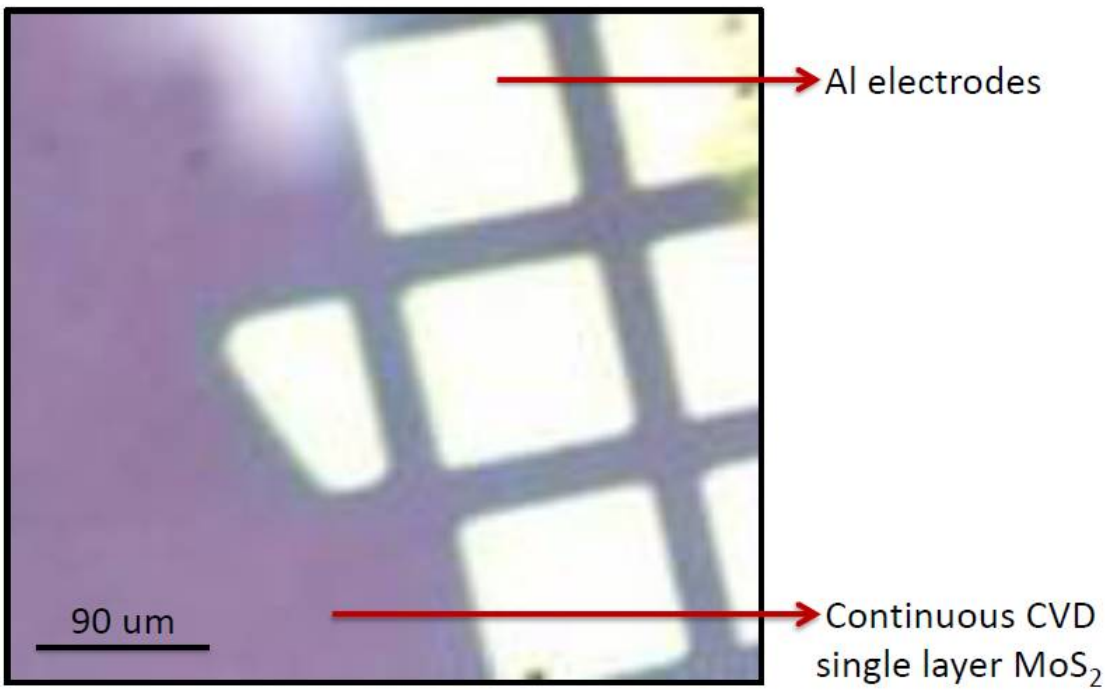

Figure 6.15: : Bright field optical picture of CVD single layer MoS_2 device on SiO_2 substrate.

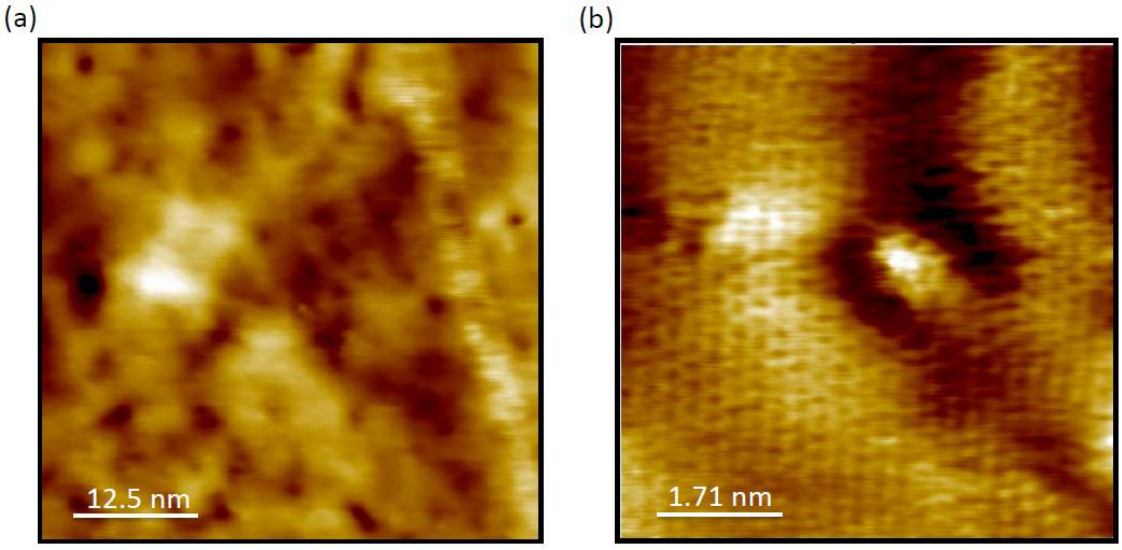

Figure 6.16: : (a) STM topography image of single layer MoS_2 on SiO_2.(b) 7nm $\times$ 7nm image showing atomic resolution, few defect sites and adsorbate on the surface of MoS_2 on SiO_2.

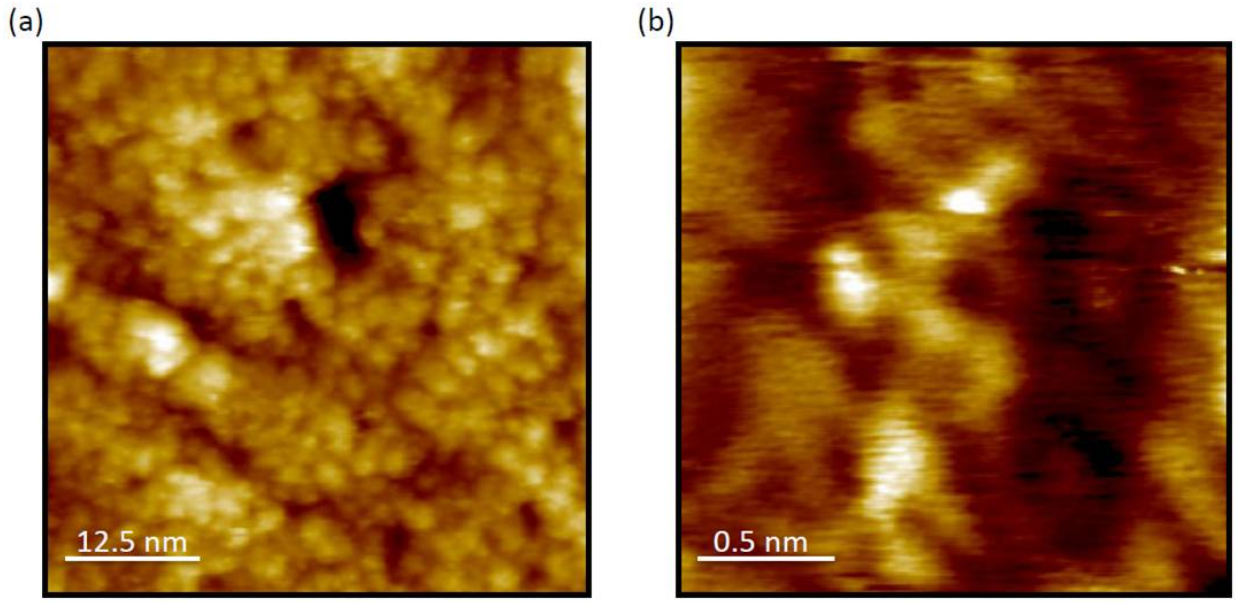

Figure 6.17: : (a) Topography of MoS_2 on SiO_2 after dilute fluorination. (b) 2nm $\times$ 2nm area scan reveals that the surface has no longer atomic resolution but appears as high profusion, indicating strain in the sample due to fluorination.

This image also shows an adsorbate on the surface as high bright spot along with few defects on the surface. These defects can be due to S or Mo vacancy. Several different area scan of MoS_2 device showed that sample was mostly clean down to atomic scale with very few dirty spots.

After fluorination, the 50 μm by 50μm topography image shows that MoS_2 surface has becomes rougher as evident in Figure 6.17(a). The roughness analysis shows that now the height corrugation is (1.5 $\pm$ 0.2) nm. Figure 6.17(b) moreover reveals that atomic resolution is lost on the sample, which is consistent with strain due to fluorine binding on the surface, making it difficult for STM tip to follow the surface morphology.

Next the sample was annealed in UHV at 260 $^{\circ}$C for 30mins. Figure 6.18(a) shows that after annealing the surface topography looks similar to before fluorination, with ripple height $\sim$ (700$\pm$ 200) pm.

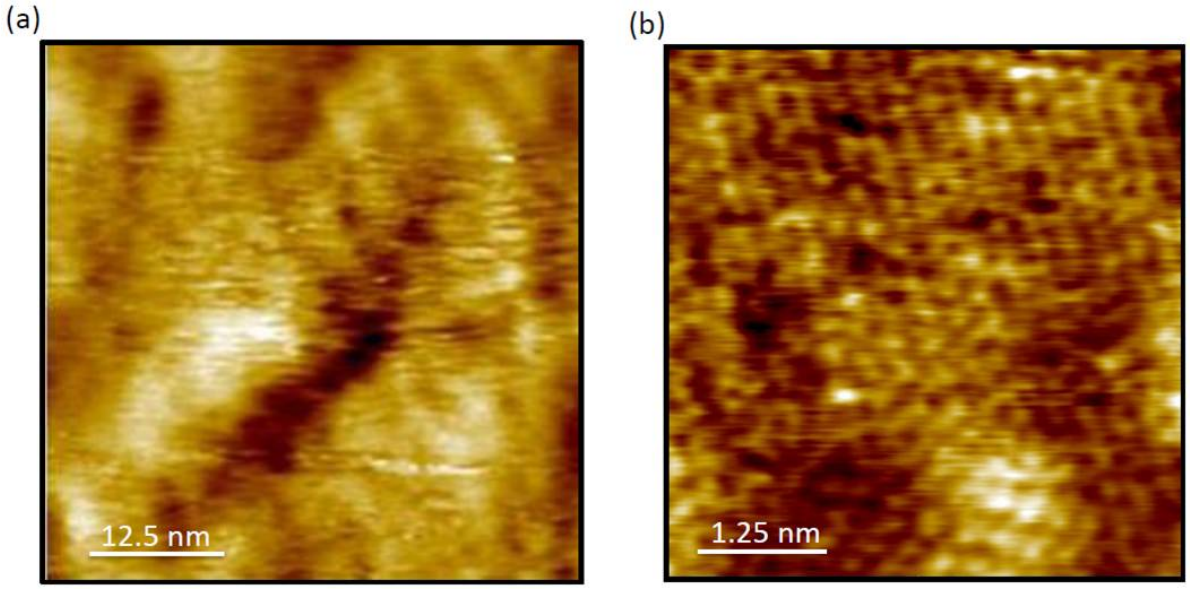

Figure 6.18: : (a) STM morphology of the bulk MoS_2 after annealing in UHV at 260 °C. for 30mins and (b) 5nm × 5nm image of MoS_2. The image exhibits atomic resolution signifying that annealing has desorbed fluorine from the surface.

On scanning 5 nm× 5 nm area we obtained atomic resolution on the surface as shown in Figure 6.18(b). The topography again shows defects on the surface. Since such defects were observed before fluorination too and the scanned area in Figure 6.16(b), Figure 6.17(b) and Figure 6.18(b) are not the same spot, so it is not possible to know if these defects were already present or formed during fluorination. However the STM studies clearly indicate that fluorine is binding to the surface of the monolayer MoS_2, which can be desorbed by annealing in UHV at 250 °C.

Furthermore PL spectroscopy was also carried out in ambient conditions before, after fluorination and after defluorination on same MoS_2 device as shown in Figure 6.19. MoS_2 has a PL peak at 1.85 eV. On fluorination the peak is quenched (39%) but after heating the PL peak intensity increases as fluorine is removed. The peak also shifts to 1.83 eV, which can be due to desorption of water and hydrocarbons from the MoS_2 surface on heating.

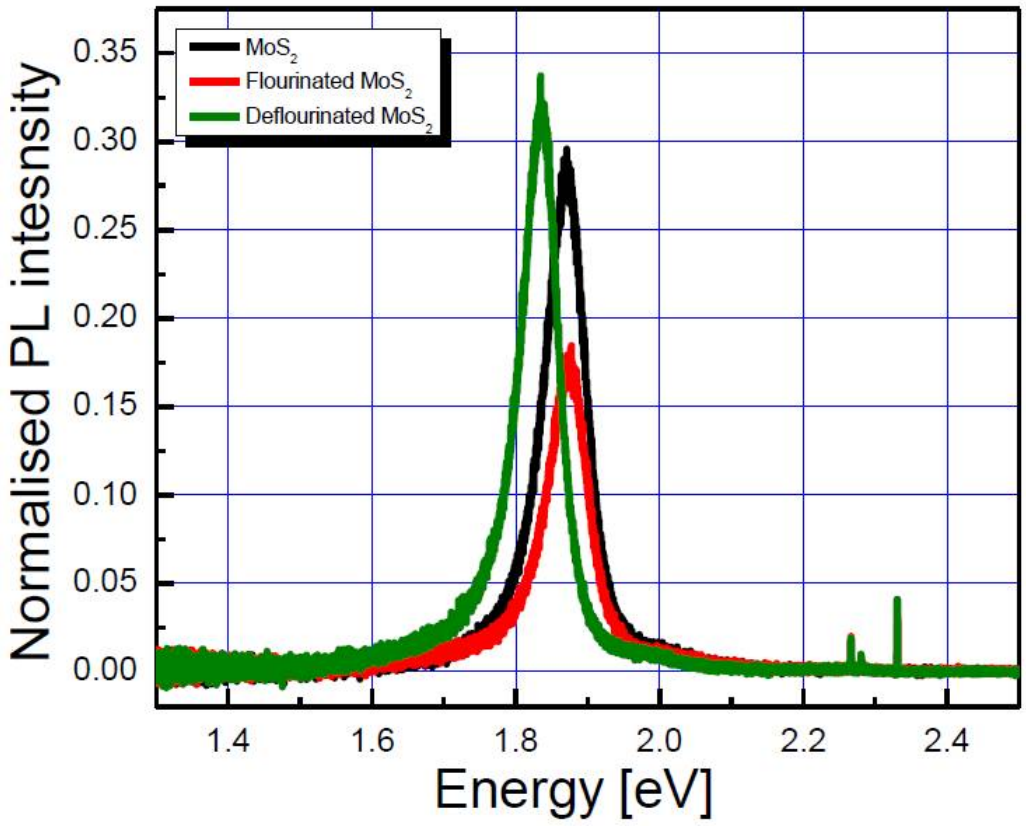

Figure 6.19: : PL spectra of single layer MoS_2 device used in STM studies, taken at three different stages: untreated, after fluorination, and after vacuum annealing at 260 °C.

Thus, using XPS study of fluorinated bulk MoS_2 we have demonstrated that fluorine is binding to the surface of MoS_2. The STM studies of fluorinated monolayer MoS_2 is consistent with XPS studies on bulk MoS_2, showing fluorine is binding to the single layer MoS_2. Further electronic transport and scanning tunneling spectroscopy (STS) studies are necessary to understand the modification of electronic properties of MoS_2 on fluorination.

CHAPTER 7: BIOFUNCTIONALIZATION OF GRAPHENE.

7.1 Structure of Peptide on graphene and graphite

Graphene sheet, an individual layer of graphite, is a semimetal with unusual physical properties.[43],[67] Graphene possesses no dangling bonds except at the edges, and their well-ordered chemical structure renders chemical interactions with the surrounding environment more predictable. In addition, transport properties of graphene are characterized by extraordinary field effect mobility even at room temperature.[131] High field effect mobility renders graphene sheets to be highly sensitive to their environment, making them ideal for sensing applications.

Graphene based field effect transistors show a sensitive, yet nonselective, response to various analytes,[132] and it is now widely accepted that selectivity, necessary for any sensors, must be imparted by functionalization. Since high sensitivity relies on high mobility, functionalization must leave the transport property of graphene unaffected. Noncovalent functionalization is ideal as it does not generate atomic-scale defects, which are extremely disruptive.[37],[38],[36],[39]

One of many promising noncovalent functionalization methods seeks to mimic and exploit the molecular recognition property of peptides found in biology [133] to impart selectivity for a wide variety of analytes. Resolving peptide structures is fundamentally important to this biomimetic approach because properties of peptides are sensitively influenced by their structures. Although the binding of peptides has been visualized using atomic force microscopy (AFM) on nanotubes [134] and graphene,[135],[136] AFM cannot be used to resolve the peptide structure. Previous studies have utilized molecular dynamics (MD) simulations [137],[138] to infer the structure of bound peptides,[134],[135],[136] but additional experimental studies are needed to confirm the validity

of these calculations.

We have performed AFM, Raman, and Fourier transform infrared (FTIR) spectroscopy to study the structure of peptides bound to graphene and graphite. This integrated strategy enabled gathering of the fingerprint signatures of the peptide, which contains information on its secondary structure. Our experimental results confirm the behavior of the peptide calculated in MD simulations. Therefore, the results demonstrate that MD simulations can be relevant for predicting the behavior of peptide-functional groups on graphene and identifying proper functional groups or various analytes.

Graphene sheets were produced using the mechanical exfoliation method, [28] and the layer thicknesses were confirmed using Raman spectroscopy.[139] Grade II HOPG used for this study was purchased from Structure Probe, Inc. The dodecamer peptide, GAMHLPWHMGTL, was synthesized by Peptide 2.0 Inc. (Chantilly, VA) at a purity of 99.39%, verified by high performance liquid chromatography. The peptide was previously identified to bind to HOPG using phage display.[135]This graphene/graphite binding peptide (GBP) was then dissolved in an aqueous buffer (100 mM Tris-HCl, pH 7.5) at a concentration of 200 μg/mL. Graphene sheets and HOPG were immersed in the GBP solution for 10 min at room temperature, washed with deionized water, and blown dry with $\mathrm{N_2}$ gas prior to analysis. A Digital Instruments 5000 AFM, operating in ambient environment, was used for imaging. Raman spectra were acquired using a Renishaw Raman spectrometer with a 532 nm laser (5% laser power, exposure time of 50 s, and 4 accumulations). FTIR and attenuated total reflectance (ATR)-FTIR measurements were acquired using a Vector 22 Fourier transform infrared spectrometer (Bruker Optics, Billerica, MA), equipped with a liquid nitrogen-cooled Hg-Cd-Te detector. FTIR of the lyophilized peptide powder was measured by pressing the powder between two $\mathrm{CaF_2}$ windows, using the spectrum of the $\mathrm{CaF_2}$ window as reference.

FTIR of the peptide in a D_2O-based buffer (150 mM NaCl, 40 mM HEPES, pH 7.2) was measured using a 25 μm spacer between the windows, using a buffer solution as reference. ATR-FTIR spectra were measured by mechanically contacting HOPG with a 1 mm thick germanium internal reflection plate (Spectral Systems, Irvington, NY) at $20 \pm 1\,^{\circ}C$. Each spectrum was the average of 1000 scans, at $2cm^{-1}$ nominal resolution. The reference spectra were measured using a bare germanium plate. Atmospheric humidity was monitored by collecting spectra at various times, using the bare CaF_2 window or the germanium plate, and were used for clearing the sample spectra of signals generated by residual humidity.

The FTIR spectrum of the GBP in the powder form displays a relatively broad amide I band with a peak in the $1660 - 1650cm^{-1}$ region as well as an amide II band around $1530cm^{-1}$, as shown in Figure 7.1(a). The peak position of the dry peptide indicates an α-helical secondary structure.[140],[141],[142],[143] When dissolved in a D_2O-based buffer, the GBP exhibits a dominant amide I peak at $1673cm^{-1}$ accompanied by a smaller peak at $1648cm^{-1}$, as shown in Figure 7.1(b). The amide II band disappears because of amide NH-to-ND conversion. Higher amide I frequencies in D_2O can be generated by various secondary structures, such as α_{II} -helix, 3_{10} -helix, reverse turns, or antiparallel β -sheet.[140],[141],[142],[143] The latter can be excluded because the antiparallel β -sheet structure generates a strong component around 1635 cm^{-1} and a weaker component around $1685cm^{-1}$.[141] While the FTIR data do not allow distinction between α_{II} -helix, 3_{10} -helix, or turn structures, the observed amide I spectra strongly suggest that at least a part of the secondary structure of the peptide changes from α-helix to another helical or turn structure upon exposure to an aqueous medium.

Incubation of graphene with the peptide results in formation of a meshlike layer as shown in Figure 7.2. This mesh layer is found on all imaged areas showing that the adsorbed layer uniformly coats graphene.

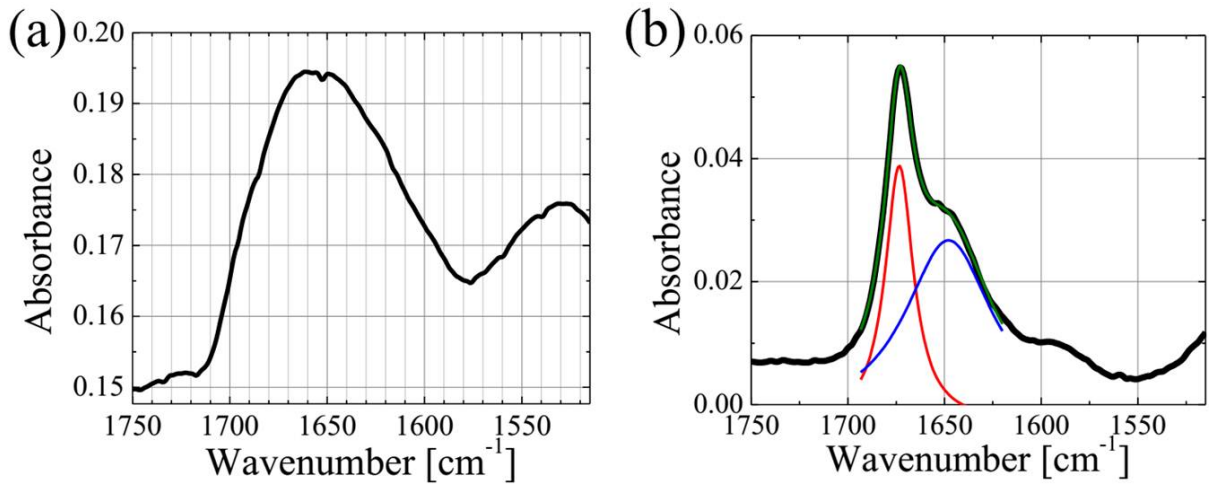

Figure 7.1: (a) Infrared spectrum of GBP in powder form, showing both amide I and amide II bands. (b) Infrared spectrum of GBP in D_2O, showing the amide I band. Red and blue curves are obtained by fitting two Lorentzian functions to the experimental data. The peaks are located at 1673 and 1648 cm^{-1}. The green curve is the result of sum of these functions.

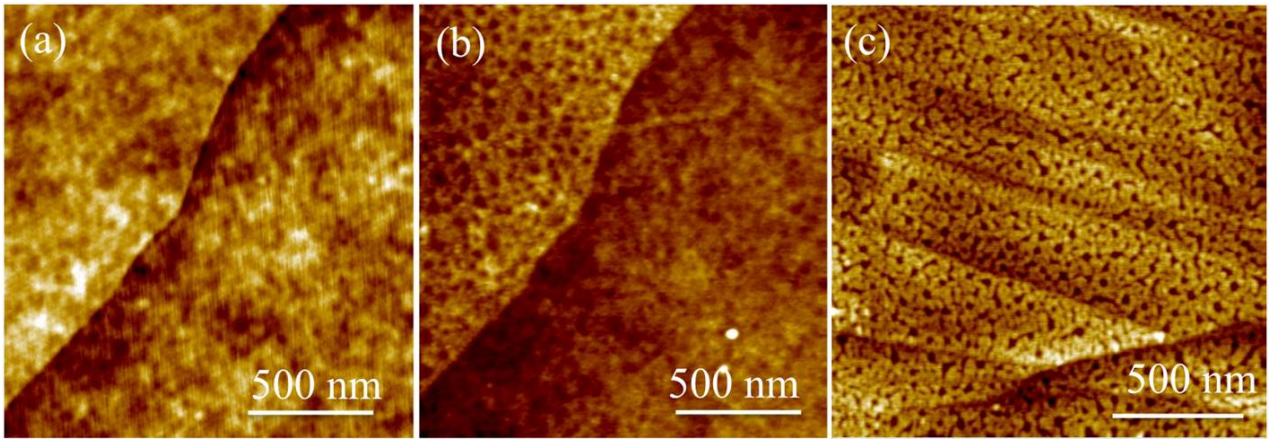

Figure 7.2: AFM topographic image of graphene (a) before and (b) after incubation with the peptide. (c) Topographic AFM image of HOPG incubated with the peptide.

Silicon oxide surface appears unaffected by incubation, indicating that the adsorption only occurs specifically on graphene. The height difference to the substrate, measured by using height histograms, increases from 0.46 ± 0.33 to 1.45 ± 0.54 nm upon incubation, suggesting that the adsorbed layer is 0.99 ± 0.63 nm thick. This thickness is similar to that observed when a dodecamer peptide was adsorbed onto carbon nanotubes.[134] Graphene and graphite possess same surface

chemical structures, and the interactions of these surfaces with peptides are expected to be similar. The AFM image of HOPG incubated with the GBP is shown in Figure 7.2(c). A similar meshlike layer appears on the HOPG surface upon incubation. Furthermore, the thickness of the adsorbed layer on HOPG is measured to be 1.10 $\pm$ 0.45 nm,[144] indistinguishable from the thickness of the peptide layer on graphene. As such, these AFM images show that the identical adsorbed layer is formed on graphene and HOPG, as expected. The adsorbed layer on HOPG is used to obtain enhanced optical spectra below.

Figure 7.3(a) compares Raman spectra of graphene before and after incubation with the peptide. Bare graphene exhibits a strong Raman signal around 1580 cm^{-1} due to its G band.[139] Incubation with the peptide produces increased signals at both 1700- 1600 and 1570- 1520 cm^{-1} regions, consistent with the amide I and amide II modes of the peptide. The peak near 1350 cm^{-1}, corresponding to the D-band, does not increase in intensity as shown in Figure 7.3(b). The $\mathrm{I_D/I_G}$ ratio is proportional to the defect density, [88] and as such, the spectra show that absorption of the peptide does not damage the graphene lattice, consistent with the expected noncovalent interaction between graphene and the peptide.

ATR-FTIR spectroscopy was used to increase the signal-to noise ratio to further analyze the nature of the adsorbed layer. Spectra display absorption bands peaking near 1670 and 1550-1540 cm^{-1} for the adsorbed peptide layer, as shown in Figure 7.4. The peak at 1580 cm^{-1} is due to the G band in graphite.[139] The spectral locations of 1670 and 1550-1540 cm^{-1} bands due to the adsorbed layer are consistent with the amide I and II bands and represent the first spectroscopic evidence that the adsorbed layer is indeed the GBP. The enhanced signal also reveals more details of the nature of the adsorbed peptide. The amide I band is blue-shifted to around 1670 cm^{-1} , compared to 1660-1650 cm^{-1} for the peptide in the powder form shown in Figure 7.1(a). Normally, the α -helical amide I mode of peptides in aqueous media is around 1655-1650 cm^{-1}.[140],[145],[146].

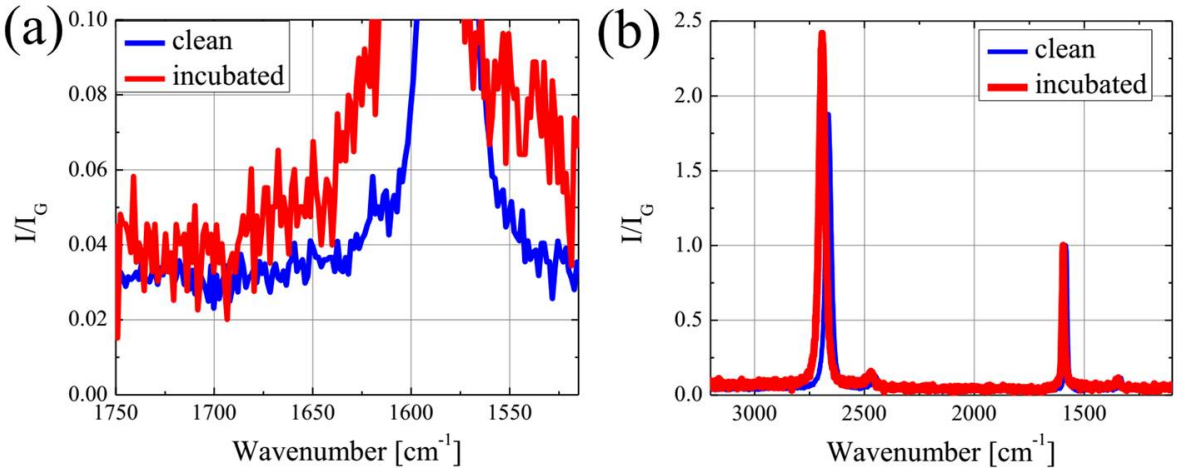

Figure 7.3: Raman spectroscopy of graphene before and after incubation with the peptide (a) between 1750 and 1525 cm^{-1} and (b) 3200 and 1100 cm^{-1}. Intensities are normalized with respect to the intensity of the G band.

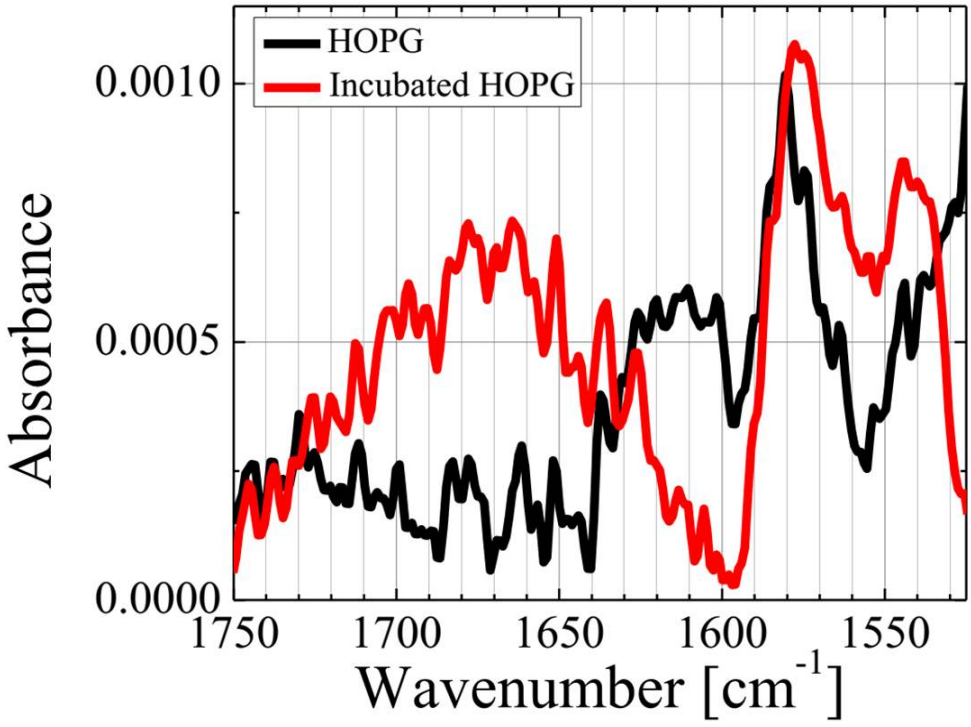

Figure 7.4: ATR-FTIR spectra of HOPG before and after incubation with the peptide.

The amide I band of the 3_{10}-helical structure is typically at 1665 cm^{-1},[141],[147] and the adsorbed layer may be conformed to a 3_{10} -helix structure. In addition, since the main contribution to the amide I mode comes from the peptide backbone C=O stretching vibration, higher amide I wavenumber (frequency) may also indicate stronger C=O bonds, which corresponds to weaker intra- or intermolecular hydrogen bonding. Blue-shifted amide I bands observed for α_{II} -helical structures in proteins and model polypeptides have also been attributed to weakened helical hydrogen bonding.[148],[149],[150],[151],[152] Therefore, the increased amide I wavenumber of the adsorbed peptide indicates that the peptide- graphite/graphene interaction induces the GBP to conform to a 3_{10}- or α_{II} -helix structure.

To understand the observed structural changes of the GBP at the atomic level, we utilized the MD simulation approach using the AMBER ff 99SB force field.[153] The five most probable initial structures of the GBP were predicted using I-TASSER software.[154](32) Five structures were first refined by performing MD simulations in vacuum. After 200 ns simulations, the radius of gyration of structures converged. The conformation of the native GBP at the lowest potential energy exhibits a highly ordered α -helix structure by forming i + 4 $\rightarrow$ i hydrogen bonding betweenH^4-H^8 and L^5- M^9 pairs as shown in Figure 7.5(a). This predicted helical structure is in agreement with our FTIR data on the GBP powder. Placing the peptide in the center of a water box with 1.2 nm TIP3P water layer in each direction, five independent molecular dynamics simulations were performed for 90 ns (40 and 50 ns in ntv and npt configuration, respectively) using various initial velocity. In contrast to the ordered helical structure in powder form, strong hydrophilicity of the histidine residues destabilizes the α -helical structure and transforms the GBP to a distorted α -helical structure as shown in Figure 7.5(b). The distorted GBP resembles 3_{10} -helix by forming i + 3 $\rightarrow$ i hydrogen bonding between H^4-W^7 and L^5- H^8 pairs as shown. Such transformation in the aqueous environment is consistent with our FTIR spectra.

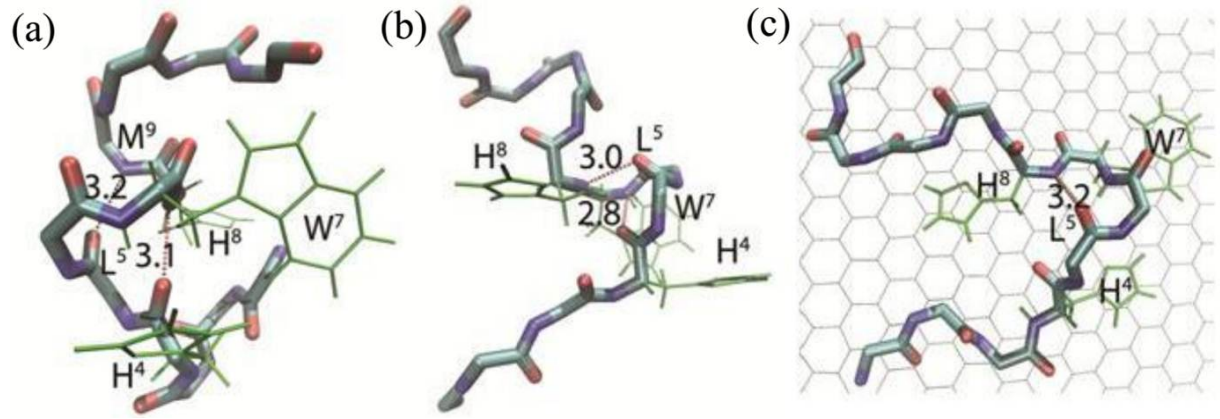

Figure 7.5: Molecular dynamics based structure of GAM peptide (a) in vacuum, (b) in water, and (c) on a 5 nm $\times$ 5 nm graphene sheet. For clarity, only part of the graphene sheet is displayed.

When molecular dynamics simulations were performed on five different systems consisting of the peptide and 5 Å $\sim$ 5 nm graphene sheet terminated with hydrogen at its edges as described previously, [136] the results converged after 40 ns and the GBP was observed to conform to graphene surface as shown in Figure 7.5(c) with an interaction energy of -106 $\pm$ 5 kcal/mol. The indole and imidazole side chains of tryptophan and histidine residues appear to parallel to the graphene sheet, distorting the helical structure and weakening the hydrogen bonding. Such calculated behavior is also consistent with our ATR-FTIR measurement of the adsorbed GBP on HOPG. Finally, to elucidate the binding mechanism, the representative structure as shown in Figure 7.5(c) was mutated and minimized. Tryptophan, histidine-4, or histidine-8 was substituted with alanine. The minimized interaction energies for the wild peptide, tryptophan to alanine, histidine-4 to alanine, and histidine-8 to alanine are - 126 $\pm$ 0.2, - 112 $\pm$ 0.2, - 115 $\pm$ 0.4, and - 123 $\pm$ 0.1 kcal/mol, respectively. These interaction energies imply that tryptophan is needed for efficient binding to graphene.

In conclusion, our vibrational spectroscopy and atomic force microscopy data show that the GBP, identified earlier using phage display,[135] binds noncovalently to graphene and HOPG. Direct

transmission FTIR spectra indicate that the peptide forms secondary structures both in powder form and in an aqueous medium. The dominant structure in the powder form is α -helix, which undergoes a transition to a distorted helical structure in aqueous solution. AFM images indicate that identical adsorbed layers are formed upon incubation on graphene and HOPG. Raman spectra show that incubation does not cause any chemical perturbation to graphene, implying that the peptide functionalizes graphene noncovalently as expected. The ATR-FTIR spectra of the adsorbed layer on HOPG indicate that the GBP is in a helical conformation, which is different from α -helix, due to its interaction with the surface. Our result thus provides new insights into how the peptide interacts with the graphene surface and serves as an important experimental confirmation of MD simulations, which are essential in designing peptide- graphene sensors with high sensitivity and selectivity. Finally, the result also shows that our approach can be useful for further studies of a wide variety of graphene-binding peptides.

7.2 Functionalizing molybdenum disulfide $(\mathrm{MoS_2})$ with peptide

In last section I have demonstrated functionalization of graphene with peptide for production of highly selective and sensitive sensors. However the absence of intrinsic band gap and poor on-off ratio ($\sim$10-100), hinders the realization of graphene based sensors for practical applications. This has accelerated efforts to either open band gap in graphene [155],[156] or explore other 2D material like metal dichalcogenides, MX_2 like MoS_2, WS_2, etc. [157],[158]

Single layer molybdenum disulfide-based FETs have been reported to have mobility of 200 cm^2 / Vsec and on/off ratio of 10^8 [37] with a band gap of 1.8eV.[157] This makes it more appealing for electronics applications as compared to graphene. Like graphene, $\mathrm{MoS_2}$ is also intrinsically sensitive to its environment and must be chemically-functionalized to impart it with the analyte selectivity required for all sensors. Peptides, which possess specific affinity to the desired analyte,

are one of the more promising candidates for functionalizing MoS_2. Hence here I have investigated peptide binding on MoS_2 using Raman spectroscopy, photoluminescence spectroscopy and atomic force microscopy at room temperature.

Single layer MoS_2 samples used in this study were obtained from the mechanical exfoliation of bulk MoS_2, purchased from SPI Supplies. The typical size of the exfoliated samples was 5 $\mu m \times 3\mu m$. We have also used large area monolayer MoS_2 on sapphire prepared by dip coating method, where substrate is dipped in a solution containing Mo solution and then subjected to sulfurization [159]. For peptide incubation, we choose the dodecamer peptide, GAMHLPWHMGTL to study its binding on MoS_2. Peptide solution in deionized water was prepared at concentration of 200 μg/mL. MoS_2 samples were immersed in peptide solution for 10 mins, then washed with deionized water and gently blown dry with N_2 gas. The Raman and photoluminescence data was collected using Renishaw Raman spectrometer with 532 nm laser (spot size diameter $\sim 1\mu m$) at power density 0.032 mW/ μm^2.

Figure 7.6 (a), (b) shows the atomic force microscopy topographic image of exfoliated single layer MoS_2 on SiO_2 before and after incubation with peptide. Clearly after peptide incubation, the MoS_2 surface is covered by meshlike layer, whereas the MoS_2 remains unchanged. The thickness of this layer is about 1.10 ± 0.25 nm, consistent with observed thickness and structure of peptide adsorbed on the graphene/ graphite surface. The surface chemistry of bulk MoS_2 and single layer MoS_2 is same so as expected similar meshlike layer was obtained upon peptide incubation on bulk MoS_2. The topographic atomic force microscopy image of peptide on bulk MoS_2 is shown in Figure 7.6(c). Additionally, we also incubated deionized water on the MoS_2. Atomic force microscopy topographic images at different spots did not show any meshlike layer. This clearly points out that like graphene, peptide is preferentially binding to MoS_2 surface.

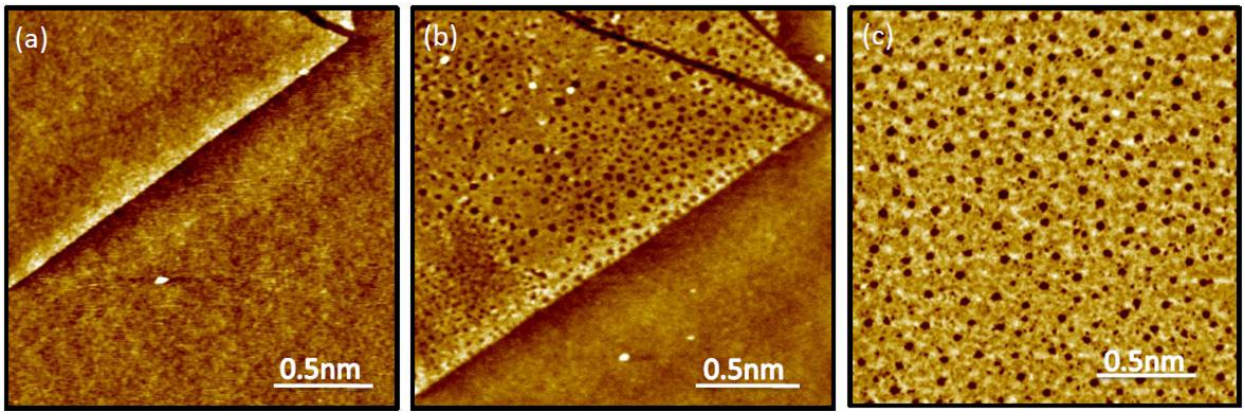

Figure 7.6: AFM topographic image of single layer MoS_2. (a) before and (b) after incubation with peptide. (c) AFM topographic image of bulk MoS2 after incubation with peptide.

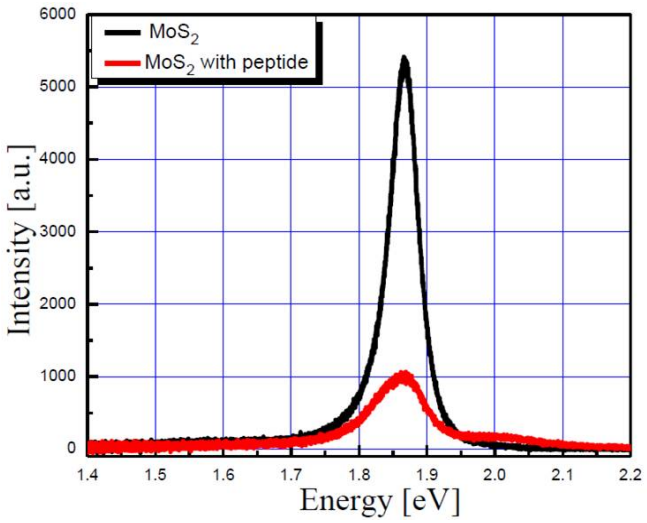

Figure 7.7: The photoluminescence signal for single layer MoS_2 with and without peptide. The data was acquired at exposure time 10sec and 4 accumulations.

Figure 7.7 compares the photoluminescence signal (PL) of single layer MoS_2 before and after peptide incubation. The single layer MoS_2 has a PL peak at 1.86 eV arising from exciton peak, which corresponds to direct band gap transition at K point in the Brillouin zone. Peptide adsorption on MoS_2 leads to about 80 $\%$ quenching of the PL intensity. The Raman data acquired after peptide incubation on bulk and exfoliated MoS_2 does not show any amide I and amide II peak at 700-1600 and 1570-1520 cm^{-1} regions corresponding to peptide as shown in Figure 7.8.

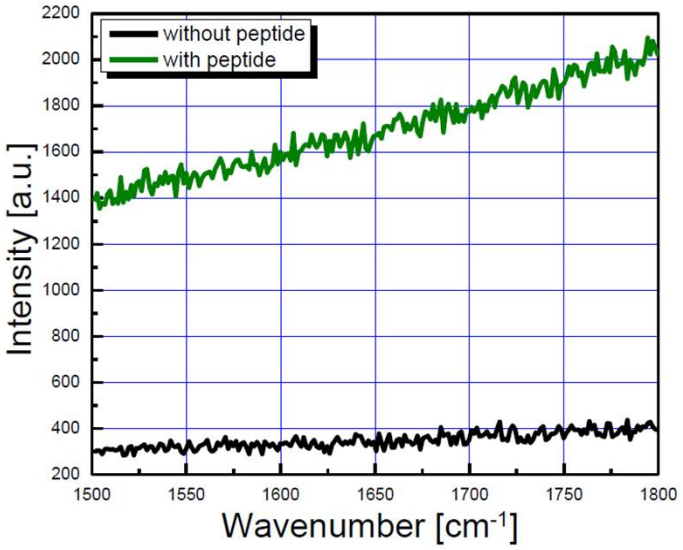

Figure 7.8: Raman spectroscopy of MoS_2 before and after incubation with the peptide between 18000 and 1500 cm^{-1}.

Since the Fourier transform infrared (FTIR) Spectroscopy is complementary to Raman spectroscopy, so we carried out FTIR measurements on bulk MoS_2 and dip coated monolayer MoS_2 before and after peptide incubation. Strangely again no amide peak was obtained for adsorbed peptide layer. Although AFM topographic images clearly indicates peptide binding to MoS_2 surface, the optical spectroscopy does not reveal the structure of the peptide binding to the MoS_2.

APPENDIX A: PROCEDURES FOR UHV LIQUID HELIUM CRYOSTAT CHAMBER

A.1 Pump down

a. Close the venting valve (1.33" metal seal valve, Do not over tighten).

b. Open the turbo pump valve.

c. Turn on the mechanical pump.

d. Turn on the turbo pump cooling fan (USB cable).

e. Turn on the turbo pump.

f. Mount the RGA controller on the chamber.

g. Wait until the system pressure is below 1×10^{-5} torr.

h. Turn on the filament, but don't turn on the electron multiplier.

i. Perform leak check.

j. Make sure that helium gas is off after leak checking.

A.2 Bake out

a. Turn off the RGA and remove it from the chamber.

b. Remove any cooling water lines.

c. Remove the rubber band from the shutter magnetic coupling.

d. Chamber has been wrapped with the heater tape: make sure that it is still properly wrapped still. (you might have to redo the wrapping on the helitran flange.)

e. Then cover the chamber with aluminum foil (especially carefully wrap the windows and ceramic around RGA pins).

f. Plug the heating tapes and increase the voltage up to 32 V in steps of 10 V, after every 10 mins.

g. Wait 10 minutes to make sure that nothing is burning severely.

Optional: Bakeout of ion pump (only if ion pump has been vented)

h. Open the ion pump gate valve.

i. Turn off the ion pump.

j. Plug in the cable labeled ”ion pump bakeout cable” straight into the wall.

k. Set TSP filament current to 30 A for the duration of the bakeout.

A.3 Chamber cool down after bake out

a. System pressure should be down to near 1×10^{-7} torr.

b. Open the ion pump valve.

c. Close Turbo pump valve and then stop it.

d. Turn off the turbo pump cooling fan.

e. Also turn off the mechanical pump.

f. Turn off the heating.

g. Uncover the foil from the RGA pin area.

h. Restart the Temp controller if it shows an ”alarm”.

i. Set the temperature at 490K and start the heater (if necessary, graphene devices might blow up so know what you are doing here.)

j. Turn off Variac

k. Before the chamber cools: Degas all filaments.

A.4 Degassing Filaments

A.4.1 Residual Gas Analyzer (RGA)

a) Wait until the RGA feed through is cold.

b) Put the RGA controller on the chamber.

c) Turn on its filament and electron multiplier.

d) Analog scan: the presence of any O_2 indicates a leak.

A.4.2 Ion Gauge

When the system has completely cooled down, the system pressure should reach below 1×10^{-9} torr. If the system pressure remains high and if there is any oxygen partial pressure detected, check for leak. First place you should check is the vent valve and move onto the most recent flange that you have tightened.

A.4.3 Outgassing the hydrogen Cracker

a. Make sure that the sample shutter is closed.

b. For degassing the shroud apply voltage of about of 700 V and slowly increase the emission current to 10 mA so that the power is 7 W.

c. Wait until the temperature is 200 degrees.

d. Turn off the emission current and voltage completely.

e. Start flowing compressed air through the cooling shroud.

f. Wait until the temperature is below 70 degrees and turn on the water flow.

g. Increase the filament current until the emission current is 50mA and voltage is 1000 V, so that

the power is 50 W.

h. When hydrogen filament has out gassed sufficiently pass a little bit of hydrogen (so as to prevent the backscattering).

i. Then let it cool.

A.5 Venting

a. Turn off the ion gauge filament.

b. Turn off all other filaments esp. check the hydrogen cracker; make sure that is completely off. Filament current should be 0 and the system should be on standby.

c. Close the ion pump valve (keep the ion pump on though).

d. Close the turbo pump valve and turn off the turbo pump and mechanical pump if it is on.

e. Open the vent valve.

A.6 Transport Probe cool down

a. Order enough helium gas and *liquid for the experiment. Contact Air Gas by Wednesday morning for Friday delivery. 10 liters of LHe is usually enough to just cool to 4K. [Make sure to order a standard 60 liter dewar (shorter) in order to reach the bottom of the dewar.] *Note: Since the liquid helium recovery system is now installed in the department, there is no need to commercially order liquid helium.

b. Make sure that the O-ring (orange viton o-ring) at the top of the helitran is still in place, if not fix.

c. First check the Helium volume left in the storage dewar. 10 liters are enough for cooling down to 4 K.

d. Before you remove the transfer tube from the wall, slide down the storage dewar adaptor all the way to the bottom of the transfer tube on the storage dewar side.

e. Situate the step ladder in the right place for you to insert the transfer tube in the storage dewar.

f. Depressurize the storage dewar and carefully insert the transfer tube in the dewar.

g. Before you insert the transfer tube into the liquid section, pressurize the storage dewar. Pressurize the dewar to 5 psi. Feel the helitran end of the transfer tube and make sure that some gas is coming out.

h. Insert the transfer tube all the way into the storage dewar slowly. You may have to depressrize as helium starts to boil off. Maintain the pressure at around 5 psi until 4 K is reached.

i. Insert the transfer tube (the Helitran side) and tighten the adjustment nut 4 turns from the pen mark.

j. Connect the exhaust port to the flow meter. Open the flow meter valve completely. The flow meter should read more than 2 if not try to pressurize the storage dewar or you need to unblock the clog which have formed in the transfer tube.

k. Connect the exhaust port heater to a variac and set voltage to 36 volts.

l. After 30 minutes, liquid helium will start to transfer; at this point reduce the flow meter setting to 6 to prevent cooling too fast.

m. After 4 K has been reached, reduce the dewar pressure to 2.5 psi and open the valve to the 2.5 psi relieving port on the dewar adaptor.

n. Adjust the adjustment nut to minimize the tip flow as written in the instruction manual.

o. Stabilize the temperature before measurement.

APPENDIX B: PROCEDURE FOR THE GENERATION OF HYDROGEN PLASMA USING SAMCO REACTIVE ION ETCHER (RIE)

B.1 Turn on procedure

a. Turn on the pumps.

b. Check the N_2 gas bottle pressure (P $\sim$ 5 psi).

c. Make sure that the valve is open ($\%$ 100) on MKS pressure controller.

d. Turn on RIE; first the breaker on the back, and then press ON button on front panel.

e. Press the START button on RIE.

B.2 Oxygen Pump Out and Leak Test

Pump out oxygen from system and oxygen lines and perform system leakage check before connecting hydrogen.

a. Make sure timer on RIE is set on 1hour or more.

b. Disconnect the oxygen line (quick connection) and cap with the white hose.Make sure Argon and CF_4 is closed.

c. Wait till pressure is less than 20 mTorr.

d. Open GV2 Valve to pump out Oxygen.

e. Ensure Oxygen valve V1 is closed and open the Oxygen valve V2 only.

f. Fully adjust mass flow controller pot all the way clockwise i.e. all the way open.

g. Allow the system to pump till below 20 mtorr.

h. Open the Oxygen valve V1 to pump air into the system (to make sure there is no oxygen in the small hose left to the Oxygen valve V1).

i. Wait for a minute or so.

j. Close the Oxygen valve V1.

k. Watch mass flow controller to make sure that once the lines are pumped out of Oxygen the mass

flow meter should continue to read zero if there is no Oxygen leakage in lines. Once it is certain that lines are not leaking then next step is to make sure SAMCO is not leaking.

l. For this, turn off the mass flow controller pot by turning it anticlockwise and close the vacuum valve at the rear of SAMCO. Watch for system leaks (this step is to check any leak in the system) Pressure shouldn't increase substantially.

m. If no leakage, then proceed further.

n. Reopen the vacuum valve at rear of SAMCO.

B.3 Vent the system

a. Turn off GV2.

b. When pressure is less than 20 mTorr, press "close" on MKS controller.

c. Wait until 0 % is shown on the position of butterfly valve.

d. Press "RESET" on RIE. When alarm sounds press "RESET" again.

e. Open the chamber and load your sample.

B.4 Pump down SAMCO again

a. Make sure timer on RIE is set on 1hour or more.

b. Open RIE vacuum valves; press Open on MKS pressure controller.

c. Wait till pressure is less than 20 mTorr.

B.5 Hydrogen plasma

a. Turn on and flow the N_2 gas into the pump at 5 liters/min. (N_2 cylinder connected to the exhaust of the pump in the utility corridor).

b. Open the H_2 cylinder and flow $H_2(\sim 5\text{psi})$.

c. Connect the H_2 hose to the Oxygen valve V1.

d. Turn on GV2.

e. Open Oxygen valves V1 and V2.

f. Turn on mass flow controller pot clockwise to read 30 sccm and wait for 5mins to purge the remaining segment of line of O_2.

g. After 5mins turn down the mass flow controller pot to read the required flow of H_2 (for e.g. 5 sccm)

h. When required pressure is achieved and stable, press "RF ON" for desired time and check the plasma in the view port on RIE to make sure plasma is generated.

i. After done using plasma close Oxygen valve V1 and open butterfly valve 100 $\%$ and turn the mass flow controller pot to read 30 sccm and wait mass flow controller pot to read zero (i.e. till H_2 is removed)

j. Then close mass flow controller pot and turn off Oxygen valve 2 and then GV2.

k. Turn off H_2 gas from the cylinder and disconnect the line and let it be open to air

l. Turn off (close the cylinder) N_2 purge gas going to pump.

B.6 Sample unloading

a. When pressure is less than 20 m Torr, press "close" on MKS controller.

b. Wait until 0% is shown on the position of butterfly valve.

c. Press ”RESET” on RIE. When alarm sounds press ”RESET”again.

d. Take out your sample and pump down the chamber again (STEP D)

B.7 Removal of remaining hydrogen and shut down procedure.

a. After disconnecting the H_2 line, open the mass flow controller pot all the way open, so that air goes in and open GV2 and Oxygen valves V1 & V2. Wait for 3-5 mins.

b. Turn off oxygen valve V1 and connect Oxygen hose.

c. Open oxygen valve V1 for 2-3 mins to bleed Oxygen through system.

d. Close oxygen valve V1; close the mass flow controller pot; close V2 and then turn off GV2.

e. Wait for pressure to go below 20 mTorr.

f. Hit Close on MKS controller.

g. Turn off SAMCO, controller and pumps.

LIST OF REFERENCES

[1] Novoselov, K. S., Geim, A. K., Morozov, S. V., Jiang, D., Zhang, Y., Dubonos, S. V., Grigorieva, I. V., and Firsov, A. A. *Science* **306**(5696), 666–669 (2004).

[2] Li, X., Cai, W., An, J., Kim, S., Nah, J., Yang, D., Piner, R., Velamakanni, A., Jung, I., Tutuc, E., Banerjee, S. K., Colombo, L., and Ruoff, R. S. *Science* **324**(5932), 1312–1314 (2009).

[3] Lee, Y.-H., Zhang, X.-Q., Zhang, W., Chang, M.-T., Lin, C.-T., Chang, K.-D., Yu, Y.-C., Wang, J. T.-W., Chang, C.-S., Li, L.-J., and Lin, T.-W. *Advanced Materials* **24**(17), 2320–2325 (2012).

[4] Castro Neto, A. H., Guinea, F., Peres, N. M. R., Novoselov, K. S., and Geim, A. K. *Rev. Mod. Phys.* **81**, 109–162 Jan (2009).

[5] Wallace, P. R. *Phys. Rev.* **71**, 622–634 May (1947).

[6] Ando, T. *NPG Asia Materials* **1**, 17–21 (2009).

[7] Baugher, B. W. H., Churchill, H. O. H., Yang, Y., and Jarillo-Herrero, P. *Nano Letters* **13**(9), 4212–4216 (2013).

[8] Kuc, A., Zibouche, N., and Heine, T. *Phys. Rev. B* **83**, 245213 Jun (2011).

[9] Tan, Y.-W., Zhang, Y., Bolotin, K., Zhao, Y., Adam, S., Hwang, E. H., Das Sarma, S., Stormer, H. L., and Kim, P. *Phys. Rev. Lett.* **99**, 246803 Dec (2007).

[10] Wu, Y. Q., Lin, Y. M., Bol, A. A., Jenkins, K. A., Xia, F. N., Farmer, D. B., Zhu, Y., and Avouris, P. *Nature* **472**(7341), 74–78 (2011).

[11] Radisavljevic, B., Whitwick, M. B., and Kis, A. *ACS Nano* **5**(12), 9934–9938 (2011).

[12] Novoselov, K. S., Jiang, D., Schedin, F., Booth, T. J., Khotkevich, V. V., Morozov, S. V., and Geim, A. K. *Proceedings of the National Academy of Sciences of the United States of America* **102**(30), 10451–10453 (2005).

[13] Ayari, A., Cobas, E., Ogundadegbe, O., and Fuhrer, M. S. *Journal of Applied Physics* **101**(1), – (2007).

[14] Qiu, H., Pan, L., Yao, Z., Li, J., Shi, Y., and Wang, X. *Applied Physics Letters* **100**(12), – (2012).

[15] Radisavljevic, B., Radenovic, A., Brivio, J., Giacometti, V., and Kis, A. *Nature Nanotechnology* **6**(3), 147–150 (2011).

[16] Mak, K. F., Ju, L., Wang, F., and Heinz, T. F. *Solid State Communications* **152**(15), 1341 – 1349 (2012). Exploring Graphene, Recent Research Advances.

[17] Ju, L., Geng, B. S., Horng, J., Girit, C., Martin, M., Hao, Z., Bechtel, H. A., Liang, X. G., Zettl, A., Shen, Y. R., and Wang, F. *Nature Nanotechnology* **6**(10), 630–634 (2011).

[18] Ferrari, A. C. and Basko, D. M. *Nature Nanotechnology* **8**(4), 235–246 (2013).

[19] Lui, C. H., Mak, K. F., Shan, J., and Heinz, T. F. *Phys. Rev. Lett.* **105**, 127404 Sep (2010).

[20] Chen, C. F., Park, C. H., Boudouris, B. W., Horng, J., Geng, B. S., Girit, C., Zettl, A., Crommie, M. F., Segalman, R. A., Louie, S. G., and Wang, F. *Nature* **471**(7340), 617–620 (2011).

[21] Mak, K. F., Lee, C., Hone, J., Shan, J., and Heinz, T. F. *Phys. Rev. Lett.* **105**, 136805 Sep (2010).

[22] Hwang, E. H. and Das Sarma, S. *Phys. Rev. B* **77**, 115449 Mar (2008).

[23] Chen, J. H., Jang, C., Xiao, S., Ishigami, M., and Fuhrer, M. S. *Nat Nanotechnol* **3**(4), 206–9 (2008). Chen, Jian-Hao Jang, Chaun Xiao, Shudong Ishigami, Masa Fuhrer, Michael S eng Research Support, Non-U.S. Gov't Research Support, U.S. Gov't, Non-P.H.S. England 2008/07/26 09:00 Nat Nanotechnol. 2008 Apr;3(4):206-9. doi: 10.1038/nnano.2008.58. Epub 2008 Mar 23.

[24] Hess, K. and Vogl, P. *Solid State Communications* **30**(12), 797 – 799 (1979).

[25] Fischetti, M. V., Neumayer, D. A., and Cartier, E. A. *Journal of Applied Physics* **90**(9) (2001).

[26] Fratini, S. and Guinea, F. *Phys. Rev. B* **77**, 195415 May (2008).

[27] Adam, S., Hwang, E. H., Galitski, V. M., and Das Sarma, S. *Proc Natl Acad Sci U S A* **104**(47), 18392–7 (2007). Adam, Shaffique Hwang, E H Galitski, V M Das Sarma, S eng 2007/11/16 09:00 Proc Natl Acad Sci U S A. 2007 Nov 20;104(47):18392-7. Epub 2007 Nov 14.

[28] Novoselov, K. S., Geim, A. K., Morozov, S. V., Jiang, D., Katsnelson, M. I., Grigorieva, I. V., Dubonos, S. V., and Firsov, A. A. *Nature* **438**(7065), 197–200 (2005). Novoselov, K S Geim, A K Morozov, S V Jiang, D Katsnelson, M I Grigorieva, I V Dubonos, S V Firsov, A A eng England 2005/11/11 09:00 Nature. 2005 Nov 10;438(7065):197-200.

[29] Chen, J. H., Jang, C., Adam, S., Fuhrer, M. S., Williams, E. D., and Ishigami, M. *Nature Physics* **4**(5), 377–381 (2008). 299LF Times Cited:516 Cited References Count:30.

[30] Ando, T. *Journal of the Physical Society of Japan* **75**(7) (2006). 079YD Times Cited:394 Cited References Count:25.

[31] Ponomarenko, L. A., Yang, R., Mohiuddin, T. M., Katsnelson, M. I., Novoselov, K. S., Morozov, S. V., Zhukov, A. A., Schedin, F., Hill, E. W., and Geim, A. K. *Physical Review Letters* **102**(20), 206603 (2009). PRL.

[32] Ishigami, M., Chen, J. H., Cullen, W. G., Fuhrer, M. S., and Williams, E. D. *Nano Letters* **7**(6), 1643–1648 (2007).

[33] Katsnelson, M. I. and Geim, A. K. *Philos Trans A Math Phys Eng Sci* **366**(1863), 195–204 (2008). Katsnelson, M I Geim, A K eng England 2007/11/21 09:00 Philos Trans A Math Phys Eng Sci. 2008 Jan 28;366(1863):195-204.

[34] Meyer, J., Geim, A., Katsnelson, M., Novoselov, K., Obergfell, D., Roth, S., Girit, C., and Zettl, A. *Solid State Communications* **143**(12), 101 – 109 (2007). Exploring graphene Recent research advances.

[35] Lui, C. H., Liu, L., Mak, K. F., Flynn, G. W., and Heinz, T. F. *Nature* **462**(7271), 339–341 (2009). 521DF Times Cited:179 Cited References Count:28.

[36] Stauber, T., Peres, N. M. R., and Guinea, F. *Physical Review B* **76**(20), 205423 (2007). PRB.

[37] Ostrovsky, P. M., Gornyi, I. V., and Mirlin, A. D. *Physical Review B* **74**(23), 235443 (2006). PRB.

[38] Titov, M., Ostrovsky, P. M., Gornyi, I. V., Schuessler, A., and Mirlin, A. D. *Physical Review Letters* **104**(7), 076802 (2010). PRL.

[39] Wehling, T. O., Katsnelson, M. I., and Lichtenstein, A. I. *Physical Review B* **80**(8), 085428 (2009). PRB.

[40] Chen, J. H., Cullen, W. G., Jang, C., Fuhrer, M. S., and Williams, E. D. *Phys Rev Lett* **102**(23), 236805 (2009). Chen, Jian-Hao Cullen, W G Jang, C Fuhrer, M S Williams, E D eng 2009/08/08 09:00 Phys Rev Lett. 2009 Jun 12;102(23):236805. Epub 2009 Jun 12.

[41] Kaasbjerg, K., Thygesen, K. S., and Jacobsen, K. W. *Physical Review B* **85**(11), 115317 (2012). PRB.

[42] *Stanford Research systems Model SR844 RF Lock-in Amplifier Chapter2* .

[43] Geim, A. K. *Science* **324**(5934), 1530–1534 (2009).

[44] Schedin, F., Geim, A. K., Morozov, S. V., Hill, E. W., Blake, P., Katsnelson, M. I., and Novoselov, K. S. *Nature Materials* **6**(9), 652–655 (2007). 207FE Times Cited:1984 Cited References Count:22.

[45] Charlier, J.-C., Blase, X., and Roche, S. *Reviews of Modern Physics* **79**(2), 677–732 (2007). RMP.

[46] Dai, H. *Surface Science* **500**(13), 218–241 (2002).

[47] Dai, H. *Accounts of Chemical Research* **35**(12), 1035–1044 (2002).

[48] Kauffman, D. and Star, A. *Angewandte Chemie International Edition* **47**(35), 6550–6570 (2008).

[49] Patolsky, F. and Lieber, C. M. *Materials Today* **8**(4), 20–28 (2005).

[50] Katoch, J., Chen, J. H., Tsuchikawa, R., Smith, C. W., Mucciolo, E. R., and Ishigami, M. *Physical Review B* **82**(8), 081417 (2010). PRB.

[51] McCreary, K. M., Pi, K., Swartz, A. G., Han, W., Bao, W., Lau, C. N., Guinea, F., Katsnelson, M. I., and Kawakami, R. K. *Physical Review B* **81**(11), 115453 (2010). PRB.

[52] McCreary, K. M., Swartz, A. G., Han, W., Fabian, J., and Kawakami, R. K. *Physical Review Letters* **109**(18), 186604 (2012). PRL.

[53] Pi, K., Han, W., McCreary, K. M., Swartz, A. G., Li, Y., and Kawakami, R. K. *Physical Review Letters* **104**(18), 187201 (2010). PRL.

[54] Chandra, B., Perebeinos, V., Berciaud, S., Katoch, J., Ishigami, M., Kim, P., Heinz, T. F., and Hone, J. *Physical Review Letters* **107**(14), 146601 (2011). PRL.

[55] Stick, D., Hensinger, W. K., Olmschenk, S., Madsen, M. J., Schwab, K., and Monroe, C. *Nature Physics* **2**(1), 36–39 (2006). 007HF Times Cited:110 Cited References Count:31.

[56] McLoughlin, J. J., Nizamani, A. H., Siverns, J. D., Sterling, R. C., Hughes, M. D., Lekitsch, B., Stein, B., Weidt, S., and Hensinger, W. K. *Physical Review A* **83**(1), 013406 (2011). PRA.

[57] Phillips, W. D. *Reviews of Modern Physics* **70**(3), 721–741 (1998). RMP.

[58] Weiner, J., Bagnato, V. S., Zilio, S., and Julienne, P. S. *Reviews of Modern Physics* **71**(1), 1–85 (1999). RMP.

[59] Das, A., Pisana, S., Chakraborty, B., Piscanec, S., Saha, S. K., Waghmare, U. V., Novoselov, K. S., Krishnamurthy, H. R., Geim, A. K., Ferrari, A. C., and Sood, A. K. *Nature Nanotechnology* **3**(4), 210–215 (2008). 284YM Times Cited:733 Cited References Count:32.

[60] Casiraghi, C., Pisana, S., Novoselov, K. S., Geim, A. K., and Ferrari, A. C. *Applied Physics Letters* **91**(23) (2007). 238MA Times Cited:258 Cited References Count:29.

[61] Mohiuddin, T. M. G., Lombardo, A., Nair, R. R., Bonetti, A., Savini, G., Jalil, R., Bonini, N., Basko, D. M., Galiotis, C., Marzari, N., Novoselov, K. S., Geim, A. K., and Ferrari, A. C. *Physical Review B* **79**(20), 205433 (2009). PRB.

[62] Casiraghi, C., Hartschuh, A., Qian, H., Piscanec, S., Georgi, C., Fasoli, A., Novoselov, K. S., Basko, D. M., and Ferrari, A. C. *Nano Letters* **9**(4), 1433–1441 (2009).

[63] Luo, Z., Cong, C., Zhang, J., Xiong, Q., and Yu, T. *Carbon* **50**(11), 4252–4258 (2012).

[64] Lee, C., Yan, H., Brus, L. E., Heinz, T. F., Hone, J., and Ryu, S. *ACS Nano* **4**(5), 2695–2700 (2010).

[65] Conley, H. J., Wang, B., Ziegler, J. I., Haglund, R. F., Pantelides, S. T., and Bolotin, K. I. *Nano Letters* **13**(8), 3626–3630 (2013).

[66] Tongay, S., Zhou, J., Ataca, C., Liu, J., Kang, J. S., Matthews, T. S., You, L., Li, J., Grossman, J. C., and Wu, J. *Nano Letters* **13**(6), 2831–2836 (2013).

[67] Geim, A. K. and Novoselov, K. S. *Nat Mater* **6**(3), 183–91 (2007). Geim, A K Novoselov, K S eng England 2007/03/03 09:00 Nat Mater. 2007 Mar;6(3):183-91.

[68] Novikov, D. S. *Applied Physics Letters* **91**(10), – (2007).

[69] *Contacts were thermally evaporated gold with chromium sticking layers.* .

[70] Chen, J. H., Jang, C., Ishigami, M., Xiao, S., Cullen, W. G., Williams, E. D., and Fuhrer, M. S. *Solid State Communications* **149**(27-28), 1080–1086 (2009). Sp. Iss. SI 465HV Times Cited:43 Cited References Count:53.

[71] Jang, C., Adam, S., Chen, J. H., Williams, E. D., Das Sarma, S., and Fuhrer, M. S. *Physical Review Letters* **101**(14), 146805 (2008). PRL.

[72] Caragiu, M. and Finberg, S. *Journal of Physics-Condensed Matter* **17**(35), R995–R1024 (2005). 967ZV Times Cited:75 Cited References Count:55.

[73] Chan, K. T., Neaton, J. B., and Cohen, M. L. *Physical Review B* **77**(23), 235430 (2008). PRB.

[74] Hwang, E. H. and Das Sarma, S. *Physical Review B* **75**(20), 205418 (2007). PRB.

[75] Dean, C. R., Young, A. F., Meric, I., Lee, C., Wang, L., Sorgenfrei, S., Watanabe, K., Taniguchi, T., Kim, P., Shepard, K. L., and Hone, J. *Nat Nanotechnol* **5**(10), 722–6 (2010). Dean, C R Young, A F Meric, I Lee, C Wang, L Sorgenfrei, S Watanabe, K Taniguchi, T Kim, P Shepard, K L Hone, J eng Research Support, Non-U.S. Gov't Research Support, U.S. Gov't, Non-P.H.S. England 2010/08/24 06:00 Nat Nanotechnol. 2010 Oct;5(10):722-6. doi: 10.1038/nnano.2010.172. Epub 2010 Aug 22.

[76] Bolotin, K., Sikes, K., Jiang, Z., Klima, M., Fudenberg, G., Hone, J., Kim, P., and Stormer, H. *Solid State Communications* **146**(910), 351 – 355 (2008).

[77] Bolotin, K. I., Sikes, K. J., Hone, J., Stormer, H. L., and Kim, P. *Phys. Rev. Lett.* **101**, 096802 Aug (2008).

[78] Bostwick, A., McChesney, J. L., Emtsev, K. V., Seyller, T., Horn, K., Kevan, S. D., and Rotenberg, E. *Phys. Rev. Lett.* **103**, 056404 Jul (2009).

[79] Elias, D. C., Nair, R. R., Mohiuddin, T. M. G., Morozov, S. V., Blake, P., Halsall, M. P., Ferrari, A. C., Boukhvalov, D. W., Katsnelson, M. I., Geim, A. K., and Novoselov, K. S. *Science* **323**(5914), 610–613 (2009).

[80] Ni, Z. H., Ponomarenko, L. A., Nair, R. R., Yang, R., Anissimova, S., Grigorieva, I. V., Schedin, F., Blake, P., Shen, Z. X., Hill, E. H., Novoselov, K. S., and Geim, A. K. *Nano Letters* **10**(10), 3868–3872 (2010).

[81] *Graphene is obtained from Kish graphite by mechanical exfoliation on 280 nm SiO2 over doped Si, which is used as the back gate. Raman spectroscopy is used to confirm that the samples are single layer graphene. Au/Cr electrodes, defined by electron-beam lithography, contact the graphene sheets. The devices are annealed in H2 /Ar at 300 C for 1 hour to remove resist residues. Each device is annealed in ultrahigh vacuum at 490 K for longer than 8 hours to eliminate any residual adsorbates prior to hydrogen dosing experiments. .*

[82] *Dosing is done at a constant temperature, which varied between different devices.* .

[83] *The dosage rate is estimated from the angular distribution of atomic hydrogen provided by the manufacturer.* .

[84] Ryu, S., Han, M. Y., Maultzsch, J., Heinz, T. F., Kim, P., Steigerwald, M. L., and Brus, L. E. *Nano Letters* **8**(12), 4597–4602 (2008).

[85] Zhu, Z. H., Lu, G. Q., and Wang, F. Y. *The Journal of Physical Chemistry B* **109**(16), 7923–7927 (2005).

[86] Carneiro M.A., C. R. *Private Communication* .

[87] Malard, L., Pimenta, M., Dresselhaus, G., and Dresselhaus, M. *Physics Reports* **473**(56), 51 – 87 (2009).

[88] Lucchese, M. M., Stavale, F., Ferreira, E. H. M., Vilani, C., Moutinho, M. V. O., Capaz, R. B., Achete, C. A., and Jorio, A. *Carbon* **48**(5), 1592–1597 (2010).

[89] Canado, L. G., Takai, K., Enoki, T., Endo, M., Kim, Y. A., Mizusaki, H., Jorio, A., Coelho, L. N., Magalhes-Paniago, R., and Pimenta, M. A. *Applied Physics Letters* **88**(16), – (2006).

[90] Sato, K., Saito, R., Oyama, Y., Jiang, J., Canado, L., Pimenta, M., Jorio, A., Samsonidze, G., Dresselhaus, G., and Dresselhaus, M. *Chemical Physics Letters* **427**(13), 117 – 121 (2006).

[91] Peres, N. M. R., Guinea, F., and Castro Neto, A. H. *Phys. Rev. B* **73**, 125411 Mar (2006).

[92] Ferreira, A., Viana-Gomes, J., Nilsson, J., Mucciolo, E. R., Peres, N. M. R., and Castro Neto, A. H. *Phys. Rev. B* **83**, 165402 Apr (2011).

[93] *Previous calculations Ref[10], Ref[11], Ref[46] using resonant scatterers with infinite on-site energy yield a resistivity exponent less or equal to -1.* .

[94] $\mu = \frac{1}{c_g} \times \frac{d\sigma}{dV_g}$ *where* $mathrm\mu$ *is field-effect mobility and* c_g *is capacitance per unit area, was used to calculate the gate-dependent mobility.* .

[95] Morozov, S. V., Novoselov, K. S., Katsnelson, M. I., Schedin, F., Elias, D. C., Jaszczak, J. A., and Geim, A. K. *Phys. Rev. Lett.* **100**, 016602 Jan (2008).

[96] Zhang, M., Chen, C., He, Y., and Xiao, Y. *Phys Rev E Stat Nonlin Soft Matter Phys* **72**(5 Pt 1), 051919 (2005). Zhang, Ming Chen, Changjun He, Yi Xiao, Yi eng Comparative Study Research Support, Non-U.S. Gov't 2005/12/31 09:00 Phys Rev E Stat Nonlin Soft Matter Phys. 2005 Nov;72(5 Pt 1):051919. Epub 2005 Nov 16.

[97] Kerwin, J. and Jackson, B. *The Journal of Chemical Physics* **128**(8), – (2008).

[98] Guinea, F., Horovitz, B., and Doussal, P. L. *Solid State Communications* **149**(2728), 1140 – 1143 (2009). Recent Progress in Graphene Studies.

[99] Pereira, V. M., Castro Neto, A. H., Liang, H. Y., and Mahadevan, L. *Phys. Rev. Lett.* **105**, 156603 Oct (2010).

[100] Stauber, T., Peres, N. M. R., and Guinea, F. *Phys. Rev. B* **76**, 205423 Nov (2007).

[101] Dean, C. R., Wang, L., Maher, P., Forsythe, C., Ghahari, F., Gao, Y., Katoch, J., Ishigami, M., Moon, P., Koshino, M., Taniguchi, T., Watanabe, K., Shepard, K. L., Hone, J., and Kim, P. *Nature* **497**(7451), 598–602 (2013). 152UF Times Cited:25 Cited References Count:30.

[102] Hwang, E. H., Adam, S., and Das Sarma, S. *Phys. Rev. Lett.* **98**, 186806 May (2007).

[103] Peres, N. M. R. *Rev. Mod. Phys.* **82**, 2673–2700 Sep (2010).

[104] *Graphene is mechanically exfoliated from kish graphite on* SiO_2*/Si with the oxide thickness of 300nm. Raman spectroscopy with excitation wavelength of 532nm is used to confirm single layer. A low laser power (less than 1mW) is used to avoid any sample heating and*

defect formation. E-beam lithography is employed to define contacts on graphene, which are deposited with Cr (5nm)/Au (70nm). All the transport measurements are carried out in ultra-high vacuum chamber.Thesis. .

[105] Ghio, E., Mattera, L., Salvo, C., Tommasini, F., and Valbusa, U. *The Journal of Chemical Physics* **73**(1) (1980).

[106] Hornekær, L., Šljivančanin, i. c. v., Xu, W., Otero, R., Rauls, E., Stensgaard, I., Lægsgaard, E., Hammer, B., and Besenbacher, F. *Phys. Rev. Lett.* **96**, 156104 Apr (2006).

[107] Zecho, T., Gttler, A., Sha, X., Jackson, B., and Kppers, J. *The Journal of Chemical Physics* **117**(18) (2002).

[108] Rhee, Y. M. and Pande, V. S. *Biophys J* **84**(2 Pt 1), 775–86 (2003). Rhee, Young Min Pande, Vijay S eng IP20 GM64782-01/GM/NIGMS NIH HHS/ Comparative Study Evaluation Studies Research Support, Non-U.S. Gov't Research Support, U.S. Gov't, Non-P.H.S. Research Support, U.S. Gov't, P.H.S. Validation Studies 2003/01/28 04:00 Biophys J. 2003 Feb;84(2 Pt 1):775-86.

[109] Kim, E. A. and Neto, A. H. C. *Epl* **84**(5) (2008). 410SO Times Cited:122 Cited References Count:28.

[110] Zhang, Y. B., Brar, V. W., Wang, F., Girit, C., Yayon, Y., Panlasigui, M., Zettl, A., and Crommie, M. F. *Nature Physics* **4**(8), 627–630 (2008). 335XB Times Cited:137 Cited References Count:28.

[111] Stolyarova, E., Rim, K. T., Ryu, S., Maultzsch, J., Kim, P., Brus, L. E., Heinz, T. F., Hybertsen, M. S., and Flynn, G. W. *Proceedings of the National Academy of Sciences* **104**(22), 9209–9212 (2007).

[112] Cullen, W. G., Yamamoto, M., Burson, K. M., Chen, J. H., Jang, C., Li, L., Fuhrer, M. S., and Williams, E. D. *Physical Review Letters* **105**(21), 215504 (2010). PRL.

[113] Zhang, Y. B., Brar, V. W., Girit, C., Zettl, A., and Crommie, M. F. *Nature Physics* **5**(10), 722–726 (2009). 511RW Times Cited:229 Cited References Count:29.

[114] Xu, K., Cao, P. G., and Heath, J. R. *Science* **329**(5996), 1188–1191 (2010). 645SG Times Cited:84 Cited References Count:30.

[115] Xue, J., Sanchez-Yamagishi, J., Bulmash, D., Jacquod, P., Deshpande, A., Watanabe, K., Taniguchi, T., Jarillo-Herrero, P., and LeRoy, B. J. *Nat Mater* **10**(4), 282–5 (2011). Xue, Jiamin Sanchez-Yamagishi, Javier Bulmash, Danny Jacquod, Philippe Deshpande, Aparna Watanabe, K Taniguchi, T Jarillo-Herrero, Pablo LeRoy, Brian J eng Letter England 2011/02/15 06:00 Nat Mater. 2011 Apr;10(4):282-5. doi: 10.1038/nmat2968. Epub 2011 Feb 13.

[116] Yankowitz, M., Xue, J. M., Cormode, D., Sanchez-Yamagishi, J. D., Watanabe, K., Taniguchi, T., Jarillo-Herrero, P., Jacquod, P., and LeRoy, B. J. *Nature Physics* **8**(5), 382–386 (2012). 936OF Times Cited:51 Cited References Count:20.

[117] Decker, R., Wang, Y., Brar, V. W., Regan, W., Tsai, H. Z., Wu, Q., Gannett, W., Zettl, A., and Crommie, M. F. *Nano Letters* **11**(6), 2291–2295 (2011). 773QJ Times Cited:97 Cited References Count:28.

[118] Tsukamoto, T. and Ogino, T. *Applied Physics Express* **2**(7) (2009). 477TN Times Cited:15 Cited References Count:21.

[119] Yazyev, O. V. and Helm, L. *Phys. Rev. B* **75**, 125408 Mar (2007).

[120] Ugeda, M. M., Brihuega, I., Guinea, F., and Gomez-Rodriguez, J. M. *Phys. Rev. Lett.* **104**, 096804 Mar (2010).

[121] Chen, J.-H., Li, L., Cullen, W. G., Williams, E. D., Fuhrer, M. S., and effect in graphene with defects, T. K. *Nature Publishing Group* **7**.

[122] Hahn, J. R. and Kang, H. *Phys. Rev. B* **60**, 6007–6017 Aug (1999).

[123] Rahman, T. S. and Lee, D. *unpublished* .

[124] Aflori M., Niculescu O., D. D. D. D. *34th EPS Conference on Plasma Phys. Warsaw* **31F**(P-2.067) (2007).

[125] Lieberman, M. and Lichtenberg, A. *Wiley:New York* , pp 3277353 (1994).

[126] Nunomura, S. and Kondo, M. *Journal of Applied Physics* **102**(9), – (2007).

[127] Åhlgren, E. H., Kotakoski, J., and Krasheninnikov, A. V. *Phys. Rev. B* **83**, 115424 Mar (2011).

[128] Plechinger, G., Mann, J., Preciado, E., Barroso, D., Nguyen, A., Eroms, J., Schüller, C., Bartels, L., and Korn, T. *ArXiv e-prints* October (2013).

[129] Tongay, S., Suh, Joonki, a. A. C., Fan, Wen, a. L. A. a. J. S., Liu, J., Ko, C., Raghunathanan, R., Zhou, J., Ogletree, F., Li, J., Grossman, J. C., and Wu, J. *Sci. Rep.* **3** (2013).

[130] Chen, M. K., Nam, H., Wi, S. J., Ji, L., Ren, X., Bian, L. F., Lu, S. L., and Liang, X. G. *Applied Physics Letters* **103**(14) (2013). 232IZ Times Cited:0 Cited References Count:22.

[131] Newaz, A. K., Puzyrev, Y. S., Wang, B., Pantelides, S. T., and Bolotin, K. I. *Nat Commun* **3**, 734 (2012). Newaz, A K M Puzyrev, Yevgeniy S Wang, Bin Pantelides, Sokrates T Bolotin, Kirill I eng England 2012/03/15 06:00 Nat Commun. 2012 Mar 13;3:734. doi: 10.1038/ncomms1740.

[132] Dan, Y., Lu, Y., Kybert, N. J., Luo, Z., and Johnson, A. T. *Nano Lett* **9**(4), 1472–5 (2009). Dan, Yaping Lu, Ye Kybert, Nicholas J Luo, Zhengtang Johnson, A T Charlie eng 2009/03/10 09:00 Nano Lett. 2009 Apr;9(4):1472-5. doi: 10.1021/nl8033637.

[133] Sarikaya, M., Tamerler, C., Jen, A. K. Y., Schulten, K., and Baneyx, F. *Nature Materials* **2**(9), 577–585 (2003). 717FP Times Cited:767 Cited References Count:97.

[134] Kuang, Z., Kim, S. N., Crookes-Goodson, W. J., Farmer, B. L., and Naik, R. R. *ACS Nano* **4**(1), 452–458 (2009).

[135] Cui, Y., Kim, S. N., Jones, S. E., Wissler, L. L., Naik, R. R., and McAlpine, M. C. *Nano Lett* **10**(11), 4559–65 (2010). Cui, Yue Kim, Sang N Jones, Sharon E Wissler, Laurie L Naik, Rajesh R McAlpine, Michael C eng Research Support, Non-U.S. Gov't Research Support, U.S. Gov't, Non-P.H.S. 2010/10/15 06:00 Nano Lett. 2010 Nov 10;10(11):4559-65. doi: 10.1021/nl102564d.

[136] Kim, S. N., Kuang, Z., Slocik, J. M., Jones, S. E., Cui, Y., Farmer, B. L., McAlpine, M. C., and Naik, R. R. *J Am Chem Soc* **133**(37), 14480–3 (2011). Kim, Sang N Kuang, Zhifeng Slocik, Joseph M Jones, Sharon E Cui, Yue Farmer, Barry L McAlpine, Michael C Naik, Rajesh R eng Research Support, U.S. Gov't, Non-P.H.S. 2011/08/25 06:00 J Am Chem Soc. 2011 Sep 21;133(37):14480-3. doi: 10.1021/ja2042832. Epub 2011 Aug 29.

[137] Daggett, V. *Chem Rev* **106**(5), 1898–916 (2006). Daggett, Valerie eng GM50789/GM/NIGMS NIH HHS/ Research Support, N.I.H., Extramural Review 2006/05/11 09:00 Chem Rev. 2006 May;106(5):1898-916.

[138] Gnanakaran, S., Nymeyer, H., Portman, J., Sanbonmatsu, K. Y., and Garca, A. E. *Current Opinion in Structural Biology* **13**(2), 168–174 (2003).

[139] Dresselhaus, M. S., Jorio, A., Hofmann, M., Dresselhaus, G., and Saito, R. *Nano Lett* **10**(3), 751–8 (2010). Dresselhaus, Mildred S Jorio, Ado Hofmann, Mario Dresselhaus, Gene Saito, Riichiro eng Research Support, Non-U.S. Gov't Research Support, U.S. Gov't, Non-P.H.S. 2010/01/21 06:00 Nano Lett. 2010 Mar 10;10(3):751-8. doi: 10.1021/nl904286r.

[140] Tatulian, S. A. *Biochemistry* **42**(41), 11898–11907 (2003).

[141] Krimm, S. and Bandekar, J. *Adv Protein Chem* **38**, 181–364 (1986). Krimm, S Bandekar, J eng Research Support, U.S. Gov't, Non-P.H.S. Review 1986/01/01 Adv Protein Chem. 1986;38:181-364.

[142] Surewicz, W. K., Mantsch, H. H., and Chapman, D. *Biochemistry* **32**(2), 389–394 (1993).

[143] Arrondo, J. L. R. and Goi, F. M. *Progress in Biophysics and Molecular Biology* **72**(4), 367–405 (1999).

[144] *Measured at the locations where the flat HOPG is visible* .

[145] Haris, P. I. and Chapman, D. *Biopolymers* **37**(4), 251–263 (1995). Rd047 Times Cited:297 Cited References Count:86.

[146] Jackson, M. and Mantsch, H. H. *Critical Reviews in Biochemistry and Molecular Biology* **30**(2), 95–120 (1995). Qw751 Times Cited:800 Cited References Count:133.

[147] Kennedy, D. F., Crisma, M., Toniolo, C., and Chapman, D. *Biochemistry* **30**(26), 6541–6548 (1991).

[148] Cladera, J., Sabes, M., and Padros, E. *Biochemistry* **31**(49), 12363–12368 (1992).

[149] Dwivedi, A. M. and Krimm, S. *Biopolymers* **23**(5), 923–43 (1984). Dwivedi, A M Krimm, S eng Research Support, U.S. Gov't, Non-P.H.S. 1984/05/01 Biopolymers. 1984 May;23(5):923-43.

[150] Krimm, S. and Dwivedi, A. M. *Science* **216**(4544), 407–8 (1982). Krimm, S Dwivedi, A M eng Research Support, U.S. Gov't, Non-P.H.S. New York, N.Y. 1982/04/23 Science. 1982 Apr 23;216(4544):407-8.

[151] Nemethy, G., Phillips, D. C., Leach, S. J., and A., S. H. *Nature* **214**, 363–365 (1967).

[152] Torres, J., Sepulcre, F., and Padros, E. *Biochemistry* **34**(50), 16320–6 (1995). Torres, J Sepulcre, F Padros, E eng Research Support, Non-U.S. Gov't 1995/12/19 Biochemistry. 1995 Dec 19;34(50):16320-6.

[153] Case, D. A., Cheatham, T. E., r., Darden, T., Gohlke, H., Luo, R., Merz, K. M., J., Onufriev, A., Simmerling, C., Wang, B., and Woods, R. J. *J Comput Chem* **26**(16), 1668–88 (2005). Case, David A Cheatham, Thomas E 3rd Darden, Tom Gohlke, Holger Luo, Ray Merz, Kenneth M Jr Onufriev, Alexey Simmerling, Carlos Wang, Bing Woods, Robert J eng R01 GM055230/GM/NIGMS NIH HHS/ R01 GM061678-06A1/GM/NIGMS NIH HHS/ RR12255/RR/NCRR NIH HHS/ Research Support, N.I.H., Extramural Research Support, U.S. Gov't, P.H.S. 2005/10/04 09:00 J Comput Chem. 2005 Dec;26(16):1668-88.

[154] *http://zhanglab.ccmb.med.umich.edu/I-TASSER.* .

[155] Han, M. Y., Özyilmaz, B., Zhang, Y., and Kim, P. *Phys. Rev. Lett.* **98**, 206805 May (2007).

[156] Todd, K., Chou, H.-T., Amasha, S., and Goldhaber-Gordon, D. *Nano Letters* **9**(1), 416–421 (2009).

[157] Mak, K. F., Lee, C., Hone, J., Shan, J., and Heinz, T. F. *Physical Review Letters* **105**(13) (2010). 653ZC Times Cited:425 Cited References Count:31.

[158] Splendiani, A., Sun, L., Zhang, Y., Li, T., Kim, J., Chim, C.-Y., Galli, G., and Wang, F. *Nano Letters* **10**(4), 1271–1275 (2010). PMID: 20229981.

[159] Liu, K.-K., Zhang, W., Lee, Y.-H., Lin, Y.-C., Chang, M.-T., Su, C.-Y., Chang, C.-S., Li, H., Shi, Y., Zhang, H., Lai, C.-S., and Li, L.-J. *Nano Letters* **12**(3), 1538–1544 (2012).